DTU Library

Models and Methods for Dynamic Computed Tomography.

Aggrawal, Hari Om

Publication date:
2019

Document Version
Publisher's PDF, also known as Version of record

[Link back to DTU Orbit](#)

Citation (APA):
Aggrawal, H. O. (2019). Models and Methods for Dynamic Computed Tomography. DTU Compute. DTU Compute PHD-2018, Vol.. 477

Models and Methods for Dynamic Computed Tomography

Hari Om Aggrawal

DTU

Summary (English)

X-ray computed tomography (CT) is a widely used non-invasive technology that is used to image the internal structure of objects without cutting and breaking them. Since the inception of the first prototype of a CT scanner in 1969, the industrial and medical applications of CT are rapidly increasing. The standard image reconstruction models for X-ray CT are based on the assumption that the object of interest remains stationary during data acquisition in a CT scanner. However, this assumption fails for dynamic CT where the object of interest deforms over time, for example, scanning a beating heart, a pill dissolving in a liquid, etc. The violation of the stationarity assumption can lead to severe motion artifacts in the images reconstructed with the standard image reconstruction models.

The standard reconstruction models that are based on a stationarity assumption can be used for dynamic CT if a sufficient number of projections are acquired within a short period of time such that the object deforms within a tolerable limit. However, limited acquisition time leads to noisy measurements, and X-ray source intensity estimates based on such measurement can be highly uncertain. These uncertainties cause severe and systematic artifacts, known as ring artifacts, which may hide the important information in a reconstructed image. To mitigate this problem, we derive a new convex reconstruction model by carefully modelling the measurement process and by taking uncertainties into account. The experimental results indicate that the model effectively mitigates ring artifacts not only with simulated data, but also with real data sets.

If the stationarity assumption cannot be fulfilled, we can compensate the motion effects by incorporating the motion behaviour of the object of interest into a re-

construction model. In practice, the motion behaviour of the object is unknown. Therefore, we jointly conduct motion estimation and image reconstruction with motion-compensated reconstruction models. These models generally assume that deformations in the object are continuous and smooth over time. Thus, they are not suitable for non-smooth deformations, such as the formation of cracks. In this thesis, we derive a motion model to represent the formation and closing of cracks based on the underlying physics of the crack formation. The proposed model effectively regularizes non-smooth and large deformations along cracks with minimal influence on the nearby regions.

The motion-compensated reconstruction models implicitly exploit the redundant motion information present in the measurements acquired over time from different projection angles. Variability in the acquired projections is highly important. In view of this, we propose an interlaced projection scheme to distribute projection views over time based on the family of metallic angles. This scheme is a fixed angular gap scheme, and hence, easy to implement in practice. Moreover, this scheme is suitable for scanning a fast-deforming object. We demonstrate that the proposed interlaced distribution of projection views over time greatly enhances the spatio-temporal resolution of the motion-compensated reconstructions.

In this thesis, our investigations bring forth methodologies which have the potential to achieve high spatio-temporal resolution reconstructions of objects deforming over time. These methodologies pave the way to study the rapid dynamic behaviors, such as the fluid flowing through porous rock and the formation of cracks in drying paint, through tomographic measurements.

Summary (Danish)

Computertomografi (CT) ved brug af røntgenstråler er en bredt anvendt teknologi, som bruges til at afbilde det indre af et objekt uden at skære i eller ødelægge objektet. Antallet af industrielle og medicinske anvendelser af CT er steget støt siden den første prototype af en CT-skanner blev konstrueret i 1969. De gængse billedrekonstruktionsmodeller for røntgen-CT antager at objektet i CT-skanneren forbliver stationært unden skanningen, men denne antagelse holder ikke for dynamisk CT, hvor objektet deformerer over tid. Som eksempler på sådanne objekter kan nævnes et slående hjerte, en pille som opløses i en væske, osv. Overholdes antagelsen om stationaritet ikke, så kan de gængse billedrekonstruktionsmodeller føre til rekonstruktioner med grove bevægelsesartefakter.

De gængse rekonstruktionsmodeller kan dog bruges til dynamisk CT, hvis et tilstrækkeligt antal projektioner er til rådighed inden for et kort tidsrum, således at deformationen inden for dette tidsrum er tilpas lille. Desværre kan en begrænsning af skanningstiden føre til støjfyldte målinger, og et estimat af røntgenkildens intensitet baseret på sådanne målinger kan være behæftet med stor usikkerhed. Denne usikkerhed kan føre til slemme og systematiske artefakter, som kaldes for ringartefakter, og disse kan skjule vigtig information i det rekonstruerede billede. For at imødegå dette problem udledes en ny konveks rekonstruktionsmodel, som omhyggeligt modellerer måleprocessen for derved at tage hensyn til usikkerheder. De eksperimentielle resultater indikerer, at modellen effektivt reducerer ringartefakter for såvel simulerede data som rigtige måledata.

Hvis antagelsen om stationaritet ikke kan opfyldes, så kan man forsøge at kompensere for bevægelseseffekter ved at inkorporere en model for bevægelsen i

rekonstruktionsmodellen. I praksis er bevægelsesmodellen ukendt, og den skal derfor bestemmes eller estimeres sammen med billedet ved hjælp af en bevægelseskompenseret rekonstruktionsmodel. Sådanne modeller antager generelt at objektets bevægelse er kontinuert og glat som funktion af tid, og de er derfor ikk egnede til rekonstruktion af ikke-glatte deformationer som for eksempel formation af sprækker. I denne afhandling udledes en bevægelsesmodel, som kan repræsentere formation og lukning af sprækker. Modellen er baseret på en fysisk model for formation af sprækker, og den regularisere ikke-glatte og store deformationer langs sprækker med minimal indflydelse på omkringliggende områder.

Den bevægelseskompenseret rekonstruktionsmodel kan indirekte udnytte redundant bevægelsesinformation i måledata, som er optaget over tid fra forskellige projektionsvinkler. Variation i projektionerne er yderst vigtig. Set i dette lys foreslås et sammenflettet projektionssystem som fordeler projektionsvinklerne over tid baseret på en familie af metalliske vinkler. Dette system passer til skanning af hurtigtdeformerende objekter. Det demonstreres at den foreslåede fordeling af projektionsvinkler øger både den tidslige og den rummelige opløsning i forbindelse med bevægelseskompenserede rekonstruktioner.

Undersøgelserne i denne afhandling fører til metodikker med potentiale for at opnå rekonstruktioner med høj tidslig og rummelig opløsning af et objekts deformation over tid. Disse metodikker baner vejen for CT-baserede studier af hurtigt bevægende dynamiske systemer som f.eks. en væske, der flyder gennem et porøst materiale, eller formation af sprækker i maling under tørring.

Preface

This thesis was prepared in partial fulfillment of the requirements for acquiring the Ph.D. degree at the Technical University of Denmark (DTU). The work was carried out between April 2015 and May 2018 in the Section for Scientific Computing, Department of Applied Mathematics and Computer Science, DTU, under the supervision of Associate Professor Martin Skovgaard Andersen and Professor Per Christian Hansen. A part of the work was done during multiple visits - in total around 3 months at the Institute of Mathematics and Image Computing (MIC) at the University of Lübeck, Germany with Professor Jan Modersitzki.

Lyngby, 31 May-2018

Hari Om Aggrawal

Acknowledgements

This thesis is the outcome of contributions from many individuals in many ways. I owe my sincere gratitude to all of them and to the funding organizations, DTU IT support team, and DTU administration.

I am sincerely grateful to my supervisor Martin S. Andersen for sharing his insight in the field of computed tomography and optimization, and giving me the extensive freedom to explore different research topics. I am indebted for his patience, encouragement, faith, and firm support during my journey. I have greatly benefitted with his guidance on scientific writing and research methodology. These words are not enough to express my deep gratitude for his thoughtful mentorship throughout my Ph.D. studies.

I am very thankful to my co-supervisor Per Christian Hansen for his support during my studies and giving me the opportunity to be a part of the HD-TOMO project. A special thanks goes to the project group members Kim Knudsen, Yiqiu Dong, Rasmus Dalgas, Ekaterina Sherina, Adrian Kirkeby, and others, who created the intellectual environment which helped me a lot to grow scientific curiosity inside me, especially, to recognize the beauty of mathematics. I am especially thankful to Yiqiu Dong for several discussions during my Ph.D. studies. I am indebted to Morten Hagdrup from the Section for Scientific Computing, DTU for his prompt availability to listen patiently to my silly questions on mathematics and clarify lot of fundamental doubts. I must thank Anne Mette Eltzholtz Larsen for handling administrative tasks.

I am sincerely grateful to Jan Modersitzki from the University of Lübeck, Germany for sharing his expertise in image registration, asking numerous fundamen-

List of Symbols

$\mathbf{1}$ a vector of ones

$A \otimes B$ Kronecker product of $A \in \mathbb{R}^{m \times n}$ and $B \in \mathbb{R}^{p \times q}$

A system matrix, the forward tomography model

A^h discrete representation of forward operator

A_j system matrix associated with projection j

$\mathbf{A}$ averaging matrix on the centroid of a triangle associated with p

$\mathbf{B}$ averaging matrix on the centroid of a triangle associated with f

blkdiag block-diagonal matrix

b log-normalized measurements

D_i finite-difference matrix for the ith pixel

$\mathbf{D}$ partial derivative operator associated with f

D   discretized dissipation energy function

$\mathcal{D}$ dissipation energy function

$\det(\nabla f)$ Jacobian determinant of deformation field f

$\mathrm{diag}(x)$ $n \times n$ diagonal matrix with the elements of x on the diagonal

dim   dimension of a space

$\mathsf{E}[\mathbf{y}]$	expectation of random variable $\mathbf{y}$
E	discretized stored elastic energy function
$\mathcal{E}$	stored elastic energy function
$e_{\hat{f}}$	percent forward deformation field error
$e_{\hat{g}}$	percent backward deformation field error
$\exp(x)$	elementwise exponentiation given a vector $x \in \mathbb{R}^n$
$e(p)$	stiffness function
e_i	the ith column of an identity matrix
f^h	discretized deformation field at nodal grids with cell-width h
f_c	forward deformation field for CIR model
f_n	forward deformation field for NCIR model
$\mathbf{f}$	a column vector consists of deformation field coefficients
$f(x)$	forward deformation field/correspondence map
γ	regularization parameter for total-variation regularizer
$g(x)$	backward deformation field/correspondence map
g_c	backward deformation field for CIR model
g_n	backward deformation field for NCIR model
H	Hessian matrix
I_+	indicator function of the nonnegative orthant
I_0	X-ray source intensity
I_M	identity matrix of size $M \times M$
$J(u)$	objective function for vector u
$\mathbf{J}$	partial derivative operator associated with p
J	discretized objective function
$\mathcal{J}$	objective function
L	Lipschitz constant
$\log(x)$	elementwise logarithm given a vector $x \in \mathbb{R}^n$

l line segment between the source and a detector

$\mu(x)$ spatial attenuation function

$\mathcal{N}$ null space of a matrix

$\phi(u)$ convex regularization function for vector u

$\mathrm{P}(y)$ probability of random variable $\mathbf{y} = y$

ψ_n metallic angle

$\mathbf{p}$ a column vector consists of phase field coefficients

$p(x)$ phase-field function/soft crack indicator function

p number of projections in a rotation

R reference image

R^h discretized reference frame at cell-centered grids with cell-width h

$\mathbb{R}^n$ n-dimensional real space

$\mathbb{R}^n_+$ nonnegative orthant of $\mathbb{R}^n$

$\mathbb{R}^{m \times n}$ the set of $m \times n$ real-valued matrices

r number of detector pixels in a detector array

S discretized data-fidelity function

$\mathcal{S}$ data-fidelity function

$\sigma_{\max}$ largest singular value

$\widehat{\Sigma}_{\mathbf{b}}$ covariance matrix associated with $\mathbf{b}$

$s(p)$ similarity mask function

T template image

T_e detector exposure time/acquisition time

T_f interpolation/transformation operator

T_l transformation matrix associated with large displacement

T_m transformation matrix associated with medium displacement

T_s transformation matrix associated with small displacement

T_z transformation matrix associated with zero displacement

$\hat{u}_{\text{amap}}$ approximate maximum a posteriori estimate of the vector u

$\hat{u}_{\text{map}}$ maximum a posteriori estimate of the vector u

$\hat{u}_{\text{y}}$ approximate maximum likelihood estimate of the vector u

u a vector represents discretized spatial attenuation function

$\mathbf{v}$ a vector stores area of triangles

$\hat{v}_{\text{pr}}$ estimate based on flat-field prior

$\hat{v}_{\text{f}}$ arithmetic average of flat-field measurements

$\hat{v}_{\text{y}}$ maximum likelihood estimate of the vector v given measurement y

v flat-field intensity

$w(p)$ the local part of the dissipation energy function

$\mathbf{y}$ random variable associated with tomographic measurements y

y tomographic measurements with an object

y_k measurement vector for the kth time frame

Contents

Introduction

X-ray computed tomography (CT) is a technique to image the internal cross-section without cutting or breaking an object. In 1969, Hounsfield built the first prototype of a CT scanner, and since then, the CT technology has been used extensively in many fields. For example, in medical science for the lung cancer screening, radiation therapy treatments planning, *etc.*, and in material science for detecting material defects, product quality control, *etc.* One of the most popular reconstruction algorithms, used even today in industrial CT scanners, to reconstruct an image from its X-ray images is based on an inverse Radon transform, which was introduced by Johann Radon in 1917, before the invention of the CT technology. In the last 100 years, a lot of efforts have been put into improving the theoretical understanding of the Radon transform; in the last 50 years, we have seen a tremendous development on the theoretical, numerical, and implementation aspects of CT. The industrial and medical applications of CT are rapidly increasing along with advancements in CT hardware, which brings new challenges, research questions and opportunities for mathematicians, industries, doctors, physicists, *etc.*

The standard image reconstruction models are mainly based on the assumption that the object of interest remains stationary during data acquisition in a CT scanner. However, this assumption fails for dynamic CT where the object of interest deforms over time, for example, scanning a beating heart, a drying paint, *etc.* There are numerous industrial and medical applications where the study

of deforming objects is of the prime importance. Dynamic CT reconstruction is a challenging problem because of the interplay between many factors such as the speed of a deforming object, the gantry rotation speed, the number of projections, the detector acquisition time, the scanning protocol, the measurement model, and the reconstruction model.

1.1 Some Challenges in Dynamic CT

In dynamic CT, we aim to reconstruct a sequence of images that represent a deforming object over time. We desire to detect rapid changes over time in addition to detect the smallest spatial features of a deforming object. However, these two basic requirements require a trade-off between the achievable temporal and spatial resolution in dynamic CT. The time gap between two consecutive projections should be short to detect rapid changes in an object and hence to achieve a high temporal resolution. The shorter time gap results in low-intensity measurements due to limited detector acquisition time. The reconstruction based on low-intensity measurements is a challenging problem, in part because of low signal-to-noise ratio (SNR). On the other hand, an increase in the acquisition time limits the total number of projections that can be acquired within the allotted time for an experiment. But, a lower number of projections may introduce limited view or sparse view artifacts and hence limits the achievable spatial resolution. A large number of projections is one of the key requirements to reconstruct an image with a high spatial resolution. Therefore, a resolution trade-off boils down to the trade-off between detector acquisition time and a number of projections within the allotted time for an experiment. In practice, many dynamic CT applications work with low-intensity measurements to acquire many projections in a short period of time. This allows them to use the standard reconstruction models with stationarity assumptions if a deforming object has not deformed much during the acquisition window.

In practice, X-ray detection is a random process. Especially with low SNR measurements (noisy measurements), it is essential that a reconstruction model should be based on a measurement model that take into account the statistical nature of a measurement process. These reconstruction models depend on the X-ray source intensity, but it is never known exactly. It is measured and hence uncertain. Under normal operating conditions, when the acquisition time is sufficiently high, this kind of uncertainty typically has a negligible effect on the reconstruction quality. However, in dose- or time-limited applications such as dynamic CT, this uncertainty may cause severe and systematic artifacts known as ring artifacts. Therefore, a careful modelling of these uncertainties in a reconstruction model is important for dynamic CT applications.

If the acquisition time is high or the object is deforming rapidly, only a few projections are available for reconstruction with the standard reconstruction model with stationarity assumptions. Thus, the reconstruction problem is highly underdetermined. Therefore, it becomes essential to regularize the reconstruction problem by modelling relationship over time either in the image space or in the projection space. We can represent time-dependent changes in the image domain in terms of a deformation map and estimate this along with the unknown object. This is a joint motion estimation and an image reconstruction approach, generally known as a motion-compensated (MC) method. In effect, projections acquired at different instants of time contribute together and improve both the spatial and the temporal resolution of a dynamic CT system.

In most of the MC reconstruction models, one of the key assumptions is the so-called one-to-one correspondence, almost everywhere, among an image sequence that represents a deforming object. The deformation map between images is assumed to be locally invertible and orientation preserving, *i.e.*, no local folding in a material over time. However, this assumption fails if either a crack forms in a material or if a region in a material gets damaged due to X-ray radiations while scanning the material in a scanner. The image sequence will no longer have one-to-one correspondence everywhere, hence called a non-corresponding image sequence. MC reconstruction frameworks with a non-corresponding motion model have not been explored much in the context of dynamic CT.

The MC reconstruction approaches exploit information from the acquired projection data to estimate time-dependent changes in a deforming object. The variability in the projection data determines the quality of an MC reconstruction. Therefore, a strategy to distribute projection views over time, *i.e.*, a view sampling scheme, need to be designed to collect maximum information about the deformation of a deforming object. Recently, it has been shown that an interlaced sampling scheme has great potential over the conventional progressive sampling for dynamic CT. Major interlacing schemes are not a fixed angular sampling (FAS) scheme. In a FAS scheme, view angle between two consecutive projections remains same throughout the experiment, and hence easy to implement in practice. Moreover, the existing interlaced FAS schemes are not suitable to scan fast-moving objects.

1.2 Contributions in the Thesis

This thesis aims to understand and investigate different factors that can influence the quality of dynamic CT reconstructions. In particular, we investigated issues associated with uncertainties due to source intensity measurements, dis-

tribution of projection views over time, and non-corresponding motion models for dynamic CT. We can summarize our contributions in the following three major work:

- Classical methods for X-ray computed tomography are based on the assumption that the X-ray source intensity is known, but in practice, the intensity is measured and hence uncertain. In time-limited applications such as dynamic CT, this uncertainty may cause severe and systematic artifacts known as ring artifacts. By carefully modeling the measurement process and by taking uncertainties into account, we derive a new convex model that leads to improved reconstructions despite poor quality measurements. We demonstrate the effectiveness of the methodology based on simulated and real datasets.

  Related Paper:
  Hari Om Aggrawal, Martin Skovgaard Andersen, Sean Rose, and Emil Y. Sidky. "A Convex Reconstruction Model for X-ray Tomographic Imaging with Uncertain Flat-fields". IEEE Transactions on Computational Imaging, Volume 4, Issue 1, March 2018.

- Conventional motion models are based on the assumption that the deformation map is continuously differentiable and has a one-to-one correspondence almost everywhere. However, these motion models fail for discontinuous deformations, *e.g.*, a crack formation, and non-smooth continuous deformations, *e.g.*, a closing of a crack. We derive a motion model in an image registration framework based on the underlying physics of a crack formation in a material. The proposed model identifies the location of a crack as well as regularizes non-smooth and large deformations along the crack region with minimal influence on deformations in nearby regions. We demonstrate the effectiveness of the methodology based on intensity-preserving and mass-preserving simulated data sets.

- In dynamic CT, the distribution of projection views over time, particularly based on an interlacing sampling scheme, influences the quality of images reconstructed with a motion-compensated reconstruction model. Major interlacing schemes are not a fixed angular sampling (FAS) scheme, hence not easy to implement in practice. Moreover, the existing interlaced FAS schemes are not suitable to scan fast-moving objects. In this work, we propose an interlaced FAS scheme based on the family of metallic angles. This scheme guarantees an aperiodic pattern and it is suitable to scan fast-moving objects due to small and adjustable angular gaps between consecutive projections. We conduct a preliminary study and demonstrate that the proposed scheme substantially enhances the quality of images reconstructed with a motion-compensated reconstruction model based on simulated datasets.

1.3   Structure of the Thesis

Chapter 2 and 3 provide the basic background information to understand re-
maining chapters of this thesis. They also cover a brief literature survey associ-
ated with challenges addressed in chapter 4 and 6. In chapter 2, we introduce
the fundamentals of X-ray computed tomography. We give a brief overview of
X-ray measurement models with their underlying assumptions, discuss recon-
struction models and methods, their inherent ill-posedness, and an approach to
regularize the problem. We discuss the underlying cause of a systematic artifact
known as ring artifacts in the reconstruction. We also present state-of-the-art
methods to mitigate ring artifacts in the reconstruction. In chapter 3, we intro-
duce dynamic CT and motivate motion modelling for dynamic CT. We provide
the basic definitions of spatial and temporal resolution in the context of dy-
namic tomography and motivate the role of a sampling scheme to achieve high
spatio-temporal resolution. We present a general motion model in an image
registration framework and discuss state-of-the-art motion-compensated recon-
struction models based on image registration models. We also discuss in brief
other temporal regularization methods for dynamic CT.

Chapter 4, 5, and 6 cover the main contributions of this thesis. Chapter 4
addresses challenges associated with uncertainties due to source intensity mea-
surements. We review some existing approaches to CT reconstruction based on
low SNR measurements. We illustrate the sensitivity of these existing meth-
ods to flat-field intensity estimation errors. We derive a new reconstruction
model that accounts for uncertainties in flat-field measurements. We describe
our numerical investigation and validate the proposed model based on simulated
data as well as on real tomographic measurements. In chapter 5, we develop
a non-corresponding image registration model with a special focus on images
with cracks. We introduce two non-corresponding problems with their under-
lying physical characteristics. We propose an image registration model, mainly
inspired from the field of damage mechanics, to solve the non-corresponding
problems. We also discuss general properties of the proposed model and es-
tablish a connection with the state-of-the-art non-corresponding models. We
explain a numerical scheme based on the discretize-then-optimize framework
and demonstrate the potential of the proposed model based on an intensity-
preserving and a mass-preserving simulated image phantoms. In chapter 6,
we propose an interlaced sampling scheme based on the family of metallic an-
gles. We develop an implicit reference based motion-compensated reconstruction
model assuming the one-to-one correspondence everywhere. We conduct a pre-
liminary study and demonstrate the effectiveness of the proposed scheme with
the motion-compensated reconstruction model based on simulated datasets.

X-ray Computed Tomography

X-ray computed tomography (CT) is a non-invasive method that is used to image the internal structure of objects without cutting or breaking them. In a CT scanner, the X-ray source illuminates an object from different projection directions while detectors capture the attenuated X-rays as shown in Fig. 2.1(a). As X-rays propagates through the object along straight lines, they attenuate exponentially with a rate of decay that depends on the material attenuation function $\mu(x)$, following the Lambert–Beer law. Specifically, the incident intensity of the X-ray beam on a detector is given by

$$I \approx \eta T_e I_0 \exp \left(- \int_l \mu(x) \, dx \right) \tag{2.1}$$

where $\eta \in (0, 1]$ is the detector efficiency, T_e is the detector acquisition time, I_0 is the photon flux of the X-ray source, and l denotes the line segment between the source and a detector. The description in (2.1) assumes a monochromatic source and does not take into account the scatter contributions, the detector crosstalks, the finite size of the detector, the statistical nature of the photon arrival process into account, *etc.*[Nuyts13]. Let v is the flat-field intensity given by

$$v = \eta T_e I_0, \tag{2.2}$$
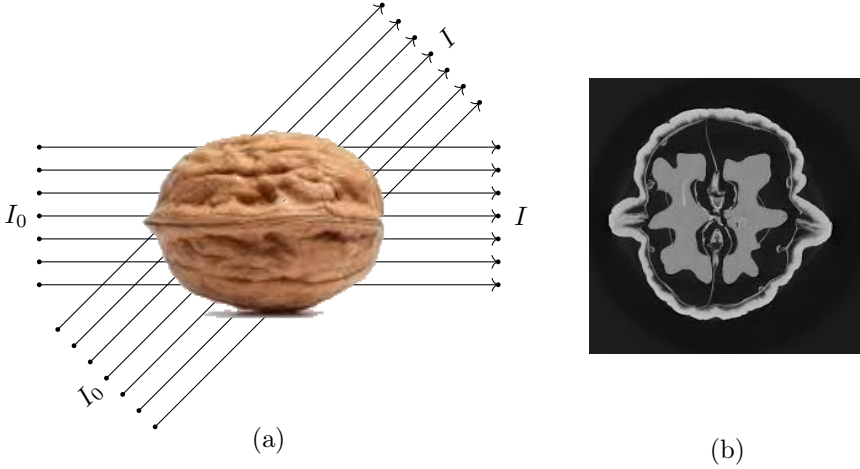
Figure 2.1: (a) a setup to illustrates the tomographic scanning of a walnut from different projection directions. (b) a cross-sectional reconstruction of the walnut from tomographic measurements.

and $t_l(\mu)$ is the transmission function given by

$$t_l(\mu) = \exp\left(-\int_l \mu(x)\,dx\right). \tag{2.3}$$

We represent the equation (2.1) as

$$R\mu(l) = -\log\frac{I}{v} \approx \int_l \mu(x)\,dx \tag{2.4}$$

where the function $R\mu(l)$ is known as the Radon transform of the function $\mu(x)$ along the line l. The Radon projections collected from multiple directions is also known as a sinogram because the Radon transform of an off-centered point in an object has a sinusoidal pattern due to the circular scanning around the object. The inverse Radon transform is the basis of major X-ray CT reconstruction models, see *e.g.* [Buzug08]. Reconstruction methods estimate the spatial attenuation of the object of interest based on the number of Radon projections, given the measurement geometry, the source intensity, and possibly some assumptions on the statistical nature of the measurement process. For example, Fig.2.1(b) shows a two-dimensional cross-section of a walnut reconstructed from the inverse Radon transform of the Radon projections.

In practice, X-ray photon arrival is a random process. Section 2.1 explains underlying measurement models that take statistical nature of measurements into account. Section 2.2 introduces the basic definition of an inverse problem

and regularization briefly. Section 2.3 discusses various reconstruction models and methods associated with measurement models as discussed in Section 2.1, comments on their inherent ill-posedness, and explains approaches to regularize the problem. In the last section 2.4, we discuss the underlying cause of systematic artifacts known as ring artifacts. We also present state-of-the-art methods to mitigate ring artifacts in a reconstruction. For in-depth description of topics covered in this chapter, the reader is suggested to see [Prince15; Hansen10; Buzug08; Kak01; Bertero98].

2.1 X-ray Photon Statistics

For photon-counting detectors, it is common to assume that the photon arrival process is a Poisson process, and each measurement is assumed to be a sample from a Poisson distribution whose mean is prescribed by the Lambert–Beer law. However, for current integrating detectors, as in the current clinical X-ray CT systems, measurements statistics are relatively complicated than for the photon-counting detectors. X-ray photons statistics depends on many factors which are encountered in the transmission chain from the X-ray source to a detector. Few of the variability sources are the fluctuation of an X-ray tube current, energy of photons, scattering or absorption inside an object, Compton scattering or photoelectric absorption in the detector, scintillator photo-conversion, electronic noise, quantization error, *etc*. Ideally, a "Poisson + Gaussian" model is considered as a reasonable noise model for measurements as discussed in [Nuyts13].

In this thesis, we discuss the measurement model for the photon-counting detectors without any electronic noise. Thus, with the assumption that the arrival process is Poisson process, measurement y is a realization of a random variable $\mathbf{y}$ which, conditioned on μ and v, is a Poisson random variable whose mean is prescribed by the Lambert–Beer law, *i.e.*,

$$\mathbf{y} \mid \mu, v \sim \text{Poisson}\left(v \cdot t_l(\mu)\right) \tag{2.5}$$

or equivalently, the probability distribution $\text{P}(y \mid \mu, v)$ is given by

$$\text{P}(y \mid \mu, v) = \frac{1}{y!}(v \cdot t_l(u))^y \exp(-v \cdot t_l(u)) \tag{2.6}$$

where the expected mean of $\mathbf{y}$ is $\mathsf{E}[\mathbf{y}] = v \cdot t_l(u)$.

The coefficient of variation (CV) measures the dispersion of a random variable in relation to its mean value; it is defined as the ratio of the standard deviation to the mean. The CV of a Poisson distribution for the random variable $\mathbf{y}$ is

given by

$$\mathrm{CV} = \frac{1}{\sqrt{v \cdot t_l(\mu)}} = \frac{1}{\sqrt{\eta T_e I_0 \cdot t_l(\mu)}}.$$

The above definition signifies that the relative noise level in a measurement increases with either the decreasing photon flux or the decreasing acquisition time or both. Therefore, problems may arise in dynamic tomography where the detector acquisition time is limited and in applications where a strict dose is required such as for the diagnosis of patients. The relative noise level also depends on the attenuation function of the object of interest.

It can be shown that the measurement y approximately satisfies a Gaussian distribution when the incident photon flux on the detector is high [Buzug08], *i.e.*,

$$\mathbf{y} \mid \mu, v \sim \mathcal{N} \left(v \cdot t_l(\mu), v \cdot t_l(\mu) \right) \tag{2.7}$$

where the mean and variance of the random variable $\mathbf{y}$ are equal, and the probability distribution of y is given by

$$\mathrm{P}(y \mid \mu, v) = \frac{1}{\sqrt{2\pi v \cdot t_l(\mu)}} \exp \left(-\frac{(y - v \cdot t_l(\mu))^2}{2v \cdot t_l(\mu)} \right). \tag{2.8}$$

It is possible to calculate the probability distribution of the log-normalized projection data

$$b = -\log \left(\frac{y}{v} \right). \tag{2.9}$$

by utilizing the following result [Papoulis02, Chapter 5]:

Suppose that $\mathbf{x}$ is a random variable with probability distribution $\mathrm{P}_x(x)$ and $\mathbf{z}$ is an another random variable, defined as $\mathbf{z} = g(\mathbf{x})$. The probability distribution of $\mathbf{z}$ is given by

$$\mathrm{P}_z(z) = \sum_{i=1}^{n} \frac{\mathrm{P}_x(x_i)}{|g'(x_i)|} \tag{2.10}$$

where $g'(x)$ is the derivative of $g(x)$ and $x_1, x_2, \ldots, x_n$ are the real roots of equation $z = g(x)$.

The probability distribution of the random variable $\mathbf{b} = -\log(\mathbf{y}/v)$, utilizing the result (2.10) is given by

$$\begin{aligned} \mathrm{P}_b(b) =& v \exp(-b) \mathrm{P}_y(v \exp(-b)) \\ =& \sqrt{\frac{v}{2\pi \cdot t_l(\mu)}} \exp(-b) \exp \left(-\frac{(v \exp(-b) - v \cdot t_l(\mu))^2}{2v \cdot t_l(\mu)} \right). \end{aligned} \tag{2.11}$$

After replacing the $\exp(-b)$ by its first order Taylor approximation at $\int_l \mu(x)\, dx$, *i.e.*,

$$\exp(-b) \approx \exp\left(-\int_l \mu(x)\, dx\right) - \exp\left(-\int_l \mu(x)\, dx\right)\left(b - \int_l \mu(x)\, dx\right), \quad (2.12)$$

the expression (2.11) can be approximated as

$$P(b) \approx \sqrt{\frac{v \cdot t_l(u)}{2\pi}} \exp\left(-\left(b - \int_l \mu(x)\, dx\right) - (v \cdot t_l(u))\frac{(b - \int_l \mu(x)\, dx)^2}{2}\right). \tag{2.13}$$

We can also determine the probability distribution of the random variable $\mathbf{b}$ by linearizing the expression (2.9) using Taylor expansion at the mean value of the random variable $\mathbf{y}$, *i.e.*,

$$\mathbf{b} \approx -\log\frac{v \cdot t_l(u)}{v} - \frac{1}{v \cdot t_l(u)}(\mathbf{y} - v \cdot t_l(u))$$

$$= \left(1 + \int_l \mu(x)\, dx\right) - \frac{1}{v \cdot t_l(u)}\mathbf{y}. \tag{2.14}$$

This is a good approximation for large values of $v \cdot t_l(u)$ as the higher order terms of the Taylor expansion are small. The approximated function (2.14) is a linear function of $\mathbf{y}$, therefore, assuming the random variable $\mathbf{y}$ has a Gaussian distribution as defined in (2.7), the random variable $\mathbf{b}$ also has a Gaussian distribution, *i.e.*,

$$\mathbf{b} \sim \mathcal{N}\left(\int_l \mu(x)\, dx,\ \frac{1}{v \cdot t_l(u)}\right) \tag{2.15}$$

or equivalently, the approximated probability distribution of $\mathbf{b}$ is given by

$$P(b) = \sqrt{\frac{v \cdot t_l(u)}{2\pi}} \exp\left(-(v \cdot t_l(u))\frac{(b - \int_l \mu(x)\, dx)^2}{2}\right). \tag{2.16}$$

It can be seen that the approximated probability distribution (2.13) has one extra linear term in the exponential compared to the approximated probability distribution (2.16). Fig. 2.2 displays the probability distributions (2.11), (2.13), and (2.16) to illustrate the goodness of approximations. The approximations are good at higher photon flux on the detector.

2.2   Inverse Problem and Regularization

A forward problem is concerned with the effect of a physical system due to the known cause, and an inverse problem is associated with the identification of
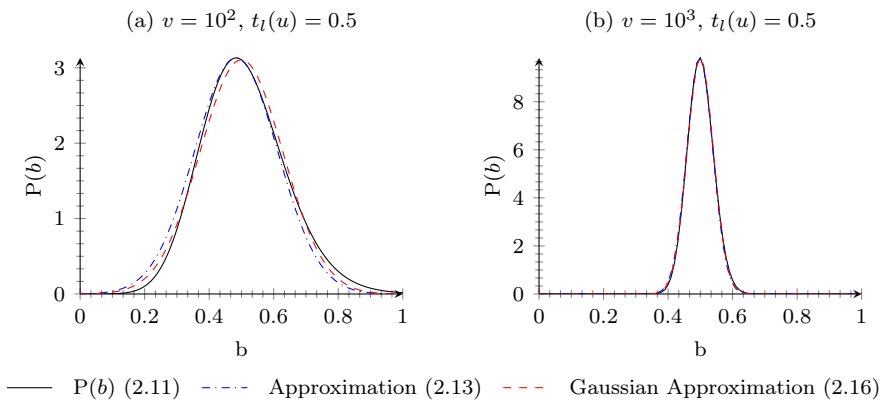
Figure 2.2: Probability distribution of a log-normalized projection data and its two approximations at two values of flat-field intensity, *i.e.*, $v = 10^2$ and $v = 10^3$, assuming transmission function $t_l(u)$ is fixed at 0.5. The approximations are good at higher photon flux on the detector.

the cause from its effects. For example, in computed tomography, estimation of an attenuation function from measurements is an inverse problem. The forward problem is the computation of line integrals with the knowledge of the attenuation function of a material.

The French mathematician Jacques Hadamard introduced three requirements that must be satisfied by a well-posed problem. These are:

- Existence: The problem should have at least one solution,

- Uniqueness: The solution should be unique, and

- Stability: The solution must depend continuously on data.

A problem which does not satisfy all of the properties as mentioned above is considered as an ill-posed problem. Inverse problems are typically ill-posed. Majorly, ill-posed problems do not satisfy the third requirement. As a result, low-level noise in the measured data may produce high-frequency fluctuations in the naive solution of an ill-posed inverse problem. Therefore, instead of looking for the naive solution which might be unacceptable, we look for an approximate solution close to a physically acceptable solution. To achieve this, we provide additional information about the physical system which expresses the expected properties of the solution; this is an underlying principle of a regularization

method. In the next section, we discuss the ill-posedness of inverse problems associated with X-ray CT reconstruction models.

2.3 Reconstruction Models and Methods

In this section, we present an analytical reconstruction model based on the measurement model (2.1) and discuss a regularization approach to handle the ill-posedness of the problem. Afterwards, we present a linear reconstruction model based on the measurement model (2.1) and discuss issues related to the discretization, ill-posedness, and regularization of the problem. We also present a statistical reconstruction model based on Bayesian methods where measurements and a priori information are assumed to be of a statistical nature.

2.3.1 Analytical Reconstruction Methods

According to the well-known Fourier slice theorem, the one-dimensional Fourier transform of a Radon projection data acquired from the direction θ is a slice of the two-dimensional Fourier transform of the original object along a radial line corresponds to the direction θ. Therefore, if the Radon projections are available from all the directions in a full or half rotation, we can reconstruct the object uniquely by performing a two-dimensional inverse Fourier transform. If we let $x = \rho n_\phi$, where $n_\phi = (cos\phi, sin\phi)$ such that $|\rho|$ is the distance to the origin, the inverse Radon transform is given by

$$\mu(x) = \frac{1}{2} \int_{-\pi}^{\pi} \int_{-\infty}^{\infty} |\zeta| H_\theta(\zeta) \exp^{i2\pi\zeta\rho n_\phi^T n_\theta} \, d\zeta d\theta \qquad (2.17)$$

where $H_\theta(\zeta)$ is the Fourier transform of the Radon data in the direction θ. The high-pass ramp filter $|\zeta|$ arises due to the change of variables in the formulation, and it reflects the filtering of the Fourier transform of the Radon data before the actual inversion. The ramp filter $|\zeta|$ amplifies the high-frequency noise in the measured data which generally result in an unacceptable reconstruction. We reach the similar conclusion by analysing the singular value decay of the Radon transform operator; the singular values decay slowly to zero, *i.e.*, $\sigma \propto 1/\sqrt{m}$ for large m. As a consequence, the Picard criterion is not satisfied by an arbitrary Radon data [Bertero98], and small singular values introduce high-frequency noise in the reconstruction. To mitigate this problem, a low-pass filter $W_Z(|\zeta|)$, characterized by a cut-off frequency Z, is introduced in the equation

(2.17), and a regularized analytical reconstruction formula is given by

$$\mu(x) = \frac{1}{2} \int_{-\pi}^{\pi} \int_{-\infty}^{\infty} |\zeta| W_Z(|\zeta|) H_\theta(\zeta) \exp^{i2\pi\zeta\rho n_\phi^T n_\theta} d\zeta d\theta. \qquad (2.18)$$

which is the basis of the filtered backprojection (FBP) algorithm. The FBP algorithm mainly consists of the following steps:

- for each value of θ, compute the Fourier transform of Radon data as defined in (2.4),

- apply the ramp filter along with the low-pass filter,

- compute the inverse Fourier transform to obtain a filtered projection,

- backproject the filtered projections from all directions in the image space and sum them up.

The measurement model (2.4) is the basis for FBP algorithm; however, the measurement model (2.5) reflects the underlying physics of measurements in practice. Nevertheless, the FBP algorithm works satisfactory at high photon counts, but it does not perform well for low dose applications and for dynamic CT where acquisition time is limited. Moreover, FBP algorithm assumes a continuum of projections from all the directions. Therefore, in practice, we need a large number of projections, and as a result, the total radiation dose administered to an object increases drastically. However, iterative reconstruction methods require a finite number of projections to achieve a high-quality reconstruction. Moreover, the algebraic or statistical reconstruction models provide flexibility to reconstruct images from arbitrary X-ray system geometries and allow a better modelling of real physical measurement processes and makes it possible to include prior information about the object in the reconstruction model [Nuyts13]. Most importantly, FBP is a computationally fast algorithm and has low memory footprint. Therefore, FBP is still a widely used algorithm in industrial CT scanners.

2.3.2   Algebraic Reconstruction Methods

In this section, we discuss reconstruction models based on the measurement model (2.1). But instead of the analytical approach as discussed in the previous section, we discretize the expression (2.1) and represent the model as a linear system of equations. We use the notation I_{ij} to denote the measurement obtained with detector elements i and projection j, and express the measurement

model (2.1) as

$$b_{ij} = -\log \frac{v_i}{I_{ij}} = \int_{l_{ij}} \mu(x)\, dx, \tag{2.19}$$

where b represents the log-normalized projection data and $v = \eta T_e I_0$ is referred as the flat-field intensity.

The attenuation function $\mu(x)$ may be discretized by using a parameterization, *i.e.*,

$$\mu(x) = \sum_{k=1}^{n} u_k \mu_k(x) \tag{2.20}$$

where $\mu_k(x)$ is one of n basis functions (*e.g.*, a pixel or voxel basis), and $u \in \mathbb{R}^n$ is a vector of unknowns (*e.g.*, pixel or voxel values). With this parameterization, the line integrals in (2.19) can be expressed as

$$\int_{l_{ij}} \mu(x)\, dx = e_i^T A_j u$$

where the elements of the matrix $A_j \in \mathbb{R}^{r \times n}$ are given by

$$(A_j)_{ik} = \int_{l_{ij}} \mu_k(x)\, dx,$$

and the system matrix $A \in \mathbb{R}^{rp \times n}$ is defined as $A = [A_1^T \cdots A_p^T]$. Hence, the measurement model (2.19) is expressed as

$$b = Au \tag{2.21}$$

where $b \in \mathbb{R}^{rp \times 1}$.

The model (2.21) is a linear reconstruction model, but an ill-posed inverse problem. Generally, the system matrix A is an ill-conditioned matrix whose singular values slowly decay to zero, and matrix has a large condition number. As a result, a small change in the data may cause a large error in the solution of the equation (2.21). The ill-posedness of such a linear system has been studied extensively using singular value decomposition (SVD) analysis, *e.g.*, see [Hansen10].

If the number of rows is more than the number of columns in the system matrix A, and the system is inconsistent, no solution satisfies the linear system. A problem is inconsistent when the measurement vector b does not belong to the range of the matrix A. This scenario does not satisfy Hadamard's requirement

of the existence of a solution for a well-posedness problem, but we can fix this by reformulating the problem as a linear least squares problem, *i.e.*,

$$\underset{u}{\text{minimize}} \frac{1}{2}\|Au - b\|_2^2. \tag{2.22}$$

The linear least squares problem only guarantees a solution, but it could be highly noisy due to the ill-conditioning of the system matrix. In general, the linear least squares problem has a unique solution if A is a full column rank matrix. In the case of a rank-deficient matrix, there will be infinitely many solutions. We can further reformulate the problem and choose a minimum norm solution out of all possible solutions. This fixes the uniqueness requirement of Hadamard for a well-posed problem.

In order to regularize the problem, we impose additional properties of the solution by adding a regularization term $\mathrm{R}(u)$, *i.e.*,

$$\underset{u}{\text{minimize}} \frac{1}{2}\|Au - b\|_2^2 + \gamma \mathrm{R}(u). \tag{2.23}$$

In the case of the Tikhonov regularization $R(u) = 0.5\|u\|_2^2$, we regularize the problem by penalizing the 2-norm of a solution to avoid large variations in the solution due to the noise in the measurements. The regularization parameter γ balances the contributions from the so-called data fidelity term $\|Au - b\|_2^2$ and the regularization term. The larger the γ, the more weight is given to the regularity of a solution, and smaller the γ, higher would be the influence of noise in the solution.

The choice of a regularization parameter depends on subjective expectations from the solution of a problem, and for real-world applications, it is difficult to quantify the expectation numerically based on some specific criteria. Moreover, it could be computationally intensive to solve the problem multiple times with different regularization parameters. There are few parameter choice methods such as the discrepancy principle method which relies on a good estimate of noise in the measured data and the L-curve method balances regularization errors and perturbation errors in the given problem, see [Hansen10] for more details.

In practice, the system matrix A is a very large sparse matrix; therefore iterative methods are the method of choice to solve the large linear systems, instead of numerical methods based on SVD. The iterative method such as algebraic reconstruction technique (ART), also known as a Kaczmarz's method is a row-action method where one row is being used at a time to update the solution. However, iterative methods such as Landweber, SART, SIRT, and gradient descent use all rows simultaneously in an iteration. These iterative methods exhibit semi-convergence where the iteration sequence initially approaches the exact solution,

after which it starts to deviate and converge to an undesired naive solution. Generally, row-action methods have faster convergence to a semi-convergence point than the fully simultaneous methods. The initial iterates from the fully simultaneous methods are generally smoother than the iterates from row-action methods.

2.3.3 Statistical Reconstruction Methods

The arrival of photons is a random process as we discussed before in section 2.1. Recall that the measurement y is a random variable in the measurement model (2.5). Statistical methods provide a framework to take into account the random nature of a variable through its statistical properties such as probability distribution. The maximum likelihood estimation (MLE) method estimates the parameters of a statistical method given the random measurements. We define a likelihood function

$$\mathcal{L}(\mu) = \mathrm{P}(y \mid \mu, v)$$

of the spatial attenuation function μ given the measurements y and flat-field intensity v. The MLE estimate of μ is given by

$$\hat{\mu}_{ml} = \underset{\mu}{\operatorname{argmax}} \, \mathrm{P}(y \mid \mu, v).$$

The MLE estimate $\hat{\mu}_{ml}$ maximizes the probability of obtaining the observed measurements. In practice, it is convenient to work with the logarithm of the likelihood function. The maximum of a log-likelihood function coincides with the maximum of the likelihood function because logarithm is a strictly increasing function.

If a priori information about the attenuation function is known in the form of a prior probability distribution $\mathrm{P}(\mu)$, we can define a posterior distribution using Bayes' rule, *i.e.*,

$$\mathrm{P}(\mu \mid y) = \frac{\mathrm{P}(y \mid \mu)\mathrm{P}(\mu)}{\mathrm{P}(y)} \tag{2.24}$$

and obtain a maximum a posteriori probability (MAP) estimate which is given by

$$\hat{\mu}_{map} = \underset{\mu}{\operatorname{argmax}} \, \mathrm{P}(\mu \mid y).$$

The MAP estimate is a point estimate and equal to the mode of the posterior distribution. Thus, the MAP method does not give any information about the uncertainity around the MAP estimate.

Let us consider a two-dimensional geometry where p projections are acquired using a one-dimensional detector array with r detector elements. We follow notations and discretization steps as described in section (2.3.2) and assume that the log-normalized projection data b_{ij} follows a Gaussian distribution, as defined in (2.16), *i.e.*,

$$\mathbf{b}_{ij} \mid u, v_i \sim \mathcal{N}\left(e_i^T A_j u, \ \frac{1}{v_i \exp(-e_i^T A_j u)}\right). \tag{2.25}$$

and the joint probability of $b = (b_{11}, \ldots, b_{rp})$ is given by

$$\mathrm{P}(b \mid u) = \prod_{i=1}^{r} \prod_{j=1}^{p} \mathrm{P}(b_{ij} \mid u) \tag{2.26}$$

assuming all measurements are independent. This is also called the likelihood of u given measurements b. Suppose, a prior distribution of u follows

$$u \sim \mathcal{N}(0, \gamma^{-1} I), \tag{2.27}$$

we can define a MAP estimation problem, using Bayes' rule (2.24),

$$
\begin{aligned}
\hat{u}_{map} &= \underset{u}{\mathrm{argmax}}\, \mathrm{P}(u \mid b) \\
&= \underset{u}{\mathrm{argmax}}\, \mathrm{P}(b \mid u)\mathrm{P}(u) \\
&= \underset{u}{\mathrm{argmin}} - \log \mathrm{P}(b \mid u)\mathrm{P}(u) \\
&= \underset{u}{\mathrm{argmin}} \sum_{i=1}^{r} \sum_{j=1}^{p} -\log \mathrm{P}(b_{ij} \mid u) - \log \mathrm{P}(u) \\
&= \underset{u}{\mathrm{argmin}} \frac{1}{2}\|Au - b\|_W^2 + \frac{\gamma}{2}\|u\|_2^2
\end{aligned}
\tag{2.28}
$$

where $W = \mathrm{diag}(\mathrm{diag}(1 \otimes v) \exp(-Au))$. Assuming $W \approx \mathrm{diag}(y)$, the estimation problem (2.28) is known as a weighted least-squares problem for X-ray CT. Assuming $W = I$, the formulation (2.28) gives a Bayesian interpretation of the least-squares problem with the Tikhonov regularization, as defined in (2.23), where $R(u) = 0.5\|u\|_2^2$.

2.4 Flat-field Estimation Errors and Ring Artifacts

Please note that a large part of this section has been published in the IEEE journal:

In practice, the flat-field intensity $v = \eta T_e I_0$ is never known exactly, but it is estimated by acquiring a number of X-ray images without an object in the scanner. Such measurements are also known as air scans [Whiting06], flat-fields, or white-fields[Sijbers04]. We assume that s flat-field measurements are acquired for each detector element based on the flat-field measuring model

$$\mathbf{f}_{ij} \mid v_i \sim \text{Poisson}(v_i) \tag{2.29}$$

for $i = 1, \ldots, r$ and $j = 1, \ldots, s$, and $\mathbf{F}$ denotes a $r \times s$ matrix random variable with elements $\mathbf{f}_{ij}$. The matrix $F \in \mathbb{R}^{r \times s}$ denotes a realization of $\mathbf{F}$. A maximum likelihood (ML) estimate of v is given by

$$\hat{v}_{\text{f}} = \underset{v}{\text{argmin}} \left\{ -\log \mathrm{P}(F \mid v) \right\} \tag{2.30}$$

$$= \underset{v}{\text{argmin}} \left\{ s\mathbf{1}^T v - \mathbf{1}^T F^T \log(v) \right\} = \frac{1}{s} F\mathbf{1},$$

The flat-field estimate $\hat{v}_{\text{f}}$ is simply an elementwise mean of s flat-field measurements which is generally used to compute reconstructions. The $\hat{v}_f$ is in itself a random variable whose variance is given by

$$\text{var}(\hat{v}_{\text{f}}) = \frac{v}{s}.$$

Consequently, the signal-to-noise ratio (SNR) of the flat-field intensity estimate is proportional to the square root of the product of the flat-field intensity and the number of samples. Therefore, if the flat-field intensity is low or if the number of flat-field measurements is small, the flat-field estimation error may be significant and lead to reconstruction artifacts and errors. Since the flat-field estimate is used to normalize measurements from all projection directions, the estimation errors result in systematic reconstruction errors. These are known as ring artifacts[Kowalski77] since they appear as concentric circles superimposed on the reconstruction, and they are a common problem that can mask important features in the reconstructed image [Thomas10; Dahlman12]. Ring artifacts may not only occur because of flat-field estimation errors; miscalibrated or dead detector elements and non-uniform sensitivities may also systematically corrupt the measurements and lead to ring artifacts in the reconstruction [Sijbers04].

An experimental study [Fahrig06] has pointed out that the ring artifacts are more severe when the X-ray source intensity is low, and hence a reconstruction from low-intensity measurements may be very sensitive to the assumptions upon

which the reconstruction method is based. The problem may arise when the acquisition time is limited, *e.g.*, in dynamic or time-resolved tomography, or if the application imposes strict dose limitations. Thus, tomographic reconstruction based on low-intensity measurements is a challenging problem, in part because of the low SNR.

We now demonstrate the effect of flat-field estimation errors on the reconstruction based on the analytical reconstruction method (2.18). We use a constant flat-field intensity $v = \omega \mathbf{1}$ for $\omega > 0$ to generate a set of measurements according to the model (2.1) with $r = 185$ detector elements and $p = 360$ parallel beam projections covering a half rotation. For the reconstruction we use the flat-field ML estimate $\hat{v}_\mathrm{f}$, as defined in (2.30), where only one flat-field sample ($s = 1$) is acquired for all detector elements based on (2.29).

Our object u, shown in Fig.2.3(b), consists of three squares of different sizes where the attenuation of the innermost square is 0.5 cm^{-1}, the enclosing square has attenuation 0.25 cm^{-1}, and the outermost square has no attenuation. The domain size is 1 cm, and the reconstruction grid is 128×128 pixels. Fig. 2.3 shows sinogram as defined in (2.4) and analytical reconstructions based on (2.18) with different values of the parameter ω. The effect of the flat-field error appears as a line in the sinogram and as rings in the reconstructions. It is clear that the severity of rings in the reconstructions and lines in the sinogram decreases with the increasing flat-field intensity.

One approach to combating ring artifacts is to move the detector array between projections [Doran01]. This has an averaging effect on the systematic error due to flat-field estimation errors and often results in noticeable improvements, but it does not address or model the underlying cause. Moreover, it requires special hardware for the acquisition, and it is not suited for applications such as dynamic CT where fast acquisition times are important. Alternative software-based methods to mitigate ring artifacts also exist. Roughly speaking, these methods can be put into three categories: sinogram preprocessing methods [Kowalski78; Raven98; Münch09; Rashid12; Kim14], combined ring reduction and reconstruction methods [Paleo15; Mohan15], and post-processing methods that reduce or remove rings from a reconstruction [Sijbers04; Prell09; Yan16]. The preprocessing methods detect and remove/reduce stripes in the sinogram which, in turn, reduces the ring artifacts in the image domain. These algorithms are typically based on Fourier domain filtering [Raven98], wavelet domain filtering[Münch09], or a normalization of measurements by estimating the sensitivity of each detector pixel [Kim14]. The post-processing methods transform the reconstructed image from Cartesian to polar coordinates [Sijbers04] and remove stripes using, *e.g.*, a median filter[Prell09], a wavelet filter, or a variational model for destriping [Yan16].

(a) Radon transform/Sinogram of Phantom

(b) Phantom

(c) Sinogram error plot, $\omega = 10$

(d) $\omega = 10$, Reconstruction

(e) Sinogram error plot, $\omega = 10^2$

(f) $\omega = 10^2$, Reconstruction

(g) Sinogram error plot, $\omega = 10^3$

(h) $\omega = 10^3$, Reconstruction
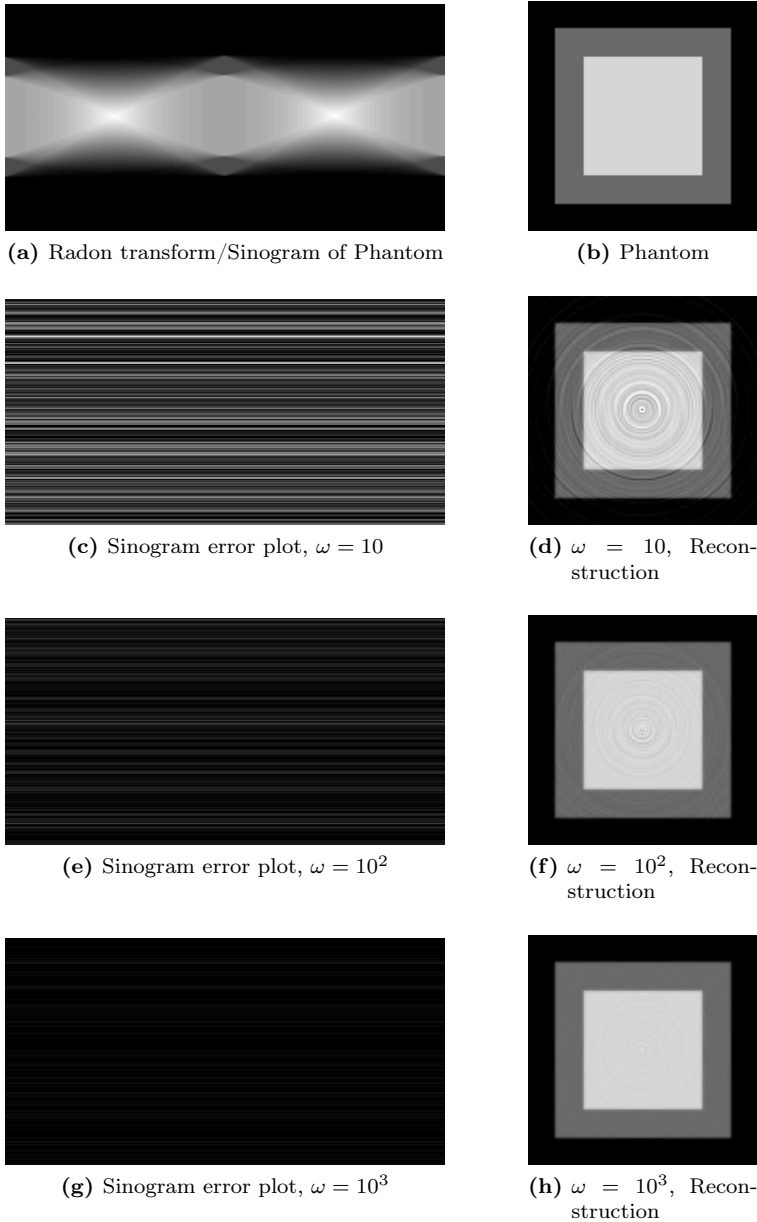
Figure 2.3: (a) Radon transform of the phantom (b). Figures (c), (e), and (g) show sinogram error plots that represent the flat-field estimation errors in the sinogram domain. We generate them by subtracting the true Radon transform, as shown in (a), from the sinogram with flat-field errors. Figures (d), (f), and (h) shows images reconstructed with sinograms having flat-field errors. The display range for the sinogram error plots is $[0, 1]$. The display range for phantom and the reconstructed image is $[0, 0.6]$.

In two recently proposed methods [Mohan15; Paleo15], ring artifact correction is included as an intrinsic part of the reconstruction process. Motivated by the cause of ring artifacts, which appear as stripes in the sinogram domain, the sinogram is split into the sum of the true sinogram and a component which represents the systematic stripe errors. Although the combined ring-reduction and reconstruction methods do take the systematic nature of the flat-field estimation errors in the sinogram domain into account, they do not explicitly model the source of the errors nor their statistical properties.

Existing methods for mitigating ring artifacts have been shown to work reasonably well when applied to measurement data with high or acceptable SNRs. However, we are not aware of any studies that investigate ring artifact correction for low SNR measurements and where the intensity of X-ray beam is assumed to be uncertain. To this end, in chapter 4, we derive a new reconstruction model that is based on a rigorous statistical description of our model assumptions. Unlike existing correction methods that, roughly speaking, are based on the geometric nature of ring artifacts in either the sinogram or the reconstruction, our approach is based on a model of one possible cause of these artifacts.

2.5   Summary

X-ray measurements are assumed to be samples of a Poisson random variable for photon-counting detectors where the Lambert–Beer law defines the underlying physics behind X-ray propagation through a material. If photon flux is high, we can approximate the statistical nature of measurements by a Gaussian distribution. Based on these different measurement models, we can define several reconstruction models for X-ray CT. The analytical reconstruction method FBP and algebraic reconstruction methods do not take into account the statistical nature of X-ray measurements. The Bayesian statistical methods provide a framework to take into account the random nature of X-ray measurements. The statistical methods based on the Poisson measurement model are mostly suitable for problems where low-intensity measurements are unavoidable, *e.g.*, in dynamic CT. Moreover, flat-field intensity estimates based on low-intensity measurements are highly uncertain. The uncertainty may cause severe and systematic artifacts, known as ring artifacts, in the reconstructions. The existing methods are, roughly speaking, based on the geometrical nature of these artifacts either in the image space or the sinogram space. These methods do not consider the underlying cause of ring artifacts, *i.e.*, the flat-field estimation error.

Dynamic X-ray Computed Tomography

Dynamic CT is a technique to image the internal cross-section of a deforming object without cutting and breaking it, *e.g.*, a pill dissolving in a liquid, a beating heart, *etc.* [Flohr16; Mokso15; Flohr15; McClelland13; Cnudde13; Pinzer12; Heindel11; Bonnet03]. The deforming object may change its shape as well as its attenuation coefficient over time. Fig. 3.1 displays some physical states of a deforming object where the object changes its shape over time.

u_{t_0} u_{t_1} u_{t_2} u_{t_3}
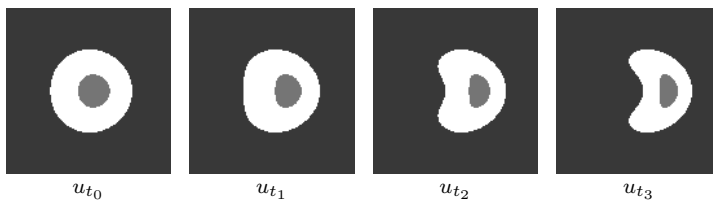
Figure 3.1: Image sequence of a dynamic phantom. u_t denotes the attenuation function of an object at time t.

The underlying physics behind X-ray imaging is the same whether the object of interest is stationary or deforming during the data acquisition. However, CT scanners, data acquisition schemes, and reconstruction models for dynamic CT

may differ from time-invariant tomography in order to achieve a high spatio-temporal resolution. In time-invariant tomography, the object of interest is assumed to be stationary during the data acquisition as discussed in chapter 2.

The temporal resolution depends on the scan time, *i.e.*, the time to acquire projections over a full rotation for one image frame. The conventional CT system has one X-ray source and an array of detectors. The centripetal force acting on the rotating frame of a CT scanner limits the speed of these conventional single-source systems, and restricts the scan rate to only 4-5 revolutions per second [Pelc14; Halliburton12]. Dual-source CT systems increase the temporal resolution by a factor of 2. On the other hand, a real-time tomography system (RTT) [Thompson15; Morton98] consists of a circular array of X-ray sources. These sources can be fired electronically to scan the object without any physical motion of the CT system, which improves the scan rate drastically, and hence, the temporal resolution.
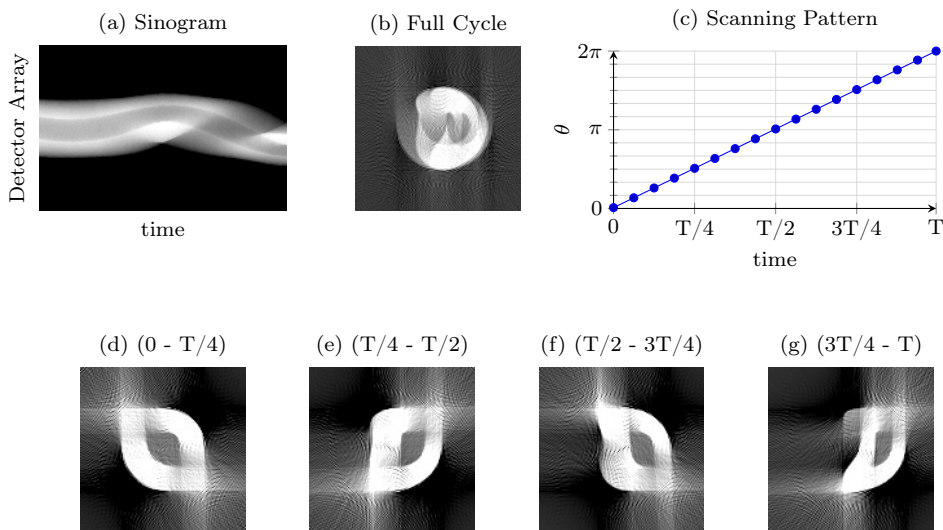
Figure 3.2: Reconstruction of a dynamic phantom using FBP algorithm with data acquired over a full cycle. (a) shows the sinogram, (b) shows the image reconstructed with the data collected over time (0-T) secs, (c) illustrates the scanning pattern over a full cycle, (d) shows the image reconstructed with a part of the data collected over time (0-T/4) sec., and (e)-(g) display reconstructions with chunk of projections collected over their respective time period.

Generally, we acquire projection data over a single half cycle or a single full cycle for the time-invariant tomography, where the object is assumed to be stationary

throughout the data acquisition. This acquisition process may not be suitable for dynamic CT as illustrated in Fig. 3.2. Suppose, the object is deforming, as shown in Fig. 3.1, while taking projections over a single full cycle following the scanning pattern as shown in Fig. 3.2(c). The corresponding sinogram, as shown in Fig. 3.2(a), does not have the sinusoidal features, which usually arise in the sinogram for the time-invariant tomography due to the circular scanning geometry. The motion artifacts are clearly visible in the image, as shown in Fig. 3.2(b), reconstructed with the entire set of projections. The reconstructions with a chunk of projections suffer from limited angle artifacts as shown in Fig. 3.2(d)-(g). These reconstructions motivate the need of special attention on the data acquisition scheme for dynamic CT to improve the spatio-temporal resolution, which we will explain in the next section of this chapter.

The structural changes in the sinogram with time, as shown in Fig. 3.2(a), indicate changes in the deforming object with respect to the source-detector geometry. This implicitly hidden motion information in the Radon space, and local smooth deformations over time in the image space, as shown in Fig. 3.1, motivate modelling of time-dependent changes and incorporate it into an image reconstruction model to enhance the spatio-temporal resolution. The joint motion estimation and image reconstruction approach is called a motion-compensated (MC) approach. The last section of this chapter discusses the state-of-the-art MC reconstruction approaches.

3.1   Sampling Schemes

A data acquisition scheme aims to achieve a high spatio-temporal resolution reconstruction from the Radon data. Therefore, the discussion about the sampling of a Radon space is our primary concern. In this section, we start our discussion with sampling schemes for time-invariant tomography, definition of the spatial and the temporal resolution, and later introduce sampling schemes for dynamic CT and discuss their limitations.

3.1.1   Sampling Schemes for Time-invariant Tomography

The sampling requirements for time-invariant tomography are well studied [Rattey81]. To achieve aliasing free reconstruction from the samples of Radon data, in general, we analyse the two-dimensional Fourier transform $F(\omega_d, \omega_\theta)$ of the Radon transform $p(d, \theta)$. Suppose that the spatial support of the attenuation function $\mu(x, y)$ is limited within a disk of radius R_M and that $\mu(x, y)$ is band-

limited within a disk of radius W_M, as shown in Fig. 3.3. This is an approximation since a function can not be both space and frequency limited. In this case, the spectral support region of $F(\omega_d, \omega_\theta)$ in the $(\omega_d, \omega_\theta)$ plane is a $R_M W_M$-bowtie as shown in Fig. (3.3)(c). Since, the Radon-transform is periodic in θ, its Fourier transform is discrete in ω_θ-direction.
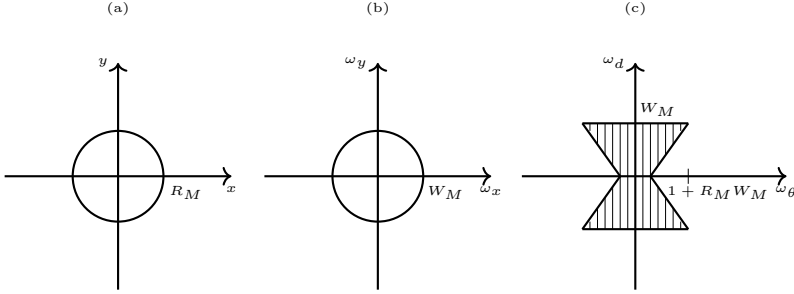
Figure 3.3: (a) and (b) illustrate the spatial and spectral support for the attenuation function. (c) shows the spectral region of the Radon transform, *i.e.*, $R_M W_M$ bowtie.

Following the spectral support region of $F(\omega_d, \omega_\theta)$, Shannon's sampling theorem says that the detector pixel spacing Δd in the $d-$direction must satisfy

$$\Delta d < \frac{\pi}{W_M}. \tag{3.1}$$

Hence, the minimum number of detector pixels should be

$$N_r = \frac{2R_M}{\max \Delta d} = 2R_M \frac{W_M}{\pi}. \tag{3.2}$$

The Fourier transform $F(\omega_d, \omega_\theta)$ is effectively zero for $|\omega_\theta| > |R_M \omega_d| + 1$. Therefore, the maximum bandwidth of the Fourier transform is $2(R_M W_M + 1)$. Hence, according to Shannon's sampling theorem, the angular gap between two consecutive projections should satisfy

$$\Delta \theta < \frac{\pi}{R_M W_M + 1}. \tag{3.3}$$

Therefore, the minimum number of projections uniformly distributed over a half rotation should be

$$M = \frac{\pi}{\max \Delta \theta} = R_M W_M + 1 \approx \frac{\pi}{2} N_r. \tag{3.4}$$

The sampling in Radon space is equivalent to the replica of the band region, *i.e.*, $R_M W_M$-bowtie in the Fourier space. In the above described approach, the

sampling of $p(\theta, d)$ is on a rectangular grid with a gap of Δd in d-direction and $\Delta \theta$ in θ-direction. This sampling approach does not cover the entire frequency space effectively due to the bowtie shape of band region. Whereas, the sampling of Radon space on a hexagonal grid is an optimal sampling scheme, as shown by Rattey and Lindgren in [Rattey81] utilizing the two-dimensional sampling theory.

3.1.2   Spatial Resolution

Spatial resolution refers to the ability of a system to detect the smallest feature of an image. The spatial resolution of a X-ray CT system mainly depends on the spacing between detector pixels, the width of a detector pixel, the number of projections, the reconstruction algorithm, and the gantry rotational speed.

In an industrial CT scanner, the length of a detector array and the spacing between detector pixels are pre-specified by manufactures, which limits the maximum spatial frequency, $i.e. W_M$, observed in a reconstructed image. Further, in the FBP algorithm, shape of the high-pass filter establishes a trade-off between spatial resolution and noise in the reconstructed image. Moreover, the number of projections should be more than the theoretical limit as described in (3.4) for aliasing free reconstruction, which can also limit the achievable spatial resolution. For the iterative reconstruction algorithms, the regularization term establishes a trade-off between spatial resolution and noise, which has been studied by analysing the local impulse response of the system in [Fessler96].

In dynamic CT, the fast gantry speed is one of the most desirable requirements to improve temporal resolution; we describe it in the next section. If the gantry does not stop during the data acquisition and camera aperture is open throughout the acquisition process, the measurement over a detector pixel effectively corresponds to a cone shaped region of an object instead of a simple line-integral along a line. The backprojection of such measurements result in a rotational blur in the reconstruction that degrades spatial resolution of a system.

3.1.3   Temporal Resolution

Temporal resolution refers to the ability of a system to detect the smallest change in the object with respect to time. The temporal resolution mainly depends on the motion of an object, the measurement acquisition scheme, the gantry rotational speed, the reconstruction algorithm, and the detector exposure time. The conventional FBP reconstruction algorithm is still the first choice for

dynamic tomography due to its computational efficiency and the well-developed underlying theoretical understanding. Therefore, we mainly discuss temporal resolution properties considering FBP as a basis for reconstruction algorithm.

A time-sequence of reconstructed image frames demonstrates the object evolution over time in dynamic CT. We need a large number of frames to resolve rapid changes in the object over time. If each frame is reconstructed independently, *i.e.*, without compensating motion information among the frames, the measured projections those are used to reconstruct a frame should satisfy the sampling criteria (3.4). Therefore, the number of projections for each frame should be $N_p \geq M$, uniformly distributed over a half rotation. If the gantry rotation time between two consecutive projections is $T_{\Delta\theta}$, the total time to take one half rotation would be

$$T_r = T_{\Delta\theta} N_p. \tag{3.5}$$

The camera exposure time T_e should be less than $T_{\Delta\theta}$, if the gantry is rotating continuously while acquiring a projection. If T_o is the desired sampling time between two image frames to achieve a high temporal resolution, then

$$\begin{aligned} T_o &\geq T_{\Delta\theta} N_p \\ &> T_e N_p. \end{aligned} \tag{3.6}$$

The inequality (3.6) defines a trade-off between the exposure time and the number of projections to achieve a desirable temporal resolution. The reduction in the number of projections to provide longer exposure time introduces sparse view artifacts in the reconstructed image. On the other hand, the reduction in the exposure time to acquire large number of projections decreases signal-to-noise ratio (SNR) of the acquired measurements. In general, estimation based on low SNR data is highly uncertain. Moreover, as discussed in chapter 2, flat-field estimates based on low-intensity flat-field measurements may introduce severe ring artifacts in the reconstructions. We should also note that the overall signal-to-noise ratio of an reconstructed image depends both on the number of projections and the exposure time[Buzug08], which is described as,

$$\text{SNR} \propto \sqrt{N_p T_e I_0} \tag{3.7}$$

where I_0 is the mean photon count per second and the filtered backprojection is a method of choice for reconstruction.

Motion artifacts become prominent if a data acquisition scheme does not follow inequality (3.6). In order to achieve the desired temporal resolution, if we perform reconstruction only with few projections, the limited angle artifacts appear depending on the distribution of views over a rotation as illustrated through an example in Fig. 3.5. In this example, we assume that the complete experiment

runs for T sec., and desired temporal resolution is $T_o = T/4$ sec. Assuming a fixed camera exposure time, independent of the total number of projections per cycle, we take projections in different configurations, as shown in Fig. 3.4. We observe in Fig. 3.5 that the artifacts are reducing with a higher coverage of projection views over a cycle within the specified temporal resolution of $T/4$ sec.
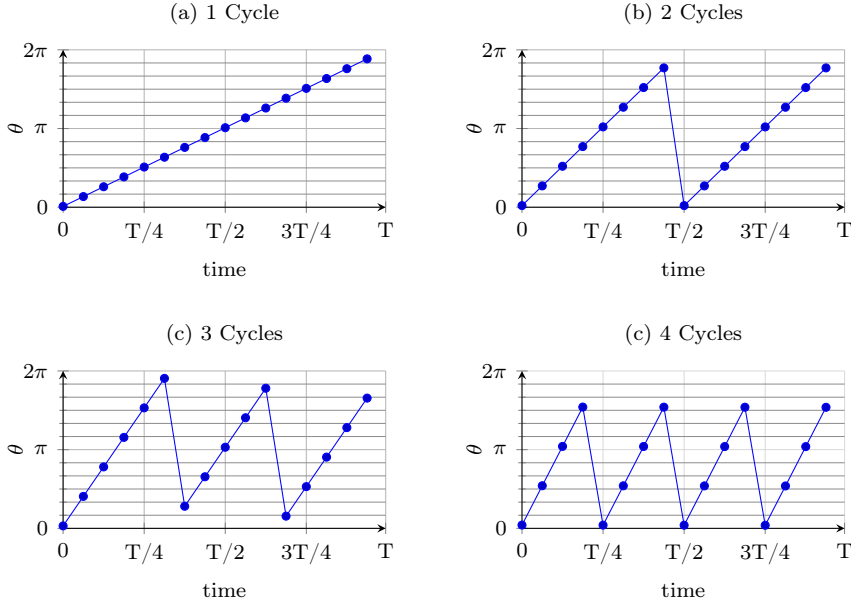
Figure 3.4: Sampling patterns for data acquisitions.

3.1.4   Sampling Schemes for Dynamic CT

We study sampling requirements for dynamic CT by analysing three-dimensional Fourier transform of a time-varying Radon transform $p(d, \theta, t)$. However, this require the knowledge of motion beforehand, which may not be known for real life applications. Willis and Bresler [Willis95] study the sampling of a time-varying Radon transform for an object with a spatially localised and a periodic temporal variation. They assume that the sampling in d-direction satisfies inequality (3.1), which reduces a 3-dimensional sampling problem into a 2-dimensional sampling problem in the (θ, t) plane. They illustrate that the linear sampling on a rectangular grid in the (θ, t) plane does not cover the entire Fourier space effectively. Therefore, they propose a scrambled sampling scheme based on the two-dimensional sampling theory, and achieve reduction in the temporal sam-
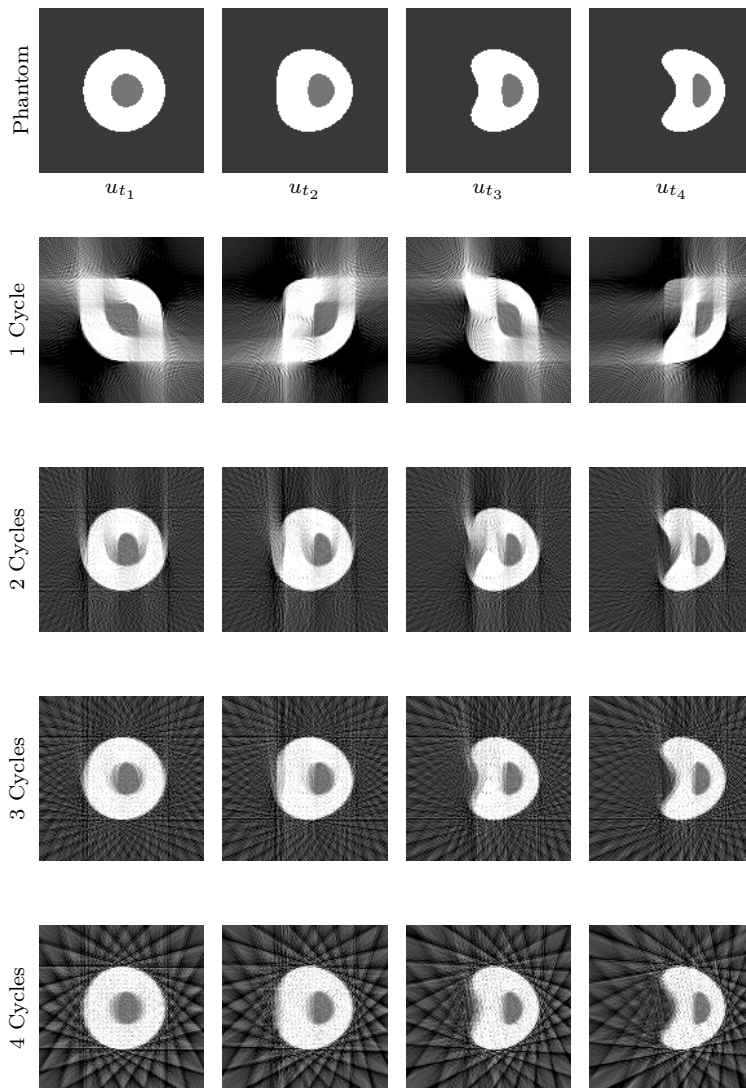
Figure 3.5: Reconstruction of a dynamic phantom using FBP algorithm with data acquired using different sampling patterns illustrated in Fig. 3.4.

pling rate by a factor of four while preserving image quality. Nevertheless, the sampling scheme is very specific to their test case, and it is difficult to see its applicability for a general moving object and especially for an object with

non-periodic temporal variations.

In general, it is difficult to define a sampling scheme without knowing the object motion during the acquisition of measurements. However, we may have a rough idea about the desired temporal and spatial resolution for an application of our interest. Based on this information, we can determine the required gantry speed, number of projections, *etc.*, based on the explanation in previous sections. The motion-compensated (MC) reconstruction approaches exploit information from projection data collected over time to model time-dependent changes in the object. Therefore, the uniqueness of projection data collected over time can prove to be helpful for motion modelling. Keeping this in mind, we will discuss two sampling schemes in the (θ, t) plane. We assumed that the data acquisition is a time sequential process where only one projection can be taken at a time. Moreover, we motivate projections over a full rotation instead of a half rotation for dynamic CT applications, and these projections over a full cycle are used to reconstruct an image frame. Projections over a full cycle allows to reduce a gantry rotation time between the last projection for a frame and the first projection for the subsequent frame of an image sequence.
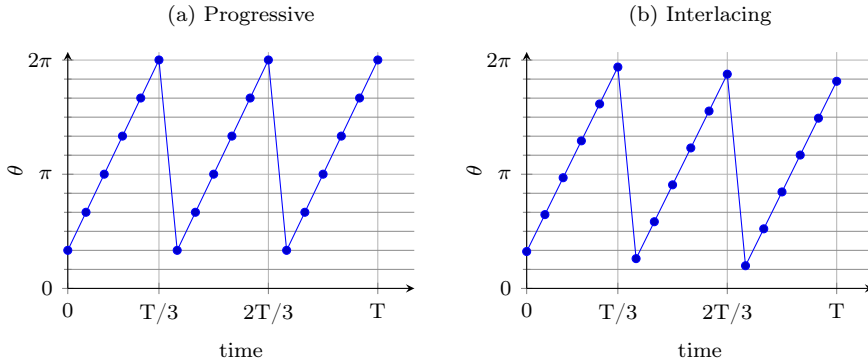
Figure 3.6: A distribution of projection views over time, *i.e.*, the sampling of (θ, t) plane, as per the progressive and the interlaced sampling scheme.

Progressive Sampling:

In this sampling scheme, each frame has the same set of projection angles, *e.g.*, a set of 6 equispaced projections for each frame is same as illustrated in Fig. 3.6(a). This scheme is well suited if each frame is reconstructed independently.

Interlaced Sampling : In this scheme, the projection angles for two consecutive frames are different, but they are interleaved, as shown in Fig. 3.6(b). If an

object is stationary for two consecutive frames, the interlaced sampling scheme provides unique projection data that is not possible in the progressive sampling scheme. In motion-compensated reconstructions, these unique projections provide extra information about the object, which improve the overall quality of a time-sequence of reconstructed images.
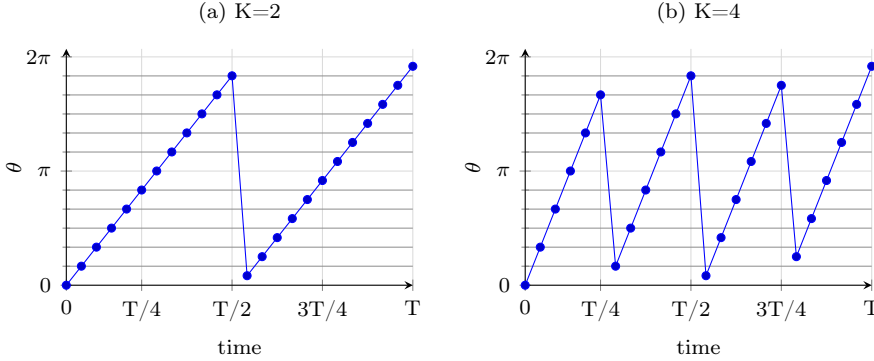
Figure 3.7: Illustration of the bit-reversal based interlacing scheme.

Mohan et. al. [Mohan15] proposed an interlacing scheme based on the bit-reversal permutation as shown in Fig. 3.7. In this scheme, interlaced view angles for the total K image frames is given by

$$\theta_n = \left[nK + B_r \left(\left\lfloor \frac{nK}{N_\theta} \right\rfloor \mathrm{mod} K \right) \right] \frac{2\pi}{N_\theta} \qquad (3.8)$$

where $N_\theta = K N_p$ is the total number of projections acquired during an experiment, and $B_r(a)$ is a bit-reversed function. The authors have also shown the potential of this scheme on real data sets. Nevertheless, this scheme has two major drawbacks :

1. The total number of frames, *i.e.*, K should be a power of 2.

2. This is not a fixed angle scheme. The view angles within a frame are equidistant but the angular gap varies from one frame to another. This could be cumbersome to implement in the real time, depending on the flexibility in a pre-built X-ray CT scanner.

In chapter 6, we are proposing an interlaced sampling scheme based on the family of metallic angles. It is a fixed angle scheme that does not limit the total number of frames to be a power of 2.

3.2   Motion Modelling - Image Registration

Image registration [Modersitzki09] is one of the techniques [Burger17; Hahn17; Manavalan16; Schmitt02] to model time-dependent changes among image sequences. Image registration is a technique to automatically estimate point to point correspondences between images. Mathematically, registration is an ill-posed problem. A variational framework for image registration is given by

$$\underset{y}{\text{minimize}} \ \mathcal{D}(\mathcal{M}(T, f), R) + \alpha \mathcal{S}(f) \tag{3.9}$$

where $f : \mathbb{R}^2 \mapsto \mathbb{R}^2$ is a correspondence map between two-dimensional images $R : \mathbb{R}^2 \mapsto \mathbb{R}$ and $T : \mathbb{R}^2 \mapsto \mathbb{R}$. The data fidelity function $\mathcal{D}$ measures the similarity between a reference image R and a transformed template image $\mathcal{M}(T, f)$ considering image features such as intensity, edges, *etc.* There may be non-unique solutions for the correspondence map, therefore we incorporate prior information about local deformations in the image through a regularizer $\mathcal{S}(f)$ to reduce the solution space. We refer our readers to chapter 5 for a thorough review of similarity measures and regularizers related to image registration models. Fig. 3.8 illustrates image registration of a reference image R with a template image T. In this example, the similarity measure matches the intensity of images such that $R(x) \approx T(f(x))$.

(a) R	(b) T	(c) R & f	(d) T & f grid
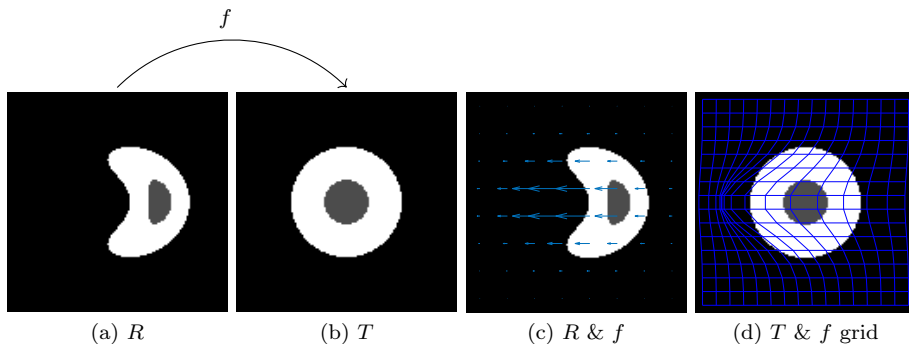
Figure 3.8: Each spatial point in the reference image R has a match in the template image T such that $R(x) \approx T(f(x))$. The map f is illustrated through arrows in Figure (c), which indicates movement of particles from the physical state R to T. Figure (d) illustrates a grid representation of the correspondence map f.

3.3   Reconstruction Models for Dynamic CT

In dynamic CT, sequence of images represent the deformation of an object over time. The spatial and temporal correlation, among image frames, is a very informative prior to regularize the ill-posed dynamic CT reconstruction problem. Here, we give a brief overview of the state-of-the-art iterative reconstruction methods for dynamic CT. We refer readers to [Bonnet03; Rit09; Katsevich10; Laurent12; Hahn14; Manavalan16; Hahn17] for motion-compensated analytical algorithms for dynamic CT. Here, we are extending notations from the previous chapter and introducing a time-dependent system matrix A_t, data b_t, and attenuation function $u_t \in \mathbb{R}^N$ to explain the iterative reconstruction methods.

Guang-Hong *et al.* [Chen08] utilize a prior image u_p reconstructed from the entire dynamic dataset assuming that static regions in the prior image are well reconstructed, however, the dynamic information is lost in the prior image. Therefore, subtraction of the image at time t_k, *i.e.*, u_{t_k} from the prior image removes all static structures, and the substracted image is sparse under some transformation operator. Under these assumptions, they define the reconstruction model as

$$\underset{u_{t_k}}{\text{minimize}} \left[\delta |D(u_{t_k} - u_p)|_1 + (1-\delta)|Du_{t_k}|_1 \right], \quad \text{s.t.} \quad A_{t_k} u_{t_k} = b_{t_k}. \quad (3.10)$$

where D is a discrete derivative operator. This method exploits temporal correlation with respect to a prior image, implicitly assuming small local deformations over time. Abascal *et al.* [Abascal16] enhance the model (3.10) by incorporating a pre-computed motion information between consecutive frames.

In an another approach [Schmitt02; Tian11; Mohan15; Kazantsev15b], they assume that a particle at time t_k moves only in its local neighbourhood over time. Under this assumption, the reconstruction model is defined as

$$\underset{u_{t_1},...,u_{t_K}}{\text{minimize}} \frac{1}{2} \sum_{k=1}^{K} \|A_{t_k} u_{t_k} - b_{t_k}\|^2 + \sum_{k=1}^{K} \sum_{i=1}^{N} \sum_{\{j,l\} \in \mathcal{N}_s} w_{ijkl} \left[(u_{t_k})_i - (u_{t_l})_j \right]^2 \quad (3.11)$$

where N_s defines a neightbourhood set around a point in both spatial and temporal directions. The weight w generally depends on the distance between the point of interest to a point in the neighbourhood set. Kazantsev *et al.* [Kazantsev15b] enhance this approach by using a non-local temporal regularizer and define a neighbourhood set using a prior image acquired from a different imaging modality [Kazantsev15a]. The prior image is also used to enhance edges that remain stationary throughout the acquisition time. Tian *et al.* [Tian11] also use a non-local temporal regularizer, however, regularization is imposed only in consecutive frames. Mory *et al.* [Mory16] enhance the model (3.11) by

performing a temporal regularization along curved trajectories by incorporating a pre-computed motion information in the reconstruction model.

Bernd *et al.* [Messnarz04] propose a spatio-temporal regularization approach for the reconstruction of cardiac transmembrane potential patterns. They assume that the potential pattern has a nondecreasing behaviour over time, which they formulate as a linear constraint on the potential pattern.

Vincent *et al.* [Nieuwenhove17] introduce a motion-vector based iterative technique (MoVIT). In the first step, the MoVIT framework performs pair-wise registration between all time frames reconstructed with a conventional algebraic reconstruction method. Later, they incorporate the estimated motion in the reconstruction framework and utilize informations from neighbouring time frames to achieve a high spatio-temporal resolution.

The above discussed approaches regularize a dynamic CT reconstruction problem either through a pre-computed motion information or by penalizing large movements in the temporal direction. Now, we discuss two joint motion estimation and image reconstruction approaches utilizing image registration techniques.
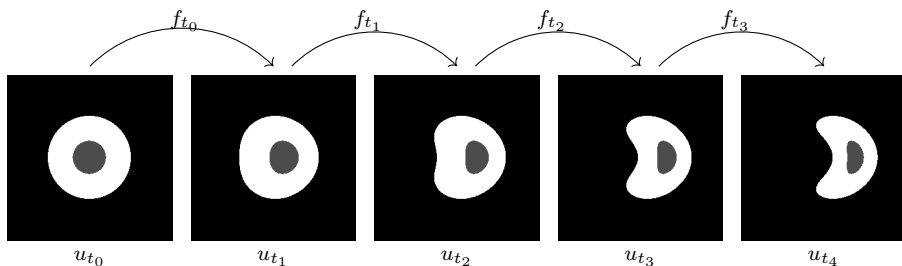
Figure 3.9: Illustration of the sequential motion modelling.

We assume a one-to-one correspondence between the given two image frames. This assumption allows us to track the position of a particle over time indisputably. Instead of tracking particles in all image frames simultaneously, we generally track particles in the nearby two image frames as shown in Fig. 3.9, or we track particles with respect to a fixed reference frame as shown in Fig. 3.10.

Following the modelling approach shown in Fig. 3.9, Mair *et al.* [Mair06] represented the image frame at time t_k approximately in terms of the consecutive image frame $u_{t_{k+1}}$, *i.e.*,

$$u_{t_k}(x) \approx u_{t_{k+1}}(f_{t_k}(x)),$$

and defined the joint motion estimation and image reconstruction model as,

$$\underset{\substack{u_{t_0},\dots,u_{t_{K-1}},\\ f_{t_0},\dots,f_{t_{K-1}}}}{\text{minimize}} \ \frac{1}{2} \sum_{k=0}^{K-1} \|A_{t_k} u_{t_k} - b_{t_k}\|^2 + \frac{\beta}{2} \sum_{k=0}^{K-2} \|u_{t_k} - u_{t_{k+1}}(f_{t_k})\|^2 + \alpha \sum_{k=0}^{K-2} \mathrm{E}(f_{t_k})$$

(3.12)

where $\mathrm{E}(f)$ incorporates the prior information about correspondence map f.
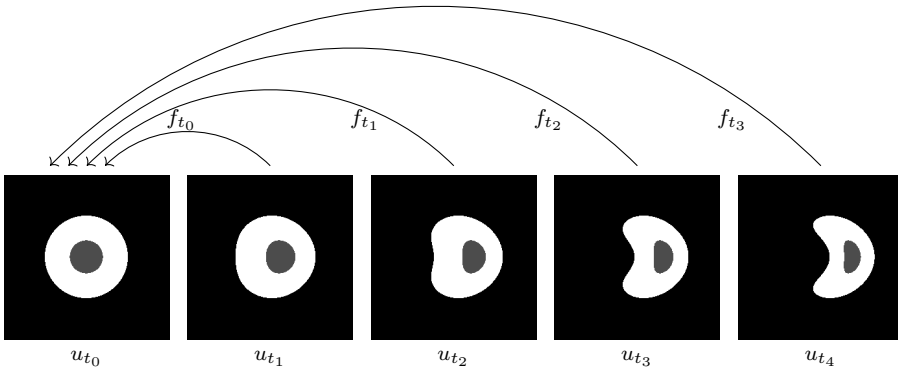
Figure 3.10: Illustration of the reference image based motion modelling.

For a reference frame based motion modelling, an image frame at time t_k is represented in terms of a reference image frame at time t_0, *i.e.*,

$$u_{t_k}(x) = u_{t_0}(f_{t_k}(x)),$$

and the joint motion estimation and image reconstruction model is defined as,

$$\underset{u_{t_0}, f_{t_0},\dots,f_{t_{K-1}}}{\text{minimize}} \ \frac{1}{2} \sum_{k=0}^{K-1} \|A_{t_k} u_{t_0}(f_{t_k}) - b_{t_k}\|^2 + \alpha \sum_{k=0}^{K-1} \mathrm{E}(f_{t_k}).$$

(3.13)

The minimization step with respect to the correspondence map for the model (3.12) is a conventional image registration problem, where data-fidelity is enforced in the image space. However, the model (3.13) measures data-fidelity in the Radon space, and requires an inverse of the correspondence map in the minimization step with respect to the attenuation function, which we generally compute with an iterative method. The model (3.13) reconstructs only one image frame and represents other frames in terms of the computed correspondence maps. However, the model (3.12) reconstructs all image frames as well as correspondence maps.

Assuming that the correspondence map among image frames is known, Su *et al.* [Chun13; Chun12] have shown that the models (3.12) and (3.13) behave similarly as $\beta \to \infty$; and they have studied noise and spatial resolution properties of these reconstruction models.

3.4   Summary

In dynamic CT, we aim to reconstruct a sequence of images that represents a deforming object over time. We desire to achieve a high spatio-temporal resolution, but in practice, it is difficult to detect both rapid changes and smallest features of a deforming object simultaneously. This resolution trade-off is mainly because of the trade-off between the detector acquisition time and the number of projections in the allotted time for an experiment. Moreover, distribution of projection views over time around the object in a CT scanner also plays a role to improve the spatial-temporal resolution. This is important especially for the reconstruction models that exploit motion information from nearby frames. We introduced two state-of-the-art sampling schemes, *i.e.*, progressive and interlacing sampling schemes, and point out their limitations. In the end, we discussed a few state-of-the-art reconstruction models for dynamic CT. These models regularize a dynamic reconstruction problem through a pre-computed motion information, by penalizing large movements in the nearby frames, or by estimating motion along with the unknown object.

A Convex Reconstruction Model for X-ray Tomographic Imaging with Uncertain Flat-fields

The entire content of this chapter has been published in the IEEE journal. The text, tables, and figures in this chapter are the same as it is in the published paper. The published paper has images in the compressed format that hide some of the important information related to our findings. Therefore, we use uncompressed version of these images in this chapter. Please also note that we have reformatted the content of the paper just to align this chapter with rest of the thesis.

Classical methods for X-ray computed tomography are based on the assumption that the X-ray source intensity is known, but in practice, the intensity is measured and hence uncertain. Under normal operating conditions, when the

exposure time is sufficiently high, this kind of uncertainty typically has a negligible effect on the reconstruction quality. However, in time- or dose-limited applications such as dynamic CT, this uncertainty may cause severe and systematic artifacts known as ring artifacts. Existing methods for mitigating ring artifacts have been shown to work reasonably well when applied to measurement data with high or acceptable SNRs. However, we are not aware of any studies that investigate ring artifact correction for low SNR measurements and where the intensity of X-ray beam is assumed to be uncertain. To this end, we derive a new reconstruction model that is based on a rigorous statistical description of our model assumptions. Unlike existing correction methods that, roughly speaking, are based on the geometric nature of ring artifacts in either the sinogram or the reconstruction, our approach is based on a model of a fundamental cause of these artifacts. The resulting reconstruction method jointly estimates the flat-field and the attenuation image, and we show that the estimation problem can be solved efficiently by solving a convex optimization problem. We also derive a quadratic approximation model which is similar to an existing weighted least-squares reconstruction model.

Section 4.1 introduces our model assumptions and reviews some existing approaches to CT reconstruction based on low SNR measurements. We illustrate the sensitivity of these existing methods to flat-field intensity estimation errors. Section 4.2 proposes a new reconstruction model and discusses different parameter selection strategies. We describe our numerical implementation in Section 4.3, and we validate the proposed model based on simulated data as well as real tomographic measurements in Section 4.4. Section 4.5 concludes our findings.

4.1 Conventional Reconstruction Approach

4.1.1 System and Measurement Model

The Lambert–Beer law describes how an X-ray beam is attenuated as it travels through an object that is characterized by a spatial attenuation function $\mu(x)$. Specifically, the incident intensity of an X-ray beam on a detector is given by

$$I \approx I_0 \exp\left(-\int_l \mu(x)\,dx\right) \tag{4.1}$$

where I_0 is the intensity of the X-ray source, and l denotes the line segment between the source and a detector. This description does not take the detector efficiency and the statistical nature of the photon arrival process into account. For photon-counting detectors, it is common to assume that the photon arrival

process is a Poisson process, and each measurement is assumed to be a sample from a Poisson distribution whose mean is prescribed by the Lambert–Beer law. Here we will consider a two-dimensional geometry where p projections are acquired using a one-dimensional detector array with r detector elements. We will use the notation y_{ij} to denote the measurement obtained with detector element i and projection j, and we will assume that the ith detector element has efficiency $\eta_i \in (0, 1]$ such that the effective intensity is $v_i = \eta_i I_0$. Thus, with the assumption that the arrival process is Poisson process, y_{ij} is a realization of a random variable $\mathbf{y}_{ij}$ which, conditioned on μ and v_i, is a Poisson random variable whose mean is prescribed by the Lambert–Beer law, *i.e.*,

$$\mathbf{y}_{ij} \mid \mu, v_i \sim \text{Poisson}\left(v_i \exp\left(-\int_{l_{ij}} \mu(x)\, dx\right)\right) \tag{4.2}$$

where l_{ij} notes the line segment between the ith detector element and the source for projection angle j. For ease of notation, we define a matrix random variable $\mathbf{Y}$ of size $r \times p$ with elements $\mathbf{y}_{ij}$, and similarly, the $r \times p$ matrix Y denotes a realization of $\mathbf{Y}$ and $y = \text{vec}(Y)$.

The attenuation function $\mu(x)$ may be discretized by using a parameterization

$$\mu(x) = \sum_{k=1}^{n} u_k \mu_k(x) \tag{4.3}$$

where $\mu_k(x)$ is one of n basis functions (*e.g.*, a pixel or voxel basis), and $u \in \mathbb{R}^n$ is a vector of unknowns (*e.g.*, pixel or voxel values). With this parameterization, the line integrals in (4.2) can be expressed as

$$\int_{l_{ij}} \mu(x)\, dx = e_i^T A_j u$$

where the elements of the matrix $A_j \in \mathbb{R}^{r \times n}$ are given by

$$(A_j)_{ik} = \int_{l_{ij}} \mu_k(x)\, dx,$$

and hence the columns of $\mathbf{Y}$ satisfy

$$\mathsf{E}[\mathbf{y}_j|u, v] = \text{diag}(v)\exp(-A_j u), \ j = 1, \ldots, p$$

where $v = (v_1, \ldots, v_r)$.

In practice, the vector v is unknown and must be measured. As mentioned in the introduction, the measurements of v are often referred to as flat-field measurements and are simply measurements obtained without any object in the

CT scanner. We will assume that s flat-field measurements are acquired for each detector element based on the flat-field measuring model

$$\mathbf{f}_{ij} \mid v_i \sim \text{Poisson}\,(v_i) \tag{4.4}$$

for $i = 1, \ldots, r$ and $j = 1, \ldots, s$, and $\mathbf{F}$ denotes a $r \times s$ matrix random variable with elements $\mathbf{f}_{ij}$. As for the measurements Y, the matrix $F \in \mathbb{R}^{r \times s}$ denotes a realization of $\mathbf{F}$.

4.1.2 Maximum Likelihood Estimation

Given the flat-field measurements F, a maximum likelihood (ML) estimate of v is given by

$$\hat{v}_{\text{f}} = \operatorname*{argmin}_{v} \left\{ -\log \mathrm{P}(F \mid v) \right\} \tag{4.5}$$

$$= \operatorname*{argmin}_{v} \left\{ s\mathbf{1}^T v - \mathbf{1}^T F^T \log(v) \right\} = \frac{1}{s} F\mathbf{1},$$

i.e., $\hat{v}_{\text{f}}$ is simply the arithmetic average of the s flat-field measurements. This estimate can be used to compute an *approximate* ML estimate of the vector u which is given by

$$\hat{u}_{\text{y}} = \operatorname*{argmin}_{u} \left\{ -\log \mathrm{P}(Y \mid u, \hat{v}_{\text{f}}) \right\} \tag{4.6}$$

$$= \operatorname*{argmin}_{u} \left\{ (\mathbf{1} \otimes \hat{v}_{\text{f}})^T \exp(-Au) + y^T Au \right\}$$

where $A \in \mathbb{R}^{rp \times n}$ is defined as $A = [A_1^T \;\; \cdots \;\; A_p^T]^T$. The estimation problem (4.6) is a convex optimization problem, and it is essentially an approximate ML estimation problem since with our model assumptions, the true likelihood $\mathrm{P}(Y \mid u, v)$ is a function of both u and v. We will return to this issue in the next section.

If y is positive, a quadratic approximation of (4.6) can be obtained by means of a second-order Taylor expansion of the likelihood function [Sauer93], and this yields the following weighted least-squares objective function

$$\frac{1}{2} \| \text{diag}(y)^{1/2} (Au - b) \|_2^2 \tag{4.7}$$

where $b = \mathbf{1} \otimes \log(\hat{v}_{\text{f}}) - \log(y)$. Notice that if A has full rank and $rp \leq n$, both (4.6) and the quadratic approximation (4.7) reduce to the problem of solving the consistent system of equations $Au = b$, but the two problems are generally different when the system of equations $Au = b$ is inconsistent. The noise properties of reconstructions based on the weighted least-squares objective (4.7) have been studied in [Rose15].

4.1.3   The Effect of Flat-field Estimation Errors

The flat-field estimate $\hat{v}_\text{f}$ in (4.5) satisfies $\mathsf{E}[\hat{v}_\text{f}] = v$, and hence it is an unbiased estimate. However, $\hat{v}_\text{f}$ is itself a random variable with covariance $(1/s)\text{diag}(v)$, and the flat-field estimation error may lead to artifacts in the reconstruction. To study how flat-field estimation errors influence the reconstruction, we now consider a simplified model based on Gaussian approximations. Specifically, we assume that $(\hat{v}_\text{f})_i | v_i \sim \mathcal{N}(v_i, s^{-1}v_i)$ and $\mathbf{y}_{ij}|v_i, u \sim \mathcal{N}(v_i \exp(-e_i^T A_j u), v_i \exp(-e_i^T A_j u))$. With these assumptions, $\mathbf{b}_{ij} = \log((\hat{v}_\text{f})_i) - \log(\mathbf{y}_{ij})$ can be approximated by linearizing each of the log terms around the mean of their arguments, *i.e.*,

$$\mathbf{b}_{ij} \approx \log(v_i) + \frac{(\hat{v}_\text{f})_i - v_i}{v_i} - \log(\mathsf{E}[\mathbf{y}_{ij}]) - \frac{\mathbf{y}_{ij} - \mathsf{E}[\mathbf{y}_{ij}]}{\mathsf{E}[\mathbf{y}_{ij}]}$$

$$= e_i^T A_j u + \mathbf{z}_i + \mathbf{w}_{ij}$$

for $i = 1, \ldots, r$ and $j = 1, \ldots, p$, and where

$$\mathbf{z}_i = ((\hat{v}_\text{f})_i - v_i)/v_i, \ \mathbf{z}_i \sim \mathcal{N}(0, (sv_i)^{-1})$$

and

$$\mathbf{w}_{ij} = (\mathbf{y}_{ij} - \mathsf{E}[\mathbf{y}_{ij}])/\mathsf{E}[\mathbf{y}_{ij}], \ \mathbf{w}_{ij} \sim \mathcal{N}(0, v_i^{-1} \exp(e_i^T A_j u)).$$

The terms $\mathbf{z}_i$ arise because of the flat-field estimation errors, and the terms $\mathbf{w}_{ij}$ represent the effect of measurement noise. If we define $\mathbf{z} = (\mathbf{z}_1, \ldots, \mathbf{z}_r)$ and $\mathbf{w} = \text{vec}(\mathbf{W})$ where $\mathbf{W}$ is the $r \times p$ matrix with elements $\mathbf{w}_{ij}$, then

$$\mathbf{b} \approx Au + \mathbf{1} \otimes \mathbf{z} + \mathbf{w}. \tag{4.8}$$

Not surprisingly, this shows that flat-field estimation errors affect all projections, and hence give rise to structured errors.

The linear approximation reaffirms that the variance of the flat-field errors is inversely proportional to the flat-field intensity and the number of flat-field measurements s. Thus, if s is sufficiently large, the flat-field estimation errors play a negligible role. However, a twofold reduction of the flat-field error-to-noise ratio

$$\sqrt{\frac{\mathsf{E}[\mathbf{z}_i^2]}{\mathsf{E}[\mathbf{w}_{ij}^2]}} = \frac{1}{\sqrt{s \exp(-e_i^T A_j u)}}$$

requires a fourfold increase in the number of flat-field samples, and hence it may require many samples to obtain a sufficiently small flat-field error-to-noise ratio.

We now demonstrate the effect of flat-field estimation errors by considering the behavior of reconstructions based on (4.6). We will use a constant flat-field $v = \omega \mathbf{1}$ for $\omega > 0$ to generate a set of measurements according to the model (4.2)

with $r = 200$ detector elements and $p = 720$ parallel beam projections covering a full rotation. For the reconstruction we use the flat-field ML estimate $\hat{v}_{\mathrm{f}}$, as defined in (4.5), where only one flat-field sample ($s = 1$) is acquired for each detector element based on (4.4).

Our object u, shown in Fig. 4.1a, consists of three squares of different sizes where the attenuation of the innermost square is 0.5 cm^{-1}, the enclosing square has attenuation 0.25 cm^{-1}, and the outermost square has no attenuation. The domain size is 1 cm, and the reconstruction grid is 128×128 pixels. Fig. 4.1 shows three reconstructions based on (4.6) with different values of the parameter ω. The effect of the flat-field error appears as a ring in the reconstructions, and it is clear that the severity of both noise and the ring in the reconstruction decreases as the flat-field intensity is increased. In the next section, we propose and investigate a new reconstruction model that takes a statistical model of the flat-field into account.

The effect of a flat-field estimation error on the reconstruction may also be analyzed by means of an analytic reconstruction of the sinogram $h_\theta(t) = \delta(t - t_0)$ where $t_0 \neq 0$ is a given constant. This corresponds to a "line" in the sinogram. The function $h_\theta(t)$ is a radial function (*i.e.*, it does not depend on θ), but it is not the Radon transform of a function since $h_\theta(t) \neq h_{\theta+\pi}(-t)$. As a consequence, the Fourier slice theorem does not hold. However, we may still compute a reconstruction using filtered backprojection. The reconstruction $\mu(x)$ is itself a radial function, and if we let $x = \rho n_\phi$ where $n_\phi = (\cos \phi, \sin \phi)$ such that $|\rho|$ is the distance to the origin, we obtain the expression [Kak01]

$$\mu(\rho n_\phi) = \frac{1}{2} \int_{-\pi}^{\pi} \int_{-\infty}^{\infty} H_\theta(\zeta) |\zeta| e^{-2\pi\epsilon|\zeta|} e^{i2\pi\zeta\rho n_\phi^T n_\theta} \, d\zeta \, d\theta$$

$$= \pi \int_{-\infty}^{\infty} H_\theta(\zeta) |\zeta| e^{-2\pi\epsilon|\zeta|} J_0(2\pi\zeta\rho) \, d\zeta$$

$$= \pi \int_0^{\infty} \left[H_\theta(\zeta) + H_\theta(-\zeta) \right] e^{-2\pi\epsilon\zeta} \zeta J_0(2\pi\zeta\rho) \, d\zeta$$

where J_0 denotes the zeroth-order Bessel function of the first kind, $H_\theta(\zeta) = e^{-i2\pi\zeta t_0}$ is the Fourier transform of $h_\theta(t)$, and $|\zeta| e^{-2\pi\epsilon|\zeta|}$ is an apodizing filter with parameter $\epsilon > 0$. Using the Hankel transform pair (20) in [Bateman54, p. 9], we obtain the closed-form expression

$$\tilde{\mu}(\rho) = \frac{1}{4\pi} \left(\frac{\sigma}{(\sigma^2 + \rho^2)^{3/2}} + \frac{\bar{\sigma}}{(\bar{\sigma}^2 + \rho^2)^{3/2}} \right) \tag{4.9}$$

where $\sigma = \epsilon + it_0$ and $\tilde{\mu}(\rho) = \mu(\rho n_\phi)$. Fig. 4.2 shows three examples of what this function may look like. It is clear from the figure that a systematic error in the sinogram in the form of a "line" will appear as spikes in the radial reconstruction.

(a) Phantom

(b) $\omega = 10^3$ photons

(c) $\omega = 10^4$ photons

(d) $\omega = 10^5$ photons
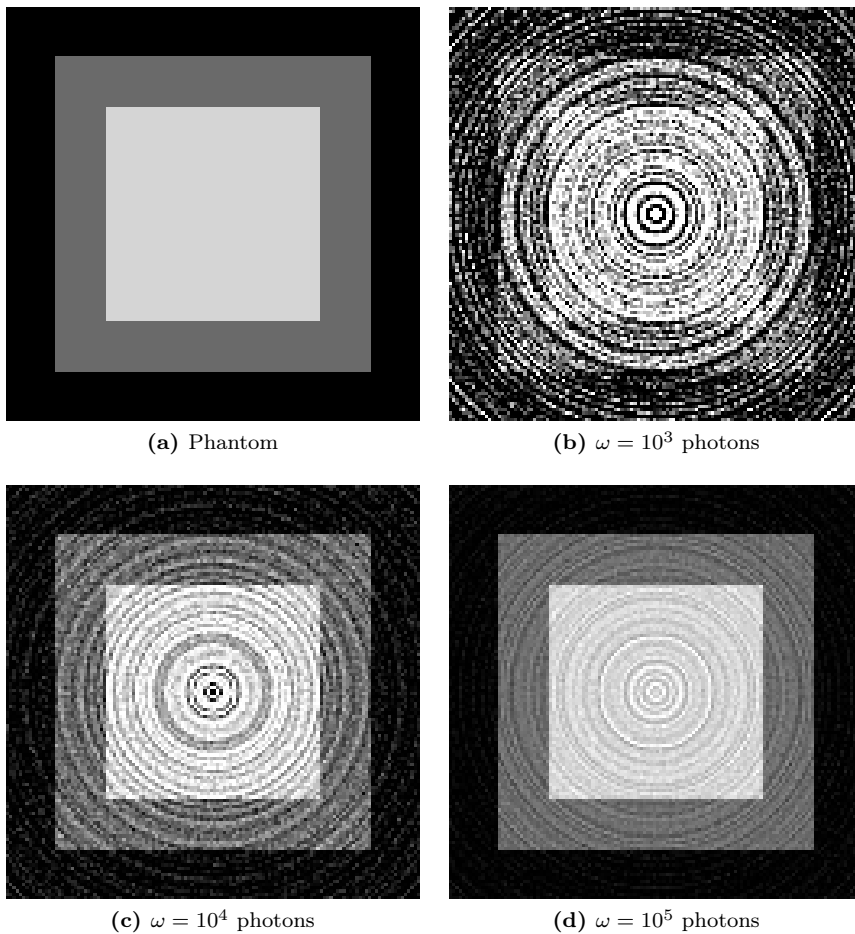
Figure 4.1: Phantom (a) and reconstructions (b), (c), and (d), based on (4.6) with flat-field estimation errors. The display range for each of the images is $[0, 0.6]$.
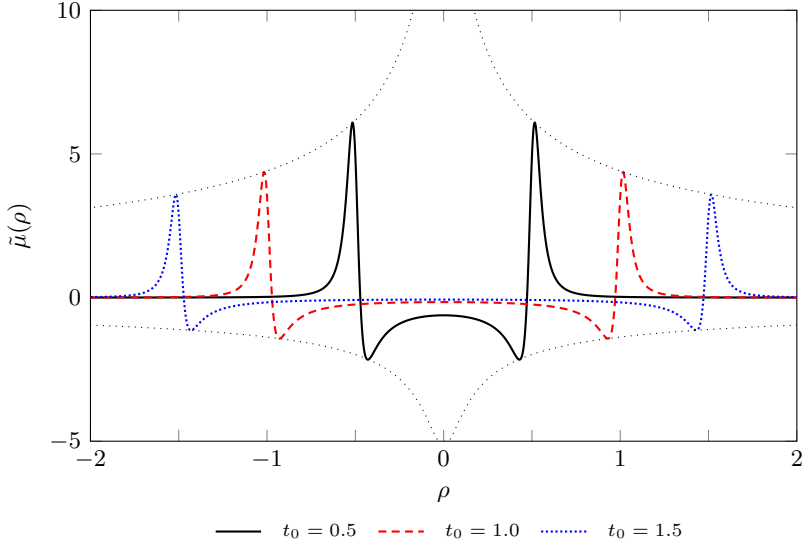
Figure 4.2: Examples of radial profile of reconstruction of $h_\theta(t)$ for three different values of t_0 (0.5, 1.0, and 1.5) and $\epsilon = 0.05$.

In particular, the reconstruction will have two "rings" of opposite sign near $\rho = t_0$, corresponding to the positive and negative peaks in the profile $\tilde{\mu}(\rho)$. The extrema of $\tilde{\mu}(\rho)$ (*i.e.*, the spike magnitudes) depend on both t_0 and ϵ. The dotted curves in the figure provide an envelope of the extrema for $\epsilon = 0.05$, and it shows that the magnitude of a spike is large when $|t_0|$ is small and vice versa. Our analysis of the extrema of $\tilde{\mu}(\rho)$, which is included in Appendix 4.A, shows that they are approximately inversely proportional to $\sqrt{\epsilon^3 |t_0|}$ when $|t_0| \gg \epsilon$. Moreover, $\tilde{\mu}(\rho)$ may have a significant offset near $\rho = 0$, as is the case for the example with $t_0 = 0.5$ in Fig. 4.2.

4.1.4 Including Prior Information

If the prior probability density $\mathrm{P}(u)$ is assumed to be known, a so-called maximum a posteriori (MAP) estimate can be expressed as

$$\hat{u}_{\mathrm{map}} = \operatorname*{argmin}_{u} \left\{ -\log \mathrm{P}(u \mid y, v) \right\} \tag{4.10}$$

where, according to Bayes' rule, the posterior probability density $\mathrm{P}(u|y, v)$ satisfies

$$\mathrm{P}(u \mid y, v) \propto \mathrm{P}(y \mid u, v)\mathrm{P}(u). \tag{4.11}$$

Again, since v is generally unknown, an approximate MAP (AMAP) estimate can be obtained by maximizing an approximation of the posterior distribution, *i.e.*,

$$\hat{u}_{\text{amap}} = \underset{u}{\text{argmin}} \left\{ -\log P(u \mid y, \hat{v}_{\text{f}}) \right\}. \tag{4.12}$$

We will restrict our attention to priors of the form

$$P(u \mid \gamma) \propto e^{-\gamma \phi(u)} \tag{4.13}$$

where $\phi(u)$ is a convex function and $\gamma > 0$ is a hyperparameter. With this prior, the AMAP estimation problem can be expressed as

$$\hat{u}_{\text{amap}} = \underset{u}{\text{argmin}} \left\{ (\mathbf{1} \otimes \hat{v}_{\text{f}})^T \exp(-Au) + y^T Au + \gamma \phi(u) \right\} \tag{4.14}$$

which is a convex optimization problem. Alternatively, using the quadratic approximation (4.7) in place of the log-likelihood function, we obtain the regularized weighted least-squares problem

$$\hat{u}_{\text{wls}} = \underset{u}{\text{argmin}} \left\{ \frac{1}{2} \|\text{diag}(y)^{1/2}(Au - b)\|_2^2 + \gamma \phi(u) \right\} \tag{4.15}$$

as an approximation to the AMAP estimation problem.

4.2   Joint Reconstruction Approach

We now turn to the main contribution of this paper, namely a model for jointly estimating the flat-field v as well as the absorption image u. Recall from the example in section 4.1.3 that the approximate ML model (4.6) may lead to ring artifacts. As will be evident from our numerical experiments in section 4.4, the approximate MAP model (4.14) suffers the same drawback. To mitigate this, we consider joint MAP estimation of u and v. This approach is motivated by the fact that the measurements Y contain information about both u and v. Indeed, given u, an ML estimate of v can be computed as

$$\hat{v}_{\text{y}}(u) = \underset{v}{\text{argmin}} \left\{ -\log P(Y \mid u, v) \right\} \tag{4.16}$$

$$= \text{diag}\left(\sum_{j=1}^{p} \exp(-A_j u) \right)^{-1} Y\mathbf{1}. \tag{4.17}$$

4.2.1   MAP Estimation Problem

With the model assumptions described in 4.1.1 and given a flat-field prior $P(v|\alpha, \beta)$, the joint posterior distribution of the unknown parameters u and v can be expressed as

$$P(u, v \mid Y, F) \propto P(Y, F \mid u, v) P(u \mid \gamma) P(v \mid \alpha, \beta)$$

where $P(Y, F|u, v) = P(Y|u, v) P(F|v)$, and $\alpha \in \mathbb{R}^r$ and $\beta \in \mathbb{R}^r$ are hyperparameters associated with the flat-field prior. Here we will assume that v_i and v_j, $i \neq j$ are independent, and the flat-field prior is $v_i | \alpha_i, \beta_i \sim \text{Gamma}(\alpha_i, \beta_i)$ for $i = 1, \dots, r$, *i.e.*,

$$P(v_i \mid \alpha_i, \beta_i) = \frac{\beta_i^{\alpha_i}}{\Gamma(\alpha_i)} v_i^{\alpha_i - 1} \exp(-\beta_i v_i).$$

The Gamma prior is chosen because of computational convenience; it is the so-called conjugate prior for the Poisson likelihood function, and as a consequence, the posterior distribution of v given u is itself a Gamma distribution. For the Gamma distribution, the hyperparameter α_i is commonly referred to as the shape, and β_i is referred to as the rate. The corresponding MAP estimation problem can be expressed as

$$
\begin{aligned}
(\hat{u}, \hat{v}) &= \underset{(u,v)}{\arg\min} \left\{ -\log P(u, v \mid Y, F) \right\} \qquad (4.18) \\
&= \underset{(u,v)}{\arg\min} \left\{ J(u, v) + \gamma \phi(u) \right\}
\end{aligned}
$$

where

$$J(u, v) = v^T d(u) + y^T A u - c^T \log(v) \qquad (4.19)$$

and

$$c = F\mathbf{1} + Y\mathbf{1} + \alpha - \mathbf{1}, \ \ d(u) = s\mathbf{1} + \sum_{j=1}^{p} \exp(-A_j u) + \beta. \qquad (4.20)$$

The function $J(u, v)$ is convex in u given v and vice versa, but it is not jointly convex in u and v. However, by setting the gradient of $J(u, v)$ with respect to v equal to zero, we obtain the first-order optimality condition $\hat{v}(u) = \text{diag}(d(u))^{-1} c$. This allows us to eliminate v from the estimation problem (4.18), *i.e.*,

$$J(u, \hat{v}(u)) \propto y^T A u + c^T \log(d(u)),$$

which is a convex function of u. Thus, the problem (4.18) is equivalent to the following convex reconstruction model

$$\hat{u} = \underset{u}{\arg\min} \left\{ y^T A u + c^T \log(d(u)) + \gamma \phi(u) \right\} \qquad (4.21)$$

with the flat-field estimate $\hat{v}$ given by

$$\hat{v} = \text{diag}(d(\hat{u}))^{-1}c. \tag{4.22}$$

We note that $\hat{v}$ has an interesting interpretation: each element of $\hat{v}$ can be expressed as a convex combination of three independent estimates, *i.e.*,

$$\hat{v} = \text{diag}(\theta_1)\hat{v}_{\text{f}} + \text{diag}(\theta_2)\hat{v}_{\text{y}}(\hat{u}) + \text{diag}(\theta_3)\hat{v}_{\text{pr}}(\alpha, \beta) \tag{4.23}$$

where $\theta_1, \theta_2, \theta_3 \in \mathbb{R}_+^r$, $\theta_1 + \theta_2 + \theta_3 = \mathbf{1}$, are parameters that depend on both data and $\hat{u}$, α, and β. The ML estimate $\hat{v}_{\text{f}}$, defined in (4.5), is based on the flat-field measurements F, the estimate $\hat{v}_{\text{y}}(\hat{u})$ is based on the measurements Y and defined in (4.16), and the estimate $\hat{v}_{\text{pr}}(\alpha, \beta) = \text{diag}(\beta)^{-1}(\alpha - \mathbf{1})$ is based on the flat-field prior; see Appendix 4.B for further details on this interpretation.

4.2.2   Choosing The Hyperparameters

The estimation problem (4.21) depends on the flat-field hyperparameters α and β. We now discuss different ways to choose these hyperparameters.

4.2.2.1   Uniform Positive Prior

The simplest prior is perhaps the uniform positive (UP) prior which is obtained by setting $\alpha_i = 1$ and $\beta_i = 0$ for $i = 1, \ldots, r$. In the present case, this corresponds to simply omitting the prior $\text{P}(v|\alpha, \beta)$ from the model, and hence the flat-field estimates $\hat{v}(u)$ become convex combinations of only two estimates instead of three. This is an improper prior since it does not integrate to one.

4.2.2.2   Jeffreys Prior

The Jeffreys prior (JP) for the Poisson distribution is $p(v_i|\alpha_i, \beta_i) \propto 1/\sqrt{v_i}$ which is obtained by letting $\alpha_i = 0.5$ and $\beta_i = 0$. This is also an improper prior.

4.2.2.3   Type-II ML Estimation

The flat-field measurements can be used to estimate the hyperparameters by maximizing the marginal probability of $f_{i1}, \ldots, f_{is}$ given the hyperparameters

α_i and β_i, *i.e.*,

$$(\hat{\alpha}_i, \hat{\beta}_i) = \underset{(\alpha_i, \beta_i)}{\operatorname{argmin}} \left\{ -\log \mathrm{P}(f_{i1}, \ldots, f_{is} \mid \alpha_i, \beta_i) \right\}. \tag{4.24}$$

This is known as type-II ML estimation or empirical Bayes estimation [Berger85]. As shown in Appendix 4.C, this approach leads to the AMAP model, *i.e.*, a zero-variance prior with mean $\hat{v}_{\mathrm{f}}$.

4.2.2.4   Flat-field Emphasizing Prior

Recall that the flat-field estimate $\hat{v}(u)$ can be expressed as convex combinations of three estimates. Specifically,

$$\hat{v}_i(u) = \frac{s}{d_i(u)}(\hat{v}_{\mathrm{f}})_i + \frac{\tau_i(u)}{d_i(u)}(\hat{v}_{\mathrm{y}})_i + \frac{\beta_i}{d_i(u)}\frac{\alpha_i - 1}{\beta_i} \tag{4.25}$$

where $\tau_i(u) = \sum_{j=1}^{p} \exp(-e_i^T A_j u)$. If we set the mode of the Gamma prior (*i.e.*, $(\alpha_i - 1)/\beta_i$) equal to the flat-field ML estimate $(\hat{v}_{\mathrm{f}})_i$ by letting $\alpha_i = 1 + \beta_i(\hat{v}_{\mathrm{f}})_i$, we obtain the estimate

$$\hat{v}_i(u) = \frac{s + \beta_i}{d_i(u)}(\hat{v}_{\mathrm{f}})_i + \frac{\tau_i(u)}{d_i(u)}(\hat{v}_{\mathrm{y}})_i \tag{4.26}$$

which is a convex combination of two estimates. It is easy to verify that $\hat{v}_i(u) \to (\hat{v}_{\mathrm{f}})_i$ as $\beta \to \infty$, and with $\beta_i = 0$, the estimate $\hat{v}_i(u)$ is equivalent to the estimate obtained with the UP prior. Thus, choosing $\beta_i > 0$ and $\alpha_i = 1 + \beta_i(\hat{v}_{\mathrm{f}})_i$ allows us to emphasize the flat-field ML estimate $(\hat{v}_{\mathrm{f}})_i$. This is consistent with the fact that the parameter β_i is the rate parameter associated with the Gamma distribution: the larger the rate, the more concentrated the distibution is around its mode. This is illustrated in Fig. 4.3. We call this corresponding prior the flat-field emphasizing (FE) prior.

4.2.3   Quadratic Approximation

A quadratic approximation of the first two terms in (4.21) can be derived by means of a second-order Taylor expansion with respect to Au. Substituting y for $(I \otimes \operatorname{diag}(\hat{v}(u))) \exp(-Au)$, we obtain the following approximate MAP estimation problem

$$\hat{u}_{\mathrm{swls}} = \underset{u}{\operatorname{argmin}} \left\{ \frac{1}{2} \|Au - b\|_{\hat{\Sigma}_{\mathrm{b}}^{-1}}^2 + \gamma \phi(u) \right\} \tag{4.27}$$
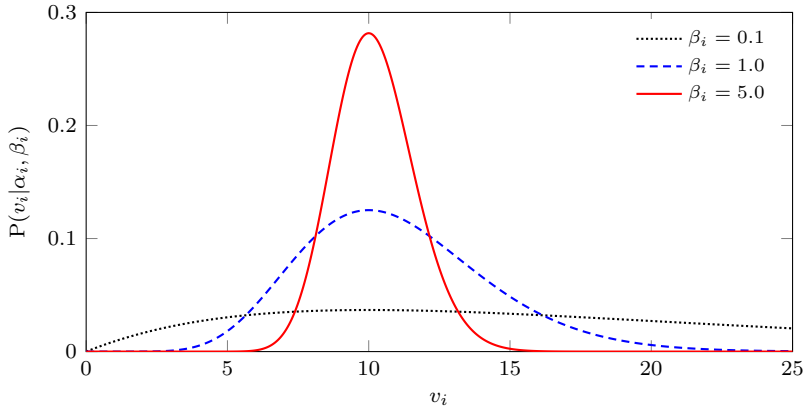
Figure 4.3: Gamma distributions with hyperparameters β_i and $\alpha_i = 1 + (\hat{v}_\mathrm{f})_i \beta_i$ for $(\hat{v}_\mathrm{f})_i = 10$ and $\beta_i \in \{0.1, 1.0, 5.0\}$.

where the covariance matrix $\widehat{\Sigma}_\mathbf{b}$ is defined as

$$\widehat{\Sigma}_\mathbf{b} = (\mathbf{1}\mathbf{1}^T) \otimes \mathrm{diag}(s\hat{v}_\mathrm{f} + \alpha - 1)^{-1} + \mathrm{diag}(y)^{-1}. \tag{4.28}$$

This is also the covariance matrix associated with $\mathbf{b}$ in the linear approximation (4.8). Note that the weighted least-squares data fidelity term takes the systematic errors induced by flat-field estimation errors into account without explicitly modeling the flat-field, and hence we label this a regularized stripe-weighted least-squares (SWLS) problem. The model depends on the hyperparameter vector α, which appears in the covariance matrix, but β does not appear in the model.

4.3 Implementation

The MAP estimation problems (4.14) and (4.21) as well as the WLS (4.15) and SWLS (4.27) quadratic approximations are all convex problems that can be solved with a wide range of numerical optimization methods. Here we will focus on simple first-order methods which are suitable for large-scale problems.

4.3.1 Attenuation Priors

Before we describe our implementation of the different reconstruction methods, we briefly discuss two attenuation priors of the form (4.13), namely the

nonnegativity prior (corresponding to nonnegativity constraints $u_i \geq 0$), and a combination of the nonnegativity prior and total variation (TV) regularization [Rudin92]. Both of these priors can be combined with the existing AMAP model (4.14), the proposed model (4.21), the WLS model (4.15) and the SWLS model (4.27).

4.3.1.1 Nonnegativity

The nonnegativity constraints can be expressed as $\phi(u) = I_+(u)$ where $I_+(u)$ denotes the indicator function of the nonnegative orthant, *i.e.*, $I_+(u) = 0$ if and only if u is a nonnegative vector, and otherwise $I_+(u) = \infty$.

4.3.1.2 Nonnegativity and TV

The combination of nonnegativity constraints and TV may be expressed as

$$\phi(u) = I_+(u) + \mathrm{TV}_\delta(u)$$

where $\mathrm{TV}_\delta(u) = \sum_{i=1}^n \xi_\delta(\|D_i u\|_2)$ is a differentiable TV-approximation, ξ_δ denotes the Huber-norm

$$\xi_\delta(t) = \begin{cases} (t)^2/(2\delta) & |t| \leq \delta \\ |t| - \delta/2 & \text{otherwise} \end{cases}$$

with parameter δ, and $D_i u$ is a finite-difference approximation of the gradient at pixel i. We will use a pixel basis corresponding to an $M \times N$ grid (*i.e.*, $n = MN$). Specifically, we define

$$D_i = \begin{bmatrix} e_i^T(I_N \otimes \bar{D}_M) \\ e_i^T(\bar{D}_N \otimes I_M) \end{bmatrix}$$

where I_M and I_N are identity matrices, and $\bar{D}_M$ and $\bar{D}_N$ are square difference matrices of order M and N, respectively, and of the form

$$\begin{bmatrix} 1 & -1 & & \\ & \ddots & \ddots & \\ & & 1 & -1 \\ & & & 0 \end{bmatrix}$$

where the last row is zero, corresponding to Neumann boundary conditions.

The function $\mathrm{TV}_\delta(u)$ has a Lipschitz continuous gradient with constant $L_{\mathrm{tv}}(\delta) = \|D\|_2^2/\delta$ where $D = \begin{bmatrix} D_1^T & \cdots D_n^T \end{bmatrix}^T$.

4.3.2   Reconstruction Models

We now consider five different reconstruction models of the form

$$\text{minimize} \quad J_i(u) + \gamma\phi(u), \quad i = 1, \ldots, 5, \tag{4.29}$$

where $J_i(u)$ is based on either (4.10), (4.14), (4.21), (4.15) or (4.27).

4.3.2.1   Baseline and AMAP Estimation

The reconstruction model (4.10) requires the true flat-field v which is not available in practice. However, the model may be used to compute a baseline reconstruction in simulation studies. The baseline reconstruction problem corresponds to $J_1(u) = J(u, v)$ where the true flat-field v is assumed to be known. If we replace v by $\hat{v}_{\mathrm{f}}$, we obtain the AMAP model (4.14) with objective $J_2(u) = J(u, \hat{v}_{\mathrm{f}})$.

To solve the reconstruction problem (4.29) using a first-order method, we need the gradient of $J(u, v)$ with respect to u, *i.e.*,

$$\nabla_u J(u, v) = A^T(y - \hat{y}(u, v)) \tag{4.30}$$

where $\hat{y}(u, v) = (I \otimes \mathrm{diag}(v))\exp(-Au)$. It is easy to verify that the gradient $\nabla_u J(u, v)$ is Lipschitz continuous on the nonnegative orthant since the norm of the Hessian

$$\nabla_u^2 J(u, v) = A^T \mathrm{diag}(\hat{y}(u, v))A$$

is bounded for $u \geq 0$ and with v fixed. We will use the Lipschitz constants $L_1 = \max_i\{v_i\}\|A\|_2^2$ and $L_2 = \max_i\{(\hat{v}_{\mathrm{f}})_i\}\|A\|_2^2$.

4.3.2.2   Joint MAP Estimation

The MAP estimation problem (4.21) is a special case of (4.29) if we let $J_3(u) = J(u, \hat{v}(u))$. The gradient of $J_3(u)$ is

$$\nabla J_3(u) = A^T y + D_d(u)^T \hat{v}(u) \tag{4.31}$$
$$= A^T(y - \hat{y}(u, \hat{v}(u)))$$

where $D_d(u) = -\sum_{j=1}^p \mathrm{diag}(\exp(-A_j u))A_j$ denotes the Jacobian matrix of $d(u)$. Comparing with (4.30), we see that the only difference is that the residual

$y - \hat{y}(u, \hat{v}(u))$ is based on the flat-field estimate $\hat{v}(u)$ instead of the true flat-field v or the ML estimate $\hat{v}_{\mathrm{f}}$.

To derive the Hessian of $J_3(u)$, note that

$$c^T \log(d(u)) = \sum_{i=1}^{r} c_i \log(d_i(u))$$

where $d_i(u) = s + \sum_{j=1}^{p} \exp(-e_i^T A_j u) + \beta_i$. This implies that the Hessian can be expressed as

$$\sum_{i=1}^{r} c_i \left(\frac{\nabla^2 d_i(u)}{d_i(u)} - \frac{\nabla d_i(u) \nabla d_i(u)^T}{d_i(u)^2} \right).$$

Now let $\Pi_i = I \otimes e_i^T$ such that $\Pi_i y = Y^T e_i$ corresponds to the ith row of Y, and define a permutation matrix $\Pi = [\Pi_1^T \;\cdots\; \Pi_r^T]^T$. This allows us to express the Hessian $\nabla^2 J_3(u)$ as

$$\nabla^2 J_3(u) = A^T \Pi^T \mathrm{blkdiag}(B_1(u), \ldots, B_r(u)) \Pi A \tag{4.32}$$

where $B_i(u) = \mathrm{diag}(\Pi_i \hat{y}) - \frac{1}{c_i} \Pi_i \hat{y} \hat{y}^T \Pi_i^T$, and where $\hat{y}$ is used as shorthand for $\hat{y}(u, \hat{v}(u))$. (We remark that $\hat{v}(u)$ depends on both α and β, and consequently, so does the Hessian $\nabla^2 J_3(u)$.) It follows that

$$\|\nabla^2 J_3(u)\|_2 \le \|A^T \mathrm{diag}(y) A\|_2$$

which implies that $\nabla J_3(u)$ is Lipschitz continuous with constant $L_3 = \|A^T \mathrm{diag}(y) A\|_2$.

4.3.2.3   WLS Estimation

The quadratic approximation (4.15) corresponds to (4.29) with $J_4(u) = \frac{1}{2}\|Au - b\|_{\widehat{\Sigma}_{\mathbf{b}}^{-1}}^2$ and $\widehat{\Sigma}_{\mathbf{b}} = \mathrm{diag}(y)^{-1}$. The gradient of $J_4(u)$ is

$$\nabla J_4(u) = A^T \Sigma_{\mathbf{b}}^{-1}(Au - b)$$

which is Lipschitz continuous with constant $\|A^T \widehat{\Sigma}_{\mathbf{b}}^{-1} A\|_2$.

4.3.2.4   Regularized SWLS

The quadratic approximation (4.27) corresponds to (4.29) with $J_5(u) = \frac{1}{2}\|Au - b\|_{\widehat{\Sigma}_{\mathbf{b}}^{-1}}^2$ and

$$\widehat{\Sigma}_{\mathbf{b}} = \Pi^T \left[\mathrm{diag}(\Pi y)^{-1} + \mathrm{diag}(s\hat{v}_{\mathrm{f}} + \alpha - \mathbf{1})^{-1} \otimes (\mathbf{1}\mathbf{1}^T) \right] \Pi.$$

Thus, $\widehat{\Sigma}_\mathbf{b}$ is a symmetric permutation of a block-diagonal matrix with diagonal-plus-rank-one blocks, and hence matrix-vector products with $\widehat{\Sigma}_\mathbf{b}^{-1}$ can be efficiently evaluated using the Woodbury identity, $i.e.,$ $\widehat{\Sigma}_\mathbf{b}^{-1} = \Pi^T \mathrm{blkdiag}(S_1, \ldots, S_r)\Pi$ where

$$S_i = \mathrm{diag}(\Pi_i y) - \frac{1}{s(\hat{v}_\mathrm{f})_i + e_i^T Y \mathbf{1} + \alpha_i - 1}\Pi_i y y^T \Pi_i^T. \tag{4.33}$$

This allows us to evaluate the gradient as

$$\nabla J_5(u) = A^T \Sigma_\mathbf{b}^{-1}(Au - b)$$

which is Lipschitz continuous with constant $\|A^T \widehat{\Sigma}_\mathbf{b}^{-1} A\|_2$.

It is instructive to compare the SWLS model to the WLS model considered in [Mohan15]. This model implicitly includes the flat-fields using the following objective function

$$J_6(u, z) = \frac{1}{2}\|\mathrm{diag}(y)^{1/2}(Au - b + \mathbf{1} \otimes z)\|_2^2 + \frac{\lambda}{2}\|z\|_2^2 \tag{4.34}$$

where $z \in \mathbb{R}^r$ is an auxiliary variable that can be thought of as the relative flat-field error (cf. the analysis in Section 4.1.3). Taking the gradient with respect to z and setting it equal to zero yields $z = \mathrm{diag}(Y\mathbf{1} + \lambda\mathbf{1})^{-1}(\mathbf{1}^T \otimes I)\mathrm{diag}(y)(b - Au)$, and using this expression in (4.34) yields

$$J_6(u) = \frac{1}{2}\|Au - b\|_{\widehat{\Sigma}^{-1}}^2 \tag{4.35}$$

where $\widehat{\Sigma}^{-1} = \Pi^T \mathrm{blkdiag}(\bar{S}_1, \ldots, \bar{S}_r)\Pi$ and

$$\bar{S}_i = \mathrm{diag}(\Pi_i y) - \frac{1}{e_i^T Y \mathbf{1} + \lambda}\Pi_i y y^T \Pi_i^T. \tag{4.36}$$

The blocks $\bar{S}_i$ clearly resemble the blocks S_i from the SWLS model in (4.33): the only difference is the scalar weight in front of the rank-1 term in each of the r blocks. In particular, notice that the weights in the SWLS model include information derived from all measurements as well as the flat-field prior. Moreover, the parameter λ in (4.36) plays a similar role as the flat-field hyperparameters α in (4.33), but the SWLS model is more general and flexible because it allows the use of a different hyperparameter α_i for each of the r blocks.

4.3.3   Algorithm

The functions $J_1(u), \ldots, J_5(u)$ are all differentiable with Lipschitz continuous gradients on the nonnegative orthant, and hence we can apply a proximal gra-

dient method which is suitable for minimizing problems of the form

$$\text{minimize} \quad g(u) + h(u).$$

Here $g : \mathbb{R}^n \to \mathbb{R}$ is convex with a Lipschitz continuous gradient with Lipschitz constant L, $h : \mathbb{R}^n \to \mathbb{R}$ is convex, and the prox-operator

$$\text{prox}_{th}(\bar{u}) = \underset{u}{\operatorname{argmin}} \left\{ th(u) + \frac{1}{2} \|u - \bar{u}\|_2^2 \right\}$$

is assumed to be cheap to evaluate. We will define $g(u) = J_i(u) + \gamma \text{TV}_\delta(u)$ and $h(u) = I_+(u)$, and hence the Lipschitz constant is given by $L = L_i + \gamma L_{\text{tv}}(\delta)$. Given a starting point $u^{(0)}$ and a fixed number of iterations K, the algorithm can be summarized as

$$u^{(k)} = \text{prox}_{th}(u^{(k-1)} - t\nabla g(u^{(k-1)})), \ k = 1, 2, \ldots, K$$

where $t \in (0, 2/L)$ is the step size and $\text{prox}_{th}(\bar{u}) = \max(0, \bar{u})$ is the projection onto the nonnegative orthant. With this step size, the method is a descent method. The Lipschitz constant L can be estimated without an explicit representation of A or D by means of the power iteration algorithm. Our MATLAB implementation of the method is available for download at `https://github.com/hariagr/R2CT`.

4.4 Numerical Experiments

4.4.1 Simulation Study

To evaluate the proposed reconstruction models, we conducted a series of experiments in MATLAB based on simulated data. In these experiments, we used a parallel beam geometry with $p = 720$ equidistant projection angles covering half a rotation, and a 2 cm wide photon counting detector array with $r = 512$ detector elements. To model a non-uniform detection efficiency, the elements of the flat-field vector v were drawn from a Poisson distribution with mean I_0. We used $s = 5$ measurements of the flat-field which were generated according to (4.4), and the measurements Y were generated according to (4.2) using a $2N \times 2N$ pixel discretization of a 2D phantom defined on a 4 cm^2 square. To avoid inverse crimes, we computed our reconstructions on an $N \times N$ ($N = 512$) pixel grid with a circular mask. The value of the TV-smoothing parameter δ was 0.01 cm^{-1} in all experiments with the TV-prior. We used as step size $t = 1.8/L$, and we used the ASTRA Toolbox [Aarle15] (version 1.7.1beta) to compute filtered backprojection (FBP) reconstructions and to implicitly compute products

with A and A^T on a GPU. We generated the phantoms using the AIR Tools package [Hansen12] (version 1.3), and we used the method outlined in Section 4.3.3 to numerically solve the reconstruction problems. As a remark, we note that the ASTRA GPU code for backprojection (*i.e.*, multiplication by A^T) is not an exact adjoint of the forward operator (multiplication by A), and this may introduce small errors in the gradient computations. However, it is significantly faster than matched implementations, and we did not see any noticeable differences in reconstruction quality when using the exact adjoint.

As initial guess we used a vector of zeros, and we used a fixed number of iterations as stopping criteria (500 iterations for reconstructions without the TV-prior and 1,500 iterations for reconstructions with the TV-prior). We determine the parameter γ for the TV-prior based on the subjective visualization. As flat-field prior $P(v|\alpha, \beta)$ we used $\alpha_i = 1 + \beta_i(\hat{v}_f)_i$ and $\beta_i \geq 0$ (corresponding to the UP flat-field prior if $\beta_i = 0$ and the FE prior if $\beta_i > 0$), and for the attenuation prior $P(u|\gamma)$ we used either nonnegativity or total variation combined with nonnegativity. Note that SWLS only depends on α, but since we also use $\alpha_i = 1 + \beta_i(\hat{v}_f)_i$ for SWLS, we report the value of β in the experiments.

To quantitatively compare the quality of reconstructions, we report the relative attenuation error (RAE)

$$e_u^{\mathrm{rel}}(\hat{u}) = 100 \cdot \frac{\|\hat{u} - u\|_2}{\|u\|_2},$$

the relative flat-field error (RFE)

$$e_v^{\mathrm{rel}}(\hat{v}) = 100 \cdot \frac{\|\hat{v} - v\|_2}{\|v\|_2},$$

the structural similarity (SSIM) index[1] [Wang04], and a "ring ratio" (RR), defined as

$$\|\psi_v(\hat{v}(\hat{u}))\|_F / \|\psi_v(\hat{v}_f)\|_F$$

with $\psi_v(\hat{v})$ defined as

$$\psi_v(\hat{v}) = \mathrm{FBP}(\mathrm{diag}(v)^{-1}(\hat{v} - v)\mathbf{1}^T) \qquad (4.37)$$

and where FBP denotes the filtered backprojection reconstruction method. In other words, $\psi_v(\hat{v})$ is the FBP reconstruction of the sinogram stripes due to flat-field estimation errors, and hence the norm $\|\psi_v(\hat{v})\|_F$ quantifies how severely the flat-field estimation errors affect the reconstruction. Thus, the RR can be viewed as an indication of the expected ring artifact reduction if we were to use

---

[1]We used the MATLAB `ssim` function with the radius parameter equal to 0.2 for reconstructions without the TV-prior and equal to 2.0 for reconstructions with the TV-prior.
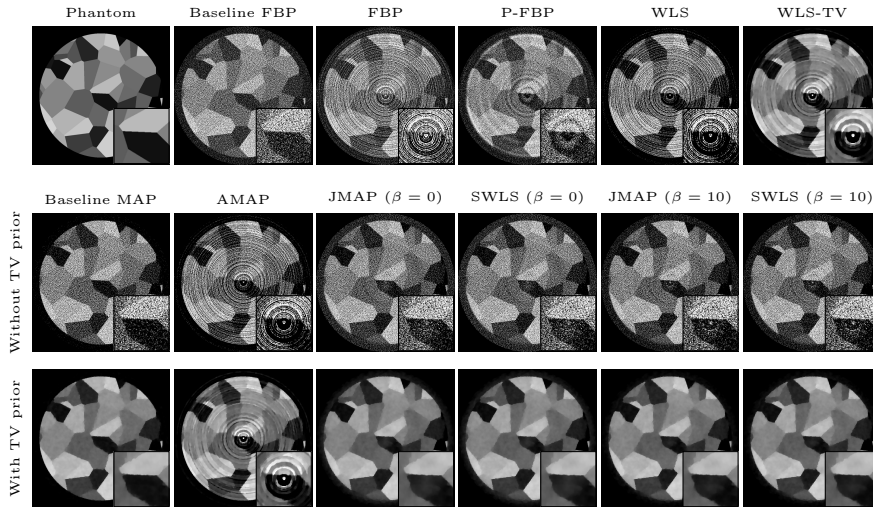
Figure 4.4: Phantom and reconstructions based on simulated low-intensity measurements. The display range for the images is 0 to 1.2 cm^{-1}. The reconstructions with the TV-prior were computed with $\gamma = 3$. The insets are blow-ups of the reconstructions at the isocenter. The number of iterations was 500 for reconstructions without TV prior and 1,500 for reconstructions with TV prior.

the flat-field estimate $\hat{v}(\hat{u})$ instead of the ML estimate $\hat{v}_f$ (smaller is better) to compute a reconstruction. Recall that all but the JMAP reconstruction model are based on the ML estimate $\hat{v}_f$, so for the other models, the RFE and the RR simply reflect what we obtain if we were to use the reconstruction $\hat{u}$ to compute a new flat-field estimate $\hat{v}(\hat{u})$, using (4.22). We used $\alpha = 1$ and $\beta = 0$ to compute $\hat{v}(\hat{u})$ for all but the JMAP and SWLS reconstruction models.

4.4.1.1 Low Intensity

In our first experiment, we used a phantom based on the "grains" phantom from AIR Tools, shown in the upper left corner of Fig. 4.4. We applied a circular mask of radius 0.8 cm to obtain a phantom that is fully contained by the reconstruction grid. We used $I_0 = 500$ in this experiment, corresponding to approximately 500 photons per detector element per projection. As a result, the SNR is relatively low. Estimates based on low SNR measurements generally have a high variance, and hence a good model and strong priors are of paramount importance. The reconstructions shown in Fig. 4.4 demonstrate this. The baseline reconstructions

Model	Without TV (full domain, 2×2 cm)				Without TV (disc, radius 0.8 cm)				TV $\gamma = 3$ (disc, radius 0.8 cm)			
	RAE	SSIM	RFE	RR	RAE	SSIM	RFE	RR	RAE	SSIM	RFE	RR
Baseline FBP	71.9	0.62	0.2	0.03	65.7	0.77	0.2	0.03	-	-	-	-
FBP	101.2	0.55	3.5	0.66	94.7	0.70	3.6	0.66	-	-	-	-
P-FBP	73.1	0.62	1.8	0.20	66.7	0.77	1.6	0.19	-	-	-	-
Baseline MAP	58.7	0.79	0.3	0.04	58.4	0.80	0.2	0.04	6.1	0.93	0.3	0.06
AMAP	77.3	0.72	2.8	0.50	76.9	0.74	2.9	0.52	15.2	0.71	1.7	0.19
WLS	76.9	0.72	2.8	0.50	76.6	0.74	2.9	0.52	15.2	0.71	1.7	0.19
JMAP ($\beta = 0$)	63.8	0.72	5.4	0.25	58.1	0.80	2.7	0.12	8.2	0.92	0.9	0.09
SWLS ($\beta = 0$)	63.9	0.72	5.5	0.26	58.0	0.80	2.7	0.12	8.3	0.92	1.0	0.10
JMAP ($\beta = 10$)	61.8	0.74	3.1	0.20	58.4	0.80	1.5	0.15	7.6	0.92	0.7	0.09
SWLS ($\beta = 10$)	61.8	0.74	3.2	0.20	58.3	0.80	1.4	0.15	7.7	0.92	0.8	0.09
JMAP ($\beta = 50$)	62.0	0.75	2.3	0.30	60.3	0.79	2.0	0.31	7.6	0.91	1.2	0.17
SWLS ($\beta = 50$)	61.9	0.75	2.3	0.30	60.2	0.79	2.0	0.31	7.7	0.91	1.3	0.17

Table 4.1: Error measures for reconstructions based on simulated low-intensity measurements.

were computed using the true flat-field, and hence they are "inverse crime" reconstructions that serve only as a baseline for comparison. The two baseline MAP reconstructions (with and without the TV prior) are based on the model (4.10). Using the flat-field estimate $\hat{v}_{\mathrm{f}}$ instead of the true flat-field, we obtained the FBP and AMAP reconstructions. It is clear from these reconstructions that the flat-field estimation errors introduce severe ring artifacts, even in the presence of a strong prior such as the TV-prior. The ring artifacts are especially severe near the center of the image (cf. Section 4.1.3).

The preprocessed FBP (P-FBP) reconstruction is the result of applying the combined wavelet and FFT filtering preprocessing method[2] by Münch et al. [Münch09] to the sinogram, followed by FBP. This removes stripes from the sinogram, and although there are still some noticeable ring artifacts in the reconstruction, the preprocessing step clearly reduces the severity of the artifacts. However, the preprocessing step involves several parameters that must be carefully tuned, and it does not directly allow us to use the AMAP or MAP-based reconstruction models for reconstruction.

The proposed models are quite effective at reducing ring artifacts, as can be seen from the JMAP reconstructions as well as the SWLS reconstruction. Notice that both the SWLS ($\beta = 0$) reconstruction and the JMAP ($\beta = 0$) reconstruction without the TV prior do not involve any parameters.

---

[2]We used a damping factor of 0.9 and a Daubechies 5 wavelet with a three-level decomposition.
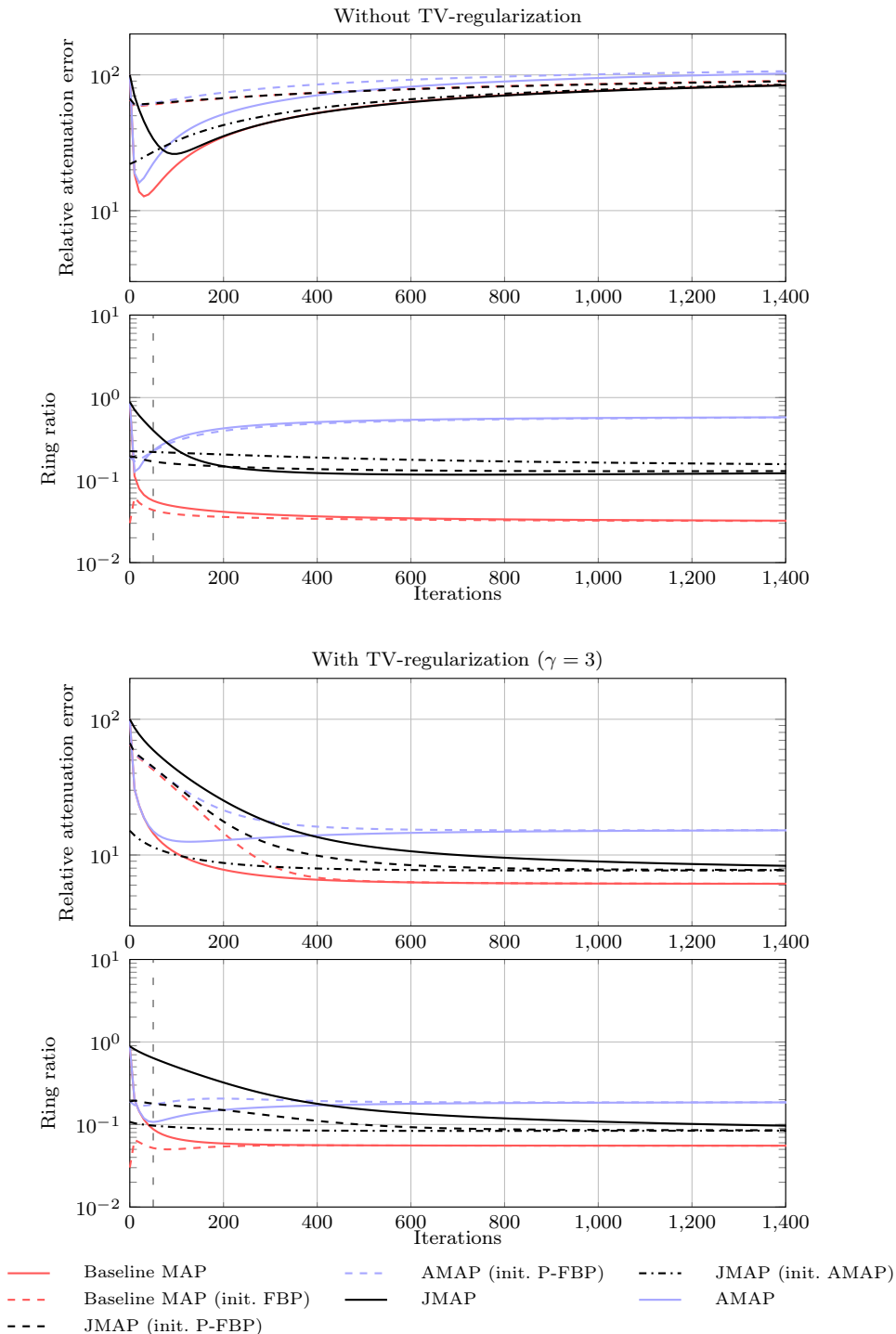
Figure 4.5: Results of semi-convergence and initialization study. Reconstructions are computed with a UP prior $\beta = 0$.

For the experiments without the TV-prior, Table 4.1 shows the error measures based on both the full reconstruction domain and based on a disc of radius 0.8 cm (corresponding to the support of the phantom). The latter approach ignores noise and ring artifacts outside the phantom, and hence this gives a more practical picture of the performance. For the reconstructions with a TV-prior, we report our results based on a disc of radius 0.8 cm. Notice that in all cases, we obtain the best reconstruction (in terms of both RAE and SSIM) using either the JMAP reconstruction model or the SWLS model. Moreover, these reconstructions have RAEs that are similar to those of the baseline MAP reconstructions. We also see that RRs and the RAEs for the JMAP reconstructions appear to be correlated, but interestingly, the RFEs do not seem to agree with the RAEs.

Despite the fact that the P-FBP reconstruction is worse than the JMAP reconstructions, it is interesting to note that it may be used to compute an improved flat-field estimate. In our experiment, the ML estimate $\hat{v}_\mathrm{f}$ had a relative error of 4.8%, but the flat-field estimate computed based on the P-FBP reconstruction had a relative error of only around 1.8%. However, using the TV-prior, the JMAP and SWLS model still produced the best flat-field estimate of all the models.

Finally, we remark that the AMAP and WLS reconstructions may be improved slightly by increasing the parameter γ. Using $\gamma = 10$, we obtained AMAP and WLS reconstructions with a relative error of around 10%, and although these reconstructions did not have noticeable ring artifacts, they contained an increased amount of undesirable TV-artifacts. On the other hand, the JMAP and SWLS reconstructions obtained with $\gamma = 3$ only have a limited amount of ring artifacts and TV artifacts, and hence we conclude that the proposed model allows us to reduce ring artifacts using a smaller regularization parameter γ than with the AMAP or WLS models, thus limiting unnecessary TV-induced artifacts.

4.4.1.2 Semi-convergence and Initialization

We now investigate the role of regularization and its influence on the reconstruction. Recall that X-ray tomographic imaging is an ill-posed problem where a small amount of noise in the measurements may results in a large change in the reconstruction if it is not regularized by a suitable prior. Thus, without regularization, intermediate iterates sometimes provide better reconstructions than iterates close to convergence. This behavior is known as semi-convergence and depends on the reconstruction method as well as initialization. Semi-convergence behavior often indicates that the reconstruction is under-regularized, and hence a solution to our convex reconstruction model may be a poor reconstruction.

In practice it is difficult to rely on semi-convergence as the true solution is unknown.

We use the same experimental setup as in the previous experiment. Fig. 4.5 shows RAE and RR as a function of the number of iterations, with and without the TV-prior (*i.e.*, regularization). The semi-convergence behavior is evident without the TV-prior, and not surprisingly, the baseline reconstruction obtains the lowest RAE at the semi-convergence point after approximately 50 iterations. After the semi-convergence point, noise start to dominate the reconstruction and the RAE starts to increase monotonically. Comparing the AMAP and JMAP models, we see that the AMAP model has a lower RAE at the semi-convergence point, but it converges to a higher RAE. Taking the definition of the AMAP and JMAP estimators into account, we can conclude that the JMAP model still converges to a better reconstruction than the AMAP model. Fig. 4.5 also shows the RR error measure, and while the AMAP model exhibits semi-convergence both with respect to the RAE and the RR, the JMAP model appears to monotonically reduce the RR despite semi-convergence with respect to the RAE.

The dashed curves in Fig. 4.5 show the results of the same experiment, but using the P-FBP reconstruction of u as initialization (the baseline MAP was initialized with the baseline FBP reconstruction). The FBP reconstruction has a smaller RAE than the zero-initialization, but FBP reconstructions may be quite noisy when the SNR is low. Consequently, this initialization may not lead to faster convergence without regularization, as can be seen in Fig 4.5. The figure also shows that the AMAP reconstruction method still exhibits a mild degree of semi-convergence when using the TV-prior, but the baseline method and the JMAP method appear to reduce the RAE and the RR monotonically. Moreover, it is clear that the FBP-initialization helps when combined with the TV-prior. Finally, using the 50th AMAP iterate as initialization for JMAP (corresponding to the semi-convergence point for the RR), we obtained a significant improvement in the number of iterations when compared to initialization with zeros.

4.4.1.3   Noise Analysis

To investigate the noise properties of the proposed reconstruction model, we generated 200 realizations of all measurements based on the grains phantom (see Fig. 4.4) and with $I_0 = 500$. We then computed pixelwise bias (the difference between the mean of the reconstructions and the phantom) and standard deviation for reconstructions based on the baseline MAP, the AMAP, and the JMAP reconstruction models. All reconstructions were computed with the TV-
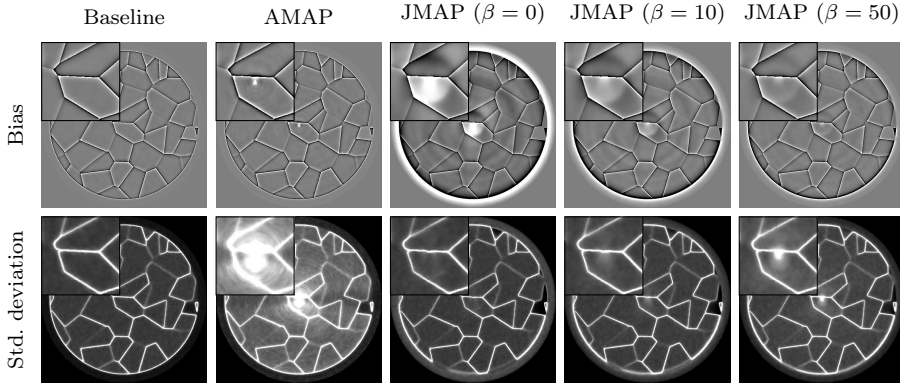
Figure 4.6: Pixelwise bias and standard deviation based on 200 realizations of all measurements. The display range for the bias images is -0.1 to 0.1 cm^{-1}, and the display range for the standard deviation images is 0 to 0.06 cm^{-1}. The reconstructions are computed with TV-prior with $\gamma = 3$. The insets are blow-ups of the reconstructions at the isocenter.

prior ($\gamma = 3$) and 1,500 iterations. The results are shown in Fig. 4.6. Generally speaking, the AMAP model is less biased than the JMAP model. For small values of β, the JMAP bias is somewhat large in comparison to the AMAP bias, especially near the boundary of the object and at the isocenter. However, the JMAP bias decreases when the parameter β is increased, but at the cost of increasing the standard deviation. This is consistent with the fundamental trade-off between bias and variance in statistical learning. More importantly, the standard deviation is significantly lower for the JMAP model in comparison to the AMAP model, and it is even comparable to that of the baseline MAP model when β is small. Notice that in all instances, the standard deviation is particularly large near the interfaces of the grains where the intensity jumps.

Recall from the previous experiment that the flat-field estimate may converge very slowly. As a consequence, the bias component that is induced by flat-field estimation errors decreases slowly as we increase the number of iterations. The results therefore depend on the stopping criteria (*i.e.*, the number of iterations). Finally we note that the noise results for the SWLS model were very similar to those of the JMAP model, and hence we have chosen to omit the SWLS results for the sake of brevity.

4.4.1.4 Flat-field Regularization

Our next experiment demonstrates a potential shortcoming of the proposed model when using the UP flat-field prior for reconstruction. We used the Shepp–Logan phantom for the experiment, but unlike in the previous experiments, we generated the measurements by evaluating the line integrals analytically. The intensity parameter was $I_0 = 10^5$. The reconstruction based on (4.14), the leftmost reconstruction in Fig. 4.7, has some low-level ring artifacts. JMAP with the FE prior and $\beta = 0$ leads to the reconstruction in the middle of Fig. 4.7. Somewhat surprisingly, while the low-level rings are mostly gone, the reconstruction has a few wide and very noticeable rings. These rings arise because of the structure of the flat-field estimation errors which can be seen by looking at the reconstruction $\psi_v(\hat{v})$, defined in (4.37) and shown in Fig. 4.7. Several high-intensity rings appear clearly, and these can be linked to large flat-field estimation errors associated with a small number of detector elements. In particular, the detector elements corresponding to rays that intersect the outer ellipsoidal shell of the Shepp–Logan phantom tangentially give rise to large estimation errors. We remark that we have observed experimentally that these artifacts seem to be exacerbated by the fact that the two outer Shepp–Logan ellipses are centered at the isocenter.

Now recall that the flat-field estimate $\hat{v}(u)$ can be expressed as (4.23), *i.e.*, a convex combination of independent estimates. Thus, the weights θ indicate the emphasis of the different flat-field estimates. The plots in Fig. 4.7 show these weights for two different priors parameterized by β. We see that when $\beta = 0$ (corresponding to the UP flat-field prior), the flat-field estimate is based almost entirely on $\hat{v}_y$, and the estimates $\hat{v}_f$ and $\hat{v}_{pr}$ both receive negligible (but nonzero) weights. Inspecting the corresponding flat-field estimate (the bottom plot in Fig. 4.7) reveals that for $\beta = 0$, the JMAP estimate is worse than the ML estimate $\hat{v}_f$. This indicates over-fitting. To mitigate this, we can emphasize the flat-field ML estimate $\hat{v}_f$ by using the FE prior (*i.e.*, $\alpha = 1 + \beta(\hat{v}_f)$), as described in 4.2.2. Doing so effectively removes the major rings that were present with the FE prior with $\beta = 0$, as shown in the rightmost reconstruction in Fig. 4.7. Moreover, the rightmost plot in the figure confirms that the resulting flat-field estimate depends less on $\hat{v}_y$ than with the FE prior with $\beta = 0$. The FBP reconstructions of the flat-field error, shown below the reconstructions in Fig. 4.7, clearly show a reduction in ring artifacts compared to the basic AMAP and JMAP reconstructions.

Model	Baseline	AMAP	JMAP ($\beta = 0$)	JMAP ($\beta = 50$)
RAE	13.49	17.37	17.56	14.00
RR	0.03	0.60	0.96	0.31
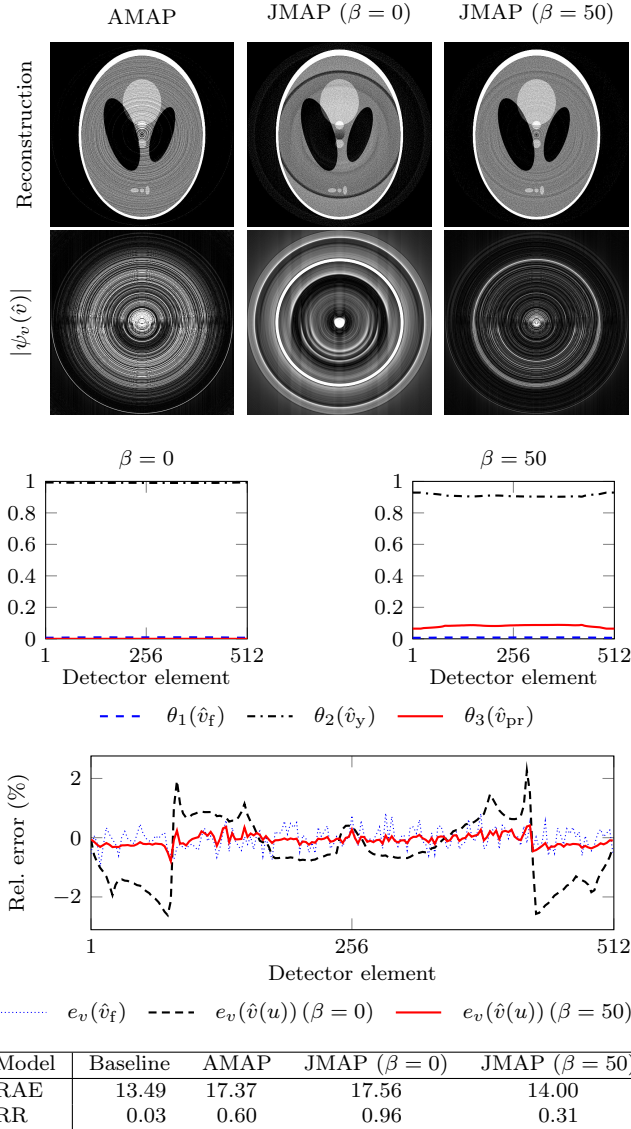
Figure 4.7: Reconstructions of the Shepp–Logan phantom after 1,000 iterations, without the TV-prior on u. The display range for the reconstruction images is 0 to 0.4 cm^{-1}, and 0 to 0.04 for the ring images $\psi_v(\hat{v})$. The first two plots show the values of $\theta_1, \theta_2, \theta_3$, as defined in (4.23), for $\beta = 0$ and $\beta = 50$. The third plot shows the element-wise relative error with respect to true flat-field v, defined as $e_v(\hat{v}) = 100 \cdot \mathrm{diag}(v)^{-1}(\hat{v} - v)$, for the ML flat-field estimate $\hat{v}_{\mathrm{f}}$ and two JMAP flat-field estimates. The table lists the RAE and RR error measures.
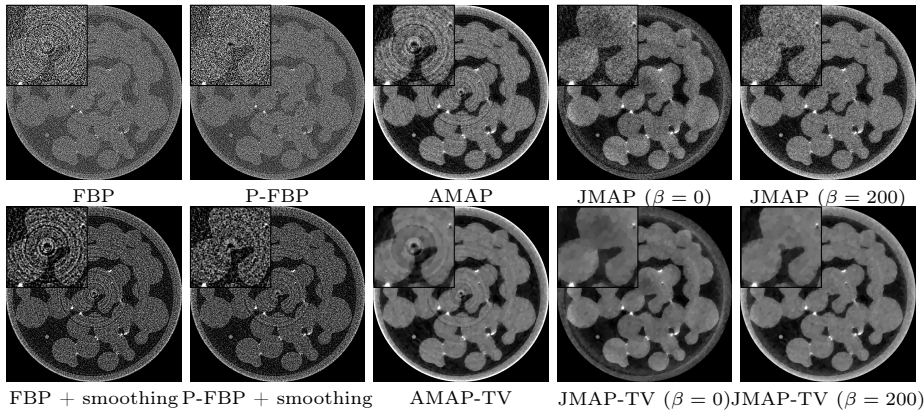
Figure 4.8: Reconstructions of real tomographic measurements. The display
range for the images is 0 to 10 cm^{-1}. The reconstructions using
the TV-prior were obtained with $\gamma = 0.01$. The number of itera-
tions were 50 for reconstructions without TV prior and 1,000 with
TV prior. The insets are blow-ups of the reconstructions at the
isocenter.

4.4.2   Real Data Study

We now evaluate the performance of the proposed model based on real measure-
ment data provided by the Advanced Photon Source (APS) facility operated by
Argonne National Laboratory (USA). The data set provides tomographic mea-
surements of a sample of glass beads with some dried potassium from $p = 900$
projection angles between $0°$ and $180°$ in a parallel beam geometry and with a
600×960 pixel detector array. In this experiment, we will consider only a 2D
reconstruction of the center slice (slice 300) so we take $r = 960$.   The energy of
the X-ray source was 33.27 keV, and the photon flux per pixel in each projection
was approximately 1200 photons/s. With an exposure time of only 6 ms, that
amounts to pixelwise photon counts in the range 0-20 per projection. Out of
a total of 20 flat-field measurements collected before and after the experiment,
8 appear to be corrupted, so we used $s = 12$ flat-field measurements for our
reconstructions. Moreover, we used a square grid with side length 0.3053 cm
and 768×768 pixels for the reconstructions. Our reconstructions are shown in
the Fig. 4.8.

Without the TV-prior on the attenuation image, the reconstructions are quite
noisy because of the low SNR. The FBP reconstruction and the AMAP re-
construction both have ring artifacts which heavily distort the reconstruction.
The P-FBP reconstruction does not have noticeable ring artifacts, but the re-

construction is quite noisy. Thus, to reduce noise, we smoothed the FBP and P-FBP reconstructions using a Gaussian filter with standard deviation 1.0, and although this help, the resulting images are still somewhat noisy compared to the other reconstructions. The JMAP reconstruction with the UP prior ($\beta = 0$) has no noticeable ring artifacts, but it has a significant amount of noise. This is especially noticeable near the circular boundary of the object, and it may be because of flat-field estimation errors. Indeed, using the FE prior with $\beta = 200$ yields a reconstruction that is somewhat improved near the outer circles. Notice that the JMAP reconstructions do not have such a "hole" in the middle like the FBP, P-FBP, and AMAP reconstruction. Finally, including the TV-prior on u results in the AMAP-TV and JMAP-TV reconstructions. These results verify the applicability of proposed model for tomographic reconstruction based on low-intensity measurements.

4.5   Conclusion

In X-ray computed tomography, the X-ray source intensity is typically estimated based on a number of flat-field measurements. This estimation introduces unavoidable errors in popular reconstruction models such as AMAP, WLS, and FBP, and these errors lead to systematic reconstruction errors in the form of ring artifacts. By investigating the filtered backprojection of a line in the sinogram, we have demonstrated that such systematic errors introduce structural changes in the reconstruction in the form of a ring. Based on the statistics of X-ray measurements, our analysis shows an inverse relationship between severity of ring artifacts and the source intensity. Therefore, these systematic errors can have a significant impact on the reconstruction quality of dose-constrained and time-constrained problems. To mitigate this problem, we have introduced a convex reconstruction model (JMAP) that jointly estimates the attenuation image and the flat-field. We have also introduced a quadratic approximation of the JMAP model, the stripe-weighted least-squares (SWLS) model, which provides insight about the model and its similarities with existing models.

To assess the reduction of ring artifacts in the reconstructions, we have proposed a "ring ratio" error measure which quantifies the flat-field error in the image domain. Our experimental results indicate that the model effectively mitigates ring artifacts even for low SNR data, not only with simulated data but also with real data sets. In some cases, the proposed method may itself introduce artifacts when not appropriately regularized. These artifact essentially arise because of overfitting, and we have shown that they can be mitigated or supressed by means of a suitable regularizing flat-field prior. Moreover, we have shown experimentally that the JMAP and the SWLS models have similar performance

in terms of noise and reconstruction quality.

Finally, we mention that the proposed methodology can readily be extended to estimate a time-varying flat-field which may be useful in applications where the flat-field does not remain stable while acquiring the tomographic measurements and/or when the scanner acquires projection images and flat-field images in an interleaved temporal order.

4.A   Extrema of the Radial Profile

The extrema of the radial profile $\tilde{\mu}(\rho)$, defined in (4.9), depend on the parameters t_0 and $\epsilon > 0$. To see this, we derive the critical points of $\tilde{\mu}(\rho)$. Setting the derivative equal to zero yields the equation

$$\tilde{\mu}'(\rho) = -3\rho \left(\sigma(\sigma^2 + \rho^2)^{-5/2} + \bar{\sigma}(\bar{\sigma}^2 + \rho^2)^{-5/2} \right) = 0$$

where $\sigma = \epsilon + it_0$. It follows that the critical points are $\rho = 0$ and any solution to the equation

$$\sigma(\sigma^2 + \rho^2)^{-5/2} + \bar{\sigma}(\bar{\sigma}^2 + \rho^2)^{-5/2} = 0,$$

or equivalently, $\rho = 0$ and solutions to the equation

$$\frac{\sigma}{\bar{\sigma}} = -\left(\frac{\sigma^2 + \rho^2}{\bar{\sigma}^2 + \rho^2} \right)^{5/2}.$$

Taking the complex logarithm of both sides of the equation yields the equation $2\angle\sigma + 2k\pi = \pi + 5\angle(\sigma^2 + \rho^2), k \in \mathbb{Z}$, and hence

$$\angle(\sigma^2 + \rho^2) = \frac{2}{5}\angle\sigma + \frac{2k-1}{5}\pi, \quad k \in \mathbb{Z}. \tag{4.38}$$

This implies that the tangent of $\angle(\sigma^2 + \rho^2)$ is equal to

$$\frac{2\epsilon t_0}{\rho^2 + \epsilon^2 - t_0^2} = \tan\left(\frac{2}{5}\angle\sigma + \frac{2k-1}{5}\pi \right), \quad k \in \mathbb{Z}, \tag{4.39}$$

or equivalently, if we define $c_k^{-1} = \tan\left(\frac{2}{5}\angle\sigma + \frac{2k-1}{5}\pi \right)$ and solve for ρ^2, we get $\rho^2 = 2\epsilon t_0 c_k + t_0^2 - \epsilon^2, k \in \mathbb{Z}$. Thus, in addition to $\rho = 0$, the real roots of the right-hand side of this equation are the critical points of $\tilde{\mu}(\rho)$, and hence we may limit our attention to $k \in \mathbb{Z}$ for which $2\epsilon t_0 c_k + t_0^2 - \epsilon^2 \geq 0$.

In order to find the extrema of $\tilde{\mu}(\rho)$, we now rewrite (4.9) as

$$\tilde{\mu}(\rho) = \frac{1}{4\pi} \frac{|\sigma|}{|\sigma^2 + \rho^2|^{3/2}} \cos(\angle\sigma - \angle(\sigma^2 + \rho^2)).$$

At a nonzero critical point $\rho_k \neq 0$, the angle $\angle(\sigma^2 + \rho_k^2)$ is given by (4.38), and it follows from (4.39) that

$$|\sigma^2 + \rho_k^2| = 2\epsilon|t_0| \left(c_k^2 + 1\right)^{1/2}.$$

This allows us to express the extrema associated with ρ_k as

$$\tilde{\mu}(\rho_k) = \frac{(\epsilon^2 + t_0^2)^{1/2}}{4\pi(1 + c_k^2)^{3/4}(2\epsilon|t_0|)^{3/2}} \cos\left(\frac{2}{5}\angle\sigma + \frac{2k-1}{5}\pi\right),$$

and it immediately follows that for $|t_0| \gg \epsilon$, the extrema are approximately inversely proportional to $\sqrt{\epsilon^3|t_0|}$.

4.B   Interpretation of Flat-field Estimate

The ith element of flat-field estimate $\hat{v}$, defined in (4.22), is given by

$$\hat{v}_i(u) = \frac{\mathbf{1}^T f_i + \mathbf{1}^T y_i + \alpha_i - 1}{d_i(u)} \tag{4.40}$$

where $f_i \in \mathbb{R}^s$, $y_i \in \mathbb{R}^p$, $d_i(u) = s + \tau_i(u) + \beta_i$, and $\tau_i(u) = \sum_{j=1}^p \exp(-e_i^T A_j u)$. This expression can be reformulated as

$$\hat{v}_i(u) = \frac{s}{d_i(u)} \frac{\mathbf{1}^T f_i}{s} + \frac{\tau_i(u)}{d_i(u)} \frac{\mathbf{1}^T y_i}{\tau_i(u)} + \frac{\beta_i}{d_i(u)} \frac{\alpha_i - 1}{\beta_i}$$
$$= \frac{s}{d_i(u)} (\hat{v}_{\mathrm{f}})_i + \frac{\tau_i(u)}{d_i(u)} (\hat{v}_{\mathrm{y}})_i + \frac{\beta_i}{d_i(u)} \hat{v}_{\mathrm{pr}}(\alpha_i, \beta_i) \tag{4.41}$$

where the ML estimate $\hat{v}_{\mathrm{f}}$ is defined in (4.5), the estimate $\hat{v}_{\mathrm{y}}(\hat{u})$ is defined in (4.16), and

$$\hat{v}_{\mathrm{pr}}(\alpha, \beta) = \mathrm{diag}(\beta)^{-1}(\alpha - \mathbf{1})$$

is the mean of the Gamma prior. It follows from the definition (4.20), *i.e.*, $d_i(u) = s + \tau_i(u) + \beta_i$, that

$$\frac{s}{d_i(u)} + \frac{\tau_i(u)}{d_i(u)} + \frac{\beta_i}{d_i(u)} = 1$$

and hence $\hat{v}_i(u)$ is a convex combination of three estimates. Thus, the full flat-field vector $\hat{v}(u)$ can be expressed as

$$\hat{v}(u) = \mathrm{diag}(\theta_1)\hat{v}_{\mathrm{f}} + \mathrm{diag}(\theta_2)\hat{v}_{\mathrm{y}}(\hat{u}) + \mathrm{diag}(\theta_3)\hat{v}_{\mathrm{pr}}(\alpha, \beta)$$

where $\theta_1 = \mathrm{diag}(d(u))^{-1}s\mathbf{1}$, $\theta_2 = \mathrm{diag}(d(u))^{-1}\tau(u)$, and $\theta_3 = \mathrm{diag}(d(u))^{-1}\beta$ with $\theta_1 + \theta_2 + \theta_3 = \mathbf{1}$.

4.C Type-II ML Estimation of Hyperparameters

The marginal probability of $f_{i1}, \ldots, f_{is}$ given the hyperparameters α_i and β_i can be computed analytically and is given by

$$
\begin{aligned}
\mathrm{P}(f_{i1}, \ldots, & f_{is} \mid \alpha_i, \beta_i) \\
&= \int_0^\infty \mathrm{P}(f_{i1}, \ldots, f_{is} \mid v_i) \mathrm{P}(v_i \mid \alpha_i, \beta_i) dv_i \\
&= \frac{\Gamma(k_i + \alpha_i)}{\left(\prod_{k=1}^s f_{ik}!\right) \Gamma(\alpha_i) s^{k_i}} \left(\frac{\beta_i}{s + \beta_i}\right)^{\alpha_i} \left(\frac{s}{s + \beta_i}\right)^{k_i} \quad (4.42)
\end{aligned}
$$

where $k_i = \sum_{k=1}^s f_{ik}$. Here the identity $\int_0^\infty x^b e^{-ax} dx = \frac{\Gamma(b+1)}{a^{b+1}}$ was used to derive this expression. This probability distribution resembles the negative binomial distribution, and it follows from the first-order optimality conditions associated with (4.24) that $\beta_i = s\alpha_i/k_i$, or equivalently, $\alpha_i/\beta_i = k_i/s$. This implies that the mean of the Gamma prior is equal to the flat-field ML estimate $(\hat{v}_f)_i$. Substituting the expression for β_i in (4.24), we obtain the one-dimensional problem $\mathrm{argmin}_{\alpha_i} \kappa_i(\alpha_i)$ where

$$
\kappa_i(\alpha_i) = -\log \frac{\Gamma(k_i + \alpha_i)}{\Gamma(\alpha_i)} - \alpha_i \log \frac{\alpha_i}{\alpha_i + k_i} - k_i \log \frac{k_i}{\alpha_i + k_i}.
$$

The derivative of $\kappa_i(\alpha_i)$ is

$$
\begin{aligned}
\kappa_i'(\alpha_i) &= -\left[F(k_i + \alpha_i) - F(\alpha_i) - \log\left(1 + \frac{k_i}{\alpha_i}\right) \right] \\
&= -\sum_{l=0}^{k_i - 1} \frac{1}{\alpha_i + l} + \log\left(1 + \frac{k_i}{\alpha_i}\right),
\end{aligned}
$$

where $F(x)$ denotes the digamma function. Similarly, the second derivative is given by

$$
\kappa_i''(\alpha_i) = \sum_{l=0}^{k_i - 1} \frac{1}{(\alpha_i + l)^2} - \frac{k_i}{\alpha_i(\alpha_i + k_i)} \quad (4.43)
$$

where the summation satisfies the inequality

$$
\begin{aligned}
\sum_{l=0}^{k_i - 1} \frac{1}{(\alpha_i + l)^2} = \sum_{n=\alpha_i}^{\alpha_i + k_i - 1} \frac{1}{n^2} &> \int_{\alpha_i}^{\alpha_i + k_i} \frac{1}{x^2} dx \\
&= \frac{k}{\alpha_i(\alpha_i + k_i)} \quad (4.44)
\end{aligned}
$$

for $\alpha_i > 0$. This shows that $\kappa_i''(\alpha_i) > 0$ for $\alpha > 0$, and hence κ_i is convex on the positive real line. Moreover, since $\kappa'(\alpha_i)$ tends to zero as as α_i tends to infinity, $\kappa'(\alpha_i)$ can not have a positive zero. Consequently, the resulting flat-field Gamma prior has zero variance (*i.e.*, α_i/β_i^2 tends to zeros for $\alpha_i \to \infty$ since $\beta_i = s\alpha_i/k_i$) and its mean is equal to the empirical flat-field estimate, *i.e.*, $\alpha_i/\beta_i = (\hat{v}_{\mathrm{f}})_i$.

CHAPTER 5

Non-corresponding Image Registration Models

Image registration [Modersitzki04; Modersitzki09; Brown92; Maintz98; Lester99; Zitová03; Sotiras13] is a technique to estimate point to point correspondences between images that represent physical states of an object or of multiple objects. For example, image registration allows comparing complementary information from CT and MRI images of a patient to diagnose a disease [Dean12]. Mathematically, image registration is an ill-posed problem in the sense of Hadamard's well-posedness. Generally, ill-posedness is addressed by introducing additional prior information, e.g., by using a physical evolution model of a material.

In some applications, images for registration may represent the physical states of a deforming object at different time instants. The physics behind the evolution process has been extensively studied in the field of continuum mechanics [Holmes09]. An object evolves or deforms due to the application of an external force or other physical factors, e.g., temperature change, pressure variation, etc. The deforming object rests at its equilibrium state when internal and external forces balance each other; the entire system possesses minimum potential energy. The deformation of a material is defined as the departure of a material from its reference configuration to its deformed state. Internal forces in a material depend on the properties of a material such as Young modulus and Poisson ratio for an elastic material. Moreover, the evolution process can be described

mathematically by following fundamental physical laws, such as conservation of energy, conservation of mass, and conservation of momentum which are applicable for all types of materials. In addition, we can embed additional information about the specific material through their constitutive relationship. The constitutive relationship defines the relation between two physical quantities which is specific to a material and approximates the response of a material to external forces. For example, the constitutive relationship for a linear elastic material says that the stress is linearly dependent on the internal strain.

Chaim [Chaim81] was one of the first to introduce concepts from continuum mechanics to design an image registration model. He represents images used for registration as a linear elastic material, enabling the deformation field to follow a linear elasticity model. In another point of view, Broit enforces a prior knowledge about the deformation which also addresses the ill-posedness of the image registration model. He uses the minimum total potential energy principle to frame a variational image registration model. According to this principle, the deformed material possess minimum potential energy at its equilibrium state; internal elastic forces and external driving forces balance each other. The work done due to the forces can also be expressed in terms of potential energies.

In the context of image registration, the driving force should be applied such that features of a reference image match with the deformed template image, at least locally. Therefore, driving forces act over all spatial points in the domain depending on the images, its feature of interest, and the deformation field; whereas driving forces are independent of deformation field in usual continuum mechanics. The potential energy due to driving forces is known as a "similarity measure" in the field of image registration. The internal elastic force, in the case of an elastic material, oppose the driving force to achieve a regular and smooth deformation field. The stored elastic energy potential due to internal forces is also called the regularization energy in the field of image registration. The total potential energy of the system is the sum of potential energy $\mathcal{S}$ due to the driving force and the stored elastic energy $\mathcal{E}$ due to the internal forces. Following the principle of minimum total potential energy, a variational image registration model is expressed as

$$\underset{f}{\text{minimize}} \int_{\Omega} \mathcal{S}(x, f, T, R) \ dx + \alpha \int_{\Omega} \mathcal{E}(x, f, \nabla f(x)) \ dx. \tag{5.1}$$

A reference image R and a template image T for registration are generally assumed to belong to a space of all $d-$dimensional images and are compactly supported scalar functions on a domain $\Omega \subset \mathbb{R}^d$. The deformation field $f :$ $\Omega \subset \mathbb{R}^d \mapsto \mathbb{R}^d$ is also called a correspondence map in the context of image registration. The regularization parameter α represents the elastic stiffness of a material. The rigidity of deformation increases with increasing stiffness parameter. Generally, we assume that material is equally stiff everywhere; thus α

is independent of spatial coordinates. The model (5.1) implicitly assumes that every feature in a reference image has a suitable match in the template image. Moreover, in the most of the practical applications, it is desirable that every point in the reference image has a unique match in the template image, and features preserve their orientation and do not cross over each other. Therefore, a one-to-one and an orientation-preserving correspondence map almost everywhere in the spatial domain is an essential desirable feature between a given set of images. We achieve these properties by restricting the Jacobian determinant of deformation field to be positive in the entire domain. Therefore, we refer to (5.1) as a corresponding image registration (CIR) model. Moreover, both forward and backward map between reference and template image should be one-to-one and inverse consistent [Christensen01a].

The formulation of a similarity measure depends on the application in hand and set of features which we intend to match in given images. The most common features are intensity and edges. One of the intensity based similarity measures is simply a sum of squared differences (SSD) between a deformed template and a reference image. Ideally, the goal is to estimate a deformation field such that $T(f) \approx R$. The normalized gradient fields (NGF) [Haber06] similarity measure exploits intensity changes in the images. This is a suitable measure for images from different modalities where it is assumed that the intensity changes appear at corresponding positions. In mass preserving applications [Gigengack12], the intensity of an image varies in proportion to the local change in volume, therefore a similarity measure also incorporates the volume change in the formulation.

There are numerous works to apply physically motivated regularization energies in image registration. The linear elastic models are suitable only for small deformations. For large deformations, the nonlinear hyperelastic energies [Rabbitt95; Darkner11], *e.g.*, Saint Venant–Kirchhoff energy, Riemannian elastic energy [Pennec05], and polyconvex elastic energy [Droske04; Burger13] have been studied in the image registration community. A well desired diffeomorphic deformation field can also be guaranteed through the hyperelastic regularization energy [Burger13]. The viscous fluid flow models are also suitable for large non-linear deformations fields [Christensen96]. Besides physical motivation, few regularizers have been proposed based on the smoothness properties of deformation field, i.e., diffusion [Fischer02], total-variation [FrohnSchauf08; Chumchob13], and curvature regularizer [Fischer04]. The diffusion and total-variation regularizers are based on the L2-norm and L1-norm of first order derivative of displacement field respectively while curvature regularization is based on the second order derivative. The total-variation regularizer allows discontinuities in the deformation field. The regularizers based on elasticity, fluid, and first order derivative penalize affine linear rigid transformations, therefore a pre-registration step is unavoidable. However, curvature regularizer has a null space containing harmonic functions and affine linear rigid transformations, therefore

it does not penalize such transformations. Moreover, a deformation field is smoother for curvature regularizer in respect of regularizers based on first order derivative.

The underlying assumptions of CIR model, *i.e.*, correspondence almost everywhere, fails if few features of a reference image do not match with features in a template image. Section 5.1 introduces two non-corresponding problems with their underlying physical characteristics. We propose, in section 5.2, an image registration framework, mainly inspired from damage mechanics, to solve the non-corresponding problem where images have cracks. Section 5.3 explains basic properties of the proposed registration model. In section 5.4, we present a discrete registration model inspired from fracture mechanics and establish a relationship with the model inspired from the damage mechanics. In section 5.5, we propose an image registration model for the non-corresponding model where images have missing structures. We also establish the relationship between our proposed model with the previously proposed models for images with missing structures. Section 5.6 explains a numerical scheme based on the discretize-then-optimize framework. We further demonstrate the potential of the proposed model through simple academic examples in section 5.7. Section 5.8 concludes our findings.

5.1   Problem Formulation

Much of the research in image registration has focused on identifying the corresponding map, assuming the existence of one-to-one correspondence map almost everywhere in the spatial domain between given images. In other words, every feature in a reference image has a unique match in the template image. This assumption fails if one of the images has a tumour and the other does not, a part of a histological image is fractured into two parts after staining, or materials are glued together in a chemical process. In these situations, one-to-one correspondence does not exist everywhere between the given physical states. These problems are known as a partial data [Periaswamy06], missing correspondence or missing structure [Chitphakdithai10; Nithiananthan12; Berendsen14], registration with inconsistent image differences [Richard04], registration with outliers [Kim04], or a non-correspondence [Chen15; Drobny15] image registration problem in the literature. In this work, we are discussing mainly two types of non-corresponding problems as shown in Fig.5.1 and Fig.5.3.

The reference images in Fig. 5.1 and Fig. 5.3 represent the initial state of an object having a light gray intensity on a lighter background and defined on a domain $\Omega_R \subset \mathbb{R}^2$. Similarly, the template images represent a deformed state of

the object where the object domain is $\Omega_T \subset \mathbb{R}^2$ after the deformation. Notice that, there are different types of local deformations in Fig. 5.1 and Fig. 5.3 which illustrate two types of non-corresponding problems of our interest in this thesis.

5.1.1 Problem 1: Images with Cracks
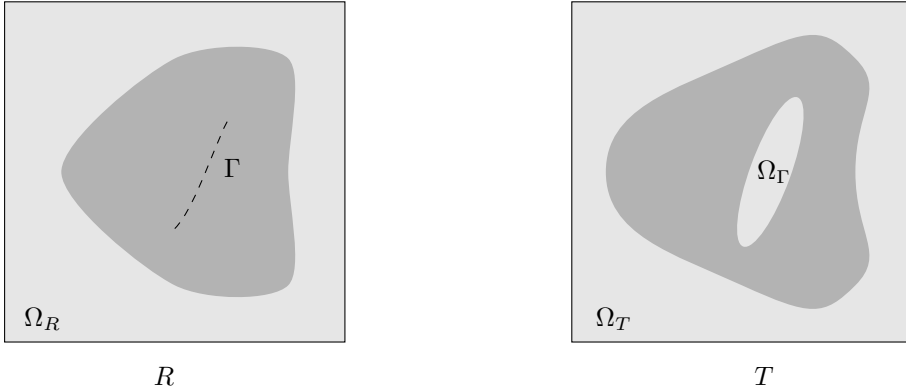
Figure 5.1: The image R represents the initial state of an object where Γ represent the spatial location where a crack originates. The image T represents the deformed state after the crack formation where Ω_Γ represents area occupied by a crack.

The first problem is concerned with cracks and cavity in a material. Physically, a crack is a space between two surfaces which have broken or been split as shown in Fig. 5.1. Suppose that a crack originates at some location Γ in the domain Ω_R of the reference image, and after formation, occupies a region Ω_Γ, as represented in the template image. These images should be registered such that

- the forward map $f : \Omega_R \backslash \Gamma \subset \mathbb{R}^2 \mapsto \Omega_T \backslash \Omega_\Gamma \subset \mathbb{R}^2$ is a one-to-one function, and

- the backward map $g : \Omega_T \backslash \Omega_\Gamma \subset \mathbb{R}^2 \mapsto \Omega_R \backslash \Gamma \subset \mathbb{R}^2$ is a one-to-one function.

In the above definitions, the deformation fields are defined only on a part of the domain instead of the full domain. The particles lying on the region Ω_Γ do not have any suitable match in the domain Ω_R. Moreover, the forward deformation field has a discontinuity along the line Γ, which we will explain in the next paragraph. Here, we refer to Γ and Ω_Γ as non-corresponding regions.
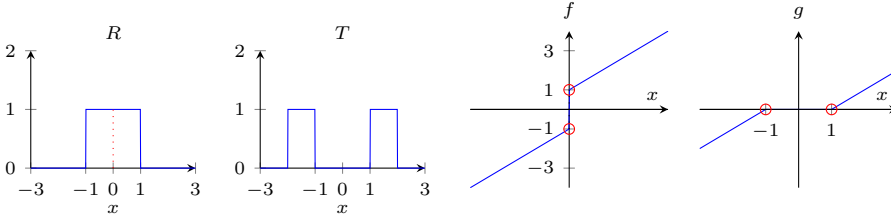
Figure 5.2: One-dimensional example to illustrate discontinuities and non-smoothness in the deformation field due to the formation of a crack and the closing of a crack. The forward deformation field is a discontinuous function where the jump discontinuity arises at the location where the crack originates. Whereas, the backward deformation field is a non-smooth continuous function.

In continuum mechanics, a crack in a material is represented mathematically by a jump discontinuity in the deformation field [Francfort98]. We would like to illustrate this behaviour through a simple one-dimensional academic example, as shown in Fig. 5.2, where a material breaks into two parts. The crack develops in the undamaged state R of a material at spatial location $x = 0$, and the material attains a deformed configuration T. We describe the movement of particles through a deformation field $f : \mathbb{R} \mapsto \mathbb{R}$ such that $T(f) \approx R$, where the deformation field f is given by

$$f(x) = \begin{cases} x + 1 & x > 0 \\ x - 1 & x < 0 \\ 0 & x = 0 \end{cases}.$$
(5.2)

The deformation field f has a jump discontinuity at the crack interface $x = 0$, as shown in Fig. 5.2. We also observe jump discontinuities in higher dimensions; therefore, mathematically, a crack interface is expressed as a set of jump discontinuities.

In the context of image registration, it is equally important to understand the movement of particles from the state T to R, *i.e.*, the closing of a crack. The backward deformation field g is given by

$$g(x) = \begin{cases} x + 1 & x < -1 \\ x - 1 & x > 1 \\ 0 & -1 \leq x \leq 1 \end{cases}.$$
(5.3)

The deformation field g is a non-differentiable continuous function at two points $x \in \{-1, 1\}$.

Our one-dimensional example shows that the forward and backward map for images with cracks possesses different types of properties. In this work, we propose an image registration model where we satisfy these properties of deformation fields only in the approximate sense, following the work by [Bourdin00; Henao16]. In general, it is difficult to estimate jump functions numerically. Therefore, it is always preferable to work in a continuous setting and approximate a discontinuous function with a continuous function defined on an infinitesimally small discretisation of a spatial domain. In this preliminary work, we assume that the deformation field is a smooth, a one-to-one, and an orientation-preserving function. Our proposed model estimate the deformation field as well as identify the location of cracks in the images.

5.1.2 Problem 2: Images with Missing Structures

$$R \qquad\qquad T$$
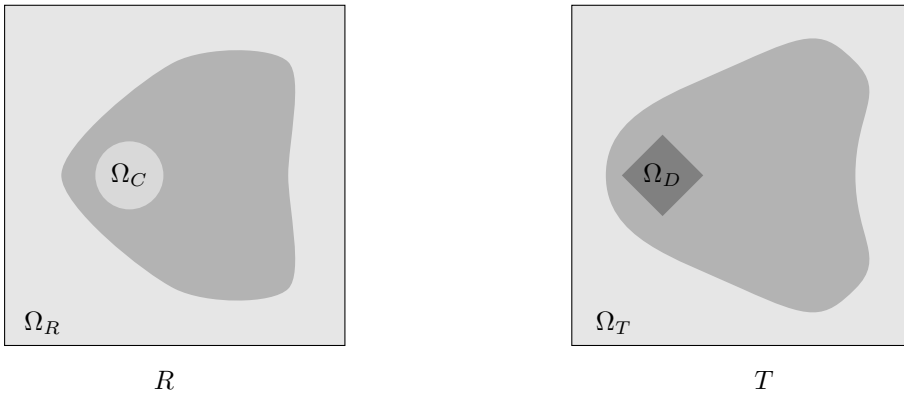
Figure 5.3: Images R and T represent two physical states of an object. The structures inside the region Ω_C of the image R has been completely changed during the deformation, and a new structure has been formed occupying the region Ω_D in the deformed state T.

In this problem, some parts of a reference image do not find any suitable match in the template image and vice-versa, for example, MRI scans of a patient before and after successful tumor surgery. In the Fig. 5.3, features inside the region Ω_C of the reference image do not match with any feature in the template image. Similarly, features inside the region Ω_D do not find any match in the reference image. However, nearby regions outside Ω_C in the reference image match with nearby regions outside Ω_D in the template image. These images should be registered such that

- the forward map $f : \Omega_R \backslash \Omega_C \subset \mathbb{R}^2 \mapsto \Omega_T \backslash \Omega_D \subset \mathbb{R}^2$ is a one-to-one function,

and

- the backward map $g : \Omega_T \setminus \Omega_D \subset \mathbb{R}^2 \mapsto \Omega_R \setminus \Omega_C \subset \mathbb{R}^2$ is a one-to-one function.

We refer to Ω_C and Ω_D as non-corresponding regions.

Unlike the deformation field for images with cracks, the deformation field for images with missing structures does not possess any special characteristics in the non-corresponding regions. A number of authors have proposed image registration models to align images with missing structures. In general, these models identify non-corresponding regions through a dissimilarity measure, and masks these regions to estimate a regularized deformation field in the corresponding regions [Periaswamy06; Chitphakdithai10; Nithiananthan12; Berendsen14; Richard04; Kim04; Chen15; Drobny15]. In this work, we also propose an image registration model for images with missing structures following the similar ideas as proposed previously by other authors. But, our formulation is different and has some similarities with the model proposed for images with cracks as well as has similarities with the previously proposed models.

5.2 Image Registration Model for Images with Cracks

In this section, we propose an image registration model for images with cracks based on the underlying physics of a crack formation. In fracture mechanics, a crack in a material is represented mathematically by a jump discontinuity in the deformation field [Francfort98]. However, in damage mechanics, a crack is identified through the stiffness of a material [Marigo16], and the deformation field is assumed to be a continuous function. It has been found in the field of mechanics that these two ideas are approximately related [Sicsic13]. In this work, we derive an image registration model following the two fundamental principles of the formation of a crack in a material, mainly inspired from damage mechanics [Marigo16]. These principles are:

- The material lose its stiffness entirely at the location of a crack.

- The material dissipates energy proportional to the crack surface.

Stiffness reflects the rigidity of a material. The less stiff the material is, the easier to deform or stretch it is. A close to zero stiffness allows extreme stretching of a

material, and due to this, a crack may form in the material. The internal elastic energy of the material also decreases with decreasing stiffness. We assume, when a crack forms, the material dissipates energy to balance the loss in the internal elastic energy satisfying the law of conservation of energy. In fracture mechanics, the dissipated energy is called the surface energy [Griffith21].

The dissipation energy carries information about the crack, which we need to model mathematically to design a registration model. We introduce a scalar phase field function $p : \Omega \subset \mathbb{R}^d \mapsto [0,1)$ that varies smoothly between 0 to 1 and defines the severity of damage in a material. Sometimes, we call phase field function a soft crack indicator function. The value 0 corresponds to an undamaged zone, *i.e.*, a non-crack region, and 1 a completely damaged zone, *i.e.*, the location of a crack. Now, we define the dissipation energy $\mathcal{D}(p)$ and a stiffness function $e(p)$ as a function of the phase field function p. Following the two principles of the formation of a crack, the dissipation energy should be at its maximum and the stiffness function should be at its minimum when a crack forms in the material or say when p approaches to 1. As discussed before, the internal elastic energy of the material varies with the stiffness of the material, therefore elastic energy depends on the varying stiffness function $e(p)$.

The driving forces are the cause of deformation in a material. In the image registration context, the similarity measure plays the role of a driving force. We assume that the non-crack regions guides the main registration process where we are assured of one-to-one correspondence between features of the given images. Therefore, as per our assumption, similarity measure should act only on the non-crack region by masking the crack region through a mask function $s(p)$. Following all the above mentioned assumptions, the total potential energy of the system, in the case of the crack formation, is the sum of potential energy due to the driving force, the internal elastic energy, and the dissipated energy, *i.e.*,

$$\mathcal{J}(f,p) = \int_\Omega \Big(s(p(x))\mathcal{S}(x,f,T,R) + \alpha e(p(x))\mathcal{E}(x,f,\nabla f(x)) + \beta \mathcal{D}(p(x)) \Big). \tag{5.4}$$

Following the minimum total potential energy principle, the variational image registration model is expressed as

$$\underset{f,p}{\text{minimize}}\, \mathcal{J}(f,p). \tag{5.5}$$

We refer to model (5.5) as a non-corresponding image registration (NCIR) model. In mechanics, the dissipation energy function is generally assumed [Marigo16] to be

$$\mathcal{D}(p(x)) = w(p(x)) + \frac{1}{2}l^2\|\nabla p(x)\|_2^2, \tag{5.6}$$

where $w(p)$ formulates local contributions and $\|\nabla p\|_2^2$ is the non-local contributions in the dissipation energy of a material due to damage. p is a dimensionless quantity, therefore a length constant l needs to be introduced to match the dimensions. In mechanics, l is known as the internal length which controls the width of the crack zone. β is a regularization parameter which varies the toughness of a material. The toughness refects the ability of a material to break. The less tough the material is, easier to break it is.

5.3   Properties

As per our model assumptions, the model (5.5) should satisfy following properties:

1. The total energy of the system should always be non-negative and finite.

2. The stored elastic energy $\mathcal{E}$ and similarity measure $\mathcal{S}$ are non-negative functions.

3. The stiffness function $e(p)$ is a positive strictly decreasing function which decreases from 1 to 0 when p grows from 0 to 1, *i.e.*, $e'(p(x)) < 0$, as shown in Fig. 5.4(a). A material loses its stiffness monotonically based on the severity of damage.

4. The local part of dissipated energy $w(p)$ is a positive strictly increasing function of p, increasing from 0 when $p(x) = 0$ to a finite positive value when $p(x) = 1$, *i.e.*, $w'(p(x)) > 0$, as shown in Fig. 5.4(b). A material releases energy monotonically based on the severity of damage.

5. The similarity mask function $s(p)$ is a positive strictly decreasing function, *i.e.*, $s'(p(x)) < 0$, which decays as p grows from 0 to 1.

6. The regularization parameters α and β are non-negative scalars.

The properties $P3$ and $P4$ follows from the two fundamental principles of the formation a crack, as described in the previous section. We prove the property $P5$ later in this section.

5.3.1   Study of Euler-Lagrange Equation

Ideally, the phase field function value is 0 in the non-crack region and 1 in the crack region. As per our model assumptions, the phase field function is a
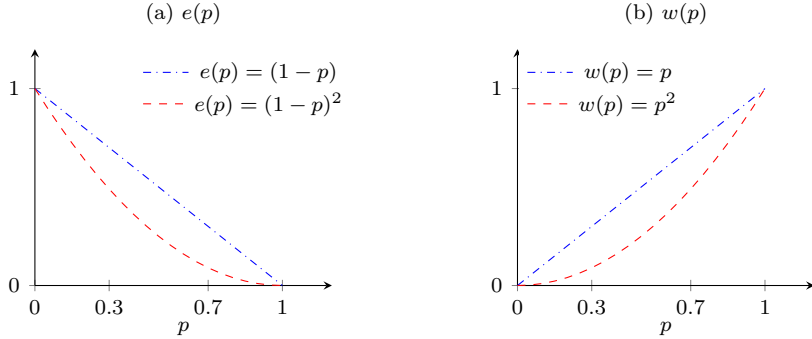
Figure 5.4: The variation of stiffness function and the local part of dissipated energy with respect to phase field function.

smooth function and it varies between 0 to 1 even in the non-crack region. In this section, we aim to understand how the phase field depends on the similarity measure, the elastic energy, the regularization parameters, and the choice of dissipation energy. Therefore, we analyze the first-order optimality condition for the proposed model (5.5) with respect to the phase field function. The investigation also illustrates the interaction between the stiffness and the toughness regularization parameters.

We investigate our proposed model (5.5) in a one-dimensional setting, *i.e.*,

$$
\mathcal{J}(f, p)
$$
$$
= \int_{\Omega} \left[s(p(x))\mathcal{S}(x, f, T, R) + \alpha e(p(x))\mathcal{E}(x, f, \nabla f(x)) + \beta w(p(x)) + \frac{1}{2}\beta l^2 p'(x)^2 \right] dx \tag{5.7}
$$

where $f : \Omega \subset \mathbb{R} \mapsto \mathbb{R}$ and $p : \Omega \subset \mathbb{R} \mapsto [0, 1]$ to be estimated.

For a fixed f, suppose the first variation of $\mathcal{J}$ at a point $\hat{p}$ vanishes in the direction $\gamma \in C_0^\infty$. This implies

$$
\delta J(\hat{p}; \gamma) = \lim_{\epsilon \to 0} \frac{J(\hat{p} + \epsilon\gamma) - J(\hat{p})}{\epsilon} = 0. \tag{5.8}
$$

The associated Euler-Lagrange equation is given by

$$
s'(\hat{p}(x))\mathcal{S}(x) + \alpha e'(\hat{p}(x))\mathcal{E}(x) + \beta w'(\hat{p}(x)) - \beta l^2 \hat{p}''(x) = 0. \tag{5.9}
$$

In order to simplify our investigation, we disregard the effect of the non-local part of dissipation energy. Therefore, we assume that the internal length parameter l is zero and the crack indicator function has a sharp transition from

the non-crack region to the crack region. We investigate the following Euler-Lagrange equation

$$s'(\hat{p}(x))\mathcal{S}(x) + \alpha e'(\hat{p}(x))\mathcal{E}(x) + \beta w'(\hat{p}(x)) = 0. \tag{5.10}$$

A material has zero elastic energy at its initial state, *i.e.*, before any deformation. If we substitute $\mathcal{E} = 0$, then (5.10) becomes

$$s'(\hat{p}(x))\mathcal{S}(x) + \beta w'(\hat{p}(x)) = 0. \tag{5.11}$$

It follows from property P2 and P4 that (5.11) is satisfied only if

$$s'(\hat{p}(x)) < 0. \tag{5.12}$$

This proves that property P5 holds.

In damage mechanics, the most common choices for dissipation energy are

DE1. $w(p) = p^2$ satisfying $w'(0) = 0$, and

DE2. $w(p) = p$ satisfying $w'(0) > 0$.

These function choices influence the behavior of the proposed NCIR model significantly as we observe this further in this section.

If a material does not have any crack region, *i.e.*, $\hat{p}(x) = 0$, then (5.10) yields

$$s'(0)\mathcal{S}(x) + \alpha e'(0)\mathcal{E}(x) + \beta w'(0) = 0. \tag{5.13}$$

Now suppose, we consider dissipation energy, defined in DE1, *i.e.*, $w(p) = p^2$ satisfying $w'(0) = 0$, then (5.13) yields

$$s'(0)\mathcal{S}(x) + \alpha e'(0)\mathcal{E}(x) = 0. \tag{5.14}$$

Following property P2 and P5, $s'(0)\mathcal{S}(x) \leq 0$, and according to property P2 and P3, we have that $\alpha e'(0)\mathcal{E}(x) \leq 0$. This concludes that

$$\mathcal{E}(x) = 0 \quad \text{and} \quad \mathcal{S}(x) = 0 \text{ at } \hat{p} = 0, \tag{5.15}$$

assuming $\alpha > 0$. $\alpha = 0$ nullifies the effect of elastic energy, and hence it is not of our interest. Equation (5.15) signifies that if the phase field is zero, the reference and the template images are in a perfect match, *i.e.*, $\mathcal{S} = 0$, without any deformation, *i.e.*, $\mathcal{E} = 0$. But, in practice, a reference and a template image are in correspondence after deformation, *i.e.*, $\mathcal{E} \geq 0$. In this case, the phase field function does not attain zero as we see in the next paragraph.

Now suppose, $s(p) = (1-p)^2$ satisfying property P5, *i.e.*, $s'(0) < 0$, $e(p) = (1-p)^2$ satisfying property P3, *i.e.*, $e'(p) < 0$, and $w(p) = p^2$ following DE1 and $w'(0) = 0$, (5.10) would be

$$-2(1-\hat{p}(x))\mathcal{S}(x) - 2\alpha(1-\hat{p}(x))\mathcal{E}(x) + 2\beta\hat{p}(x) = 0, \text{ and} \qquad (5.16)$$

$$\hat{p}(x) = \frac{1}{1 + \beta/(\mathcal{S}(x) + \alpha\mathcal{E}(x))}. \qquad (5.17)$$

The equation $\hat{p}(x) = 0$ only holds when both $\mathcal{S}(x) = 0$ and $\mathcal{E}(x) = 0$, assuming $\alpha > 0$ in the expression (5.17). We interpreted the same result through the equation (5.15).

The above analysis points out that the phase field is zero in the non-crack region only if the given template and reference image are in correspondence everywhere without any deformation. This implies that both the images are same and no need to peform registration. Otherwise, the phase field is always non-zero in the non-crack region.

As we explained before, the deformation field should be discontinuous along the crack interface. However, the proposed model (5.5) is based on the assumption that the deformation field is a continuous, a one-to-one, and an orientation-preserving function. The phase field equal to 1 corresponds to the formation/nucleation of a crack. According to the equation (5.17), the phase field value is 1 only if the system has either infinite elastic energy or infinite similarity measure, which does not satisfy the property P1, assuming regularization parameters are positive. Therefore, the proposed formulation models deformations just before the nucleation of a crack when the system has finite energy and a continuous deformation field assumption is valid.

The equation (5.17) signifies that the phase field depends on the similarity measure, the elastic energy, and the regularization parameters. We further simplify our investigation and assume that the non-crack regions are in correspondence, *i.e.*, $\mathcal{S}(x) = 0$. With this assumption, (5.17) would be

$$\hat{p}(x) = \frac{1}{1 + \beta/(\alpha\mathcal{E}(x))}. \qquad (5.18)$$

Fig. 5.5(a) illustrates the variation in the phase field function with respect to the elastic energy $\mathcal{E}$ for multiple conditions on regularization parameters, following equation (5.18). The elastic energy $\mathcal{E}$ increases with increasing deformation with respect to the initial state of a material. Fig. 5.5(a) indicates that the phase field increases with increasing deformation and approaches to 1 when deformation is significantly large, such as in the crack region. If $\beta = \alpha$, the phase field function becomes independent of the regularization parameters and solely depends on the elastic energy. This indicates that, in the proposed model, the effect of the

regularization parameters are negligible if the similarity measure is close to zero and $\beta = \alpha$. We also observe similar behaviour in our numerical experiments.

At a fixed elastic energy, according to (5.18), the phase field is approximately inversely proportional to the toughness constant β, and approximately directly proportional to the stiffness constant α. Toughness reflects the breakability and the stiffness reflects rigidity of a material. If a material is less tough, *i.e.*, easy to break, the probability of formation of a crack is higher. But, it is counterbalanced by stiffness of a material. If a material is less stiff, it is easy to stretch the material. Therefore, even the toughness is low, it would be take longer to break a stretchable material. These physical intuitions behind the toughness and stiffness help to select the regularization parameters for the registration of a given set of images.

(a) $w(p) = p^2$ (b) $w(p) = p$
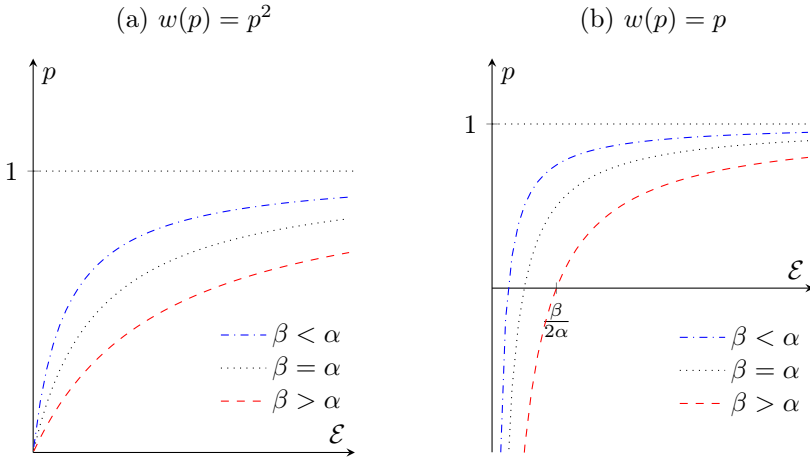
Figure 5.5: The dependence of phase field function p on the elastic energy $\mathcal{E}$ for two choices of the dissipative energy function. β is a damage toughness constant and α is a stiffness constant. $s(p) = (1-p)^2$ and $e(p) = (1-p)^2$.

Now suppose, the equation (5.13) has dissipation energy $w(p) = p$ satisfying $w'(0) > 0$, as mentioned in DE2, and following property P2 and P5, $s'(0)\mathcal{S}(x) \leq 0$ and according to property P2 and P3, $\alpha e'(0)\mathcal{E}(x) \leq 0$. This concludes that

$$s'(0)\mathcal{S}(x) + \alpha e'(0)\mathcal{E}(x) < 0, \tag{5.19}$$

assuming both $\alpha > 0$ and $\beta > 0$. If non-crack regions match perfectly, *i.e.*, $\mathcal{S}(x) = 0$, according to inequality (5.19) the elastic energy should always be positive, *i.e.*, $\mathcal{E} > 0$. Physically, this has both positive and negative implications. If the non-crack regions are in a perfect match without any deformations, the

elastic energy should be zero, but the inequality (5.19) enforces elastic energy to be positive which is an undesirable behaviour. On the other hand, if non-crack regions match perfectly after deformation, elastic energy would be non-negative; and inequality (5.19) would be satisfied and phase field function could be zero in the non-crack region, which is a desirable behavior. This behavior differs with dissipation energy $w(p) = p^2$ satisfying $w'(0) = 0$, as mentioned in DE1, where phase field attains a non-zero value in the non-crack region.

For example, if $s(p) = (1-p)^2$ satisfying $s'(0) < 0$, $e(p) = (1-p)^2$ satisfying $e'(p) < 0$, and $w(p) = p$ satisfying $w'(0) > 0$, (5.10) would be

$$-2(1-\hat{p}(x))\mathcal{S}(x) - 2\alpha(1-\hat{p}(x))\mathcal{E}(x) + \beta = 0, \text{ and} \qquad (5.20)$$

$$\hat{p}(x) = 1 - \frac{\beta}{2(\mathcal{S}(x) + \alpha\mathcal{E}(x))}. \qquad (5.21)$$

The Fig. 5.5(b) displays the variation of the phase field function (5.21) with respect to the elastic energy, assuming that the similarity measure is zero, *i.e.*, $\mathcal{S}(x) = 0$. The phase field attains a negative value, which is a physically unrealistic scenario and violates our model assumptions. We can reformulate the proposed model and explicitly constraint the phase field such that it always lies between 0 and 1. The first order optimality condition for the constraint problem still needs to be investigated.

In our numerical experiments, we use dissipation energy $w(p) = p^2$ to verify our preliminary conclusions about the behaviour of the phase field and the regularization parameters obtained through the study of first order optimality condition for the proposed model.

5.4   Discrete Image Registration Model

We can also formulate a variational registration model without any continuity assumptions on a deformation field, borrowing ideas from fracture mechanics [Francfort98]. A crack $\Gamma \subset \Omega$ is a $(d-1)-$dimensional hypersurface in a $d-$dimensional domain. If $w(x)$ represents the energy required to create an infinitesimal crack at the point x of Ω, then the surface energy associated to the crack $\Gamma \subset \Omega$ is given by

$$\int_{\Gamma} w(x)\, d\mathcal{H}^{d-1}(x) \qquad (5.22)$$

where $d\mathcal{H}^{d-1}$ is $(d-1)-$dimensional Hausdorff measure, and β represents the toughness of a material. Once again, following the principle of minimum total potential energy of the system, the variational image registration model is

expressed as

$$\underset{f,\Gamma}{\text{minimize}} \int_{\Omega \setminus \Gamma} \mathcal{S}(x,f,T,R) + \alpha \int_{\Omega \setminus \Gamma} \mathcal{E}(x,f,\nabla f(x)) + \beta \int_{\Gamma} w(x) \, d\mathcal{H}^{d-1}(x).$$
(5.23)

This model is similar to the well-known Mumford-Shah image segmentation model [Mumford89]

$$\underset{u,\Gamma}{\text{minimize}} \int_{\Omega \setminus \Gamma} |u-g|^2 + \mu \int_{\Omega \setminus \Gamma} |\nabla u|^2 + \lambda \int_{\Gamma} d\mathcal{H}^{d-1}(x).$$
(5.24)

The existence of a minimizer for the functional (5.24) has been shown through the weak formulation of the problem [De Giorgi89], i.e.,

$$\underset{u}{\text{minimize}} \int_{\Omega} |u-g|^2 + \mu|\nabla u|^2 + \lambda \mathcal{H}^{d-1}(S_u)$$
(5.25)

where S_u is the discontinuity set of u in an approximate sense, and u belongs to a special class of functions of bounded variation (SBV). The weak formulation is further approximated by elliptical functionals [Ambrosio90] through $\Gamma-$convergence theory, *i.e.*,

$$\underset{u,p}{\text{minimize}} \int_{\Omega} (1-p)^2|u-g|^2 + \mu(1-p)^2|\nabla u|^2 + \lambda\Big(\frac{p^2}{l} + \frac{1}{2}l\|\nabla p\|_2^2\Big).$$
(5.26)

The expression (5.26) is similar to our proposed model (5.5) if we choose $s(p) = (1-p)^2$, $e(p) = (1-p)^2$, and $w(p) = p^2$, *i.e.*,

$$\underset{f,p}{\text{minimize}} \int_{\Omega} (1-p)^2\mathcal{S}(x,f,T,R) + \alpha(1-p)^2\mathcal{E}(x,f,\nabla f(x)) + \beta\Big(p^2 + \frac{1}{2}l^2\|\nabla p\|_2^2\Big).$$
(5.27)

The existence analysis of the model (5.23) is still an open question but hopefully can be shown by following the ideas from [De Giorgi89]. It is possible that the elliptical approximation of weak formulation of (5.23) can be shown equivalent to our model (5.5) following the ideas from [Ambrosio90] and work done in the field of mechanics [Henao10; Henao15], however, this still needs to be investigated rigorously.

5.5   Image Registration Model for Images with Missing Structures

We are now concerned with a situation when some regions of a reference image do not match with any region in a template image. We refer to these regions as non-corresponding regions. The similarity measure computes the similarity between

two images based on the features of interest and it attains a high value in the non-corresponding regions. This observation has motivated a number of authors [Brett01; Periaswamy06; Ou11; Drobny15] to propose a locally-weighted image registration model. The weight function depends on the similarity measure and assigns a lower weight to the non-corresponding regions. A general image registration model is expressed as

$$\underset{f}{\text{minimize}} \int_\Omega w(x, f, T, R) \, \mathcal{S}(x, f, T, R) + \alpha \int_\Omega \mathcal{E}(x, f, \nabla f(x)). \qquad (5.28)$$

One of the common choices for the weight function $w(x, f, T, R)$ [Drobny15] is

$$w(x, f, T, R) = \exp(-S(x, f, T, R)^2/\sigma) \qquad (5.29)$$

where σ is a regularization parameter which controls the area of the corresponding regions.

Another approach to solving the problem is a joint segmentation and registration approach [Chitphakdithai10; Kwon14; Chen15; Richard04] where a regularization energy term is introduced to penalize the area of non-corresponding regions. On a similar note, we are proposing a generalized model for the problem. The model proposed by [Richard04] can be considered as a special case of our proposed model.

We assume that the driving force acting on corresponding regions majorly guides the image registration process. Therefore, similarity measure mainly works on the corresponding regions by masking the non-corresponding regions by means of a phase field function. This function varies between 0 to 1 and attains values close to 1 in the non-corresponding regions. We introduce an energy term which represents the work done on the non-corresponding regions in terms of the phase-field function. Therefore, the total energy of the system is given by

$$\mathcal{J}(f, p) = \int_\Omega s(p(x))\mathcal{S}(x, f, T, R) + \alpha\mathcal{E}(x, f, \nabla f(x)) + \beta\mathcal{D}(p(x)), \qquad (5.30)$$

and the image registration model following the minimum total potential energy principle is defined as

$$\underset{f,p}{\text{minimize}} \, \mathcal{J}(f, p). \qquad (5.31)$$

The model (5.31) is similar to the model (5.5) assuming $e(p) = 1$. Therefore, most of the analysis done for (5.5) can readily be extended for (5.31).

Notice that both the models (5.31) and (5.28) estimate smooth deformation fields in non-corresponding regions, but they are majorly guided by nearby corresponding regions. We want to show the connection between these two models

by specifying $s(p) = (1 - p)^2$, and $\mathcal{D}(p) = p^2$ in the energy functional (5.30), *i.e.*,

$$\mathcal{J}(f, p) = \int_\Omega (1 - p(x))^2 \mathcal{S}(x, f, T, R) + \alpha \mathcal{E}(x, f, \nabla f(x)) + \beta p^2(x). \qquad (5.32)$$

Suppose, the first variation of $\mathcal{J}$ with respect to $\hat{p}$ vanishes in all directions $\gamma \in \mathcal{C}_0^\infty$. This implies,

$$\delta J(\hat{p}; \gamma) = 0. \qquad (5.33)$$

The associated Euler-Lagrangian equation is

$$-2(1 - \hat{p}(x))\mathcal{S}(x, f, T, R) + 2\beta\hat{p}(x) = 0. \qquad (5.34)$$

This implies

$$\hat{p}(x) = \frac{\mathcal{S}}{\mathcal{S} + \beta}. \qquad (5.35)$$

After substituting the optimal $\hat{p}(x)$ in (5.32), the model becomes

$$\underset{f}{\text{minimize}} \int_\Omega \frac{\beta}{\mathcal{S}(x, f, T, R) + \beta} \mathcal{S}(x, f, T, R) + \alpha \mathcal{E}(x, f, \nabla f(x)), \qquad (5.36)$$

which is similar to the weighted image registration model (5.28) with weight function

$$w(x, f, T, R) = \frac{\beta}{\mathcal{S}(x, f, T, R) + \beta}. \qquad (5.37)$$

The weight functions (5.29) and (5.37) are illustrated in Fig. 5.6.
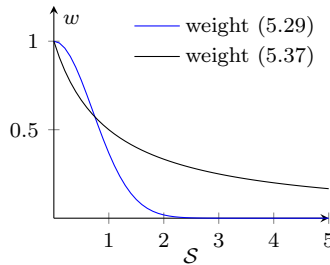
Figure 5.6: Illustration of weight functions (5.29) and (5.37) at $\sigma = 1$, and $\beta = 1$.

5.6 Numerical Implementation

We discretize the variational problem (5.5) to compute a numerical solution. We use the Galerkin finite element method (FEM) to approximate $f \in \mathcal{V}$ from a finite-dimensional subspace $\mathcal{V}_h \subset \mathcal{V}$. The presentation of discretization scheme in this work is motivated by the work of Ruthotto *et al.* [Ruthotto15].

5.6.1 Galerkin Finite Element Method Discretization

The two-dimensional domain is triangulated with a total of n_t triangles $\mathcal{T}_h$ where h is the mesh size, the maximum diameter of a triangle. Let $\mathcal{V}_h$ be a finite-dimensional subspace of piecewise linear functions with basis $b_1, b_2, \ldots, b_{n_v}$: $\Omega \mapsto \mathbb{R}$, where n_v is the total number of vertices in the mesh. The vertices of triangles are denoted by $V_1, V_2, \ldots, V_{n_v}$. The continuous function $f = (f_1, f_2)$ is represented in terms of basis functions as

$$f(x) = \sum_{i=1}^{n_v} \mathrm{f}_i \ b_i(x) \tag{5.38}$$

where coefficients f are stored component-wise in a column vector $\mathbf{f} = (\mathbf{f}_1, \mathbf{f}_2)^T \in \mathbb{R}^{2n_v}$. Similarly, the function p is expressed in terms of linear basis functions as

$$p(x) = \sum_{i=1}^{n_v} \mathrm{p}_i \ b_i(x) \tag{5.39}$$

where coefficients p are stored component-wise in a column vector $\mathbf{p} \in \mathbb{R}^{n_v}$.

The partial derivatives $\nabla = (\partial_1, \partial_2)$ of p are given by

$$\nabla p(x) = \sum_{i=1}^{n_v} \mathrm{p}_i \ \nabla b_i(x). \tag{5.40}$$

The partial derivative of a linear basis function is piecewise constant all over the triangle. The partial derivatives are stored in a column vector $\mathbf{Jp} \in \mathbb{R}^{2n_t}$ where $\mathbf{J} \in \mathbb{R}^{2n_t \times n_v}$ is a partial derivative operator formed with a partial derivative of basis functions. The Jacobian matrix $\nabla f(x)$ is also stored in a column vector $\mathbf{Df} \in \mathbb{R}^{4n_t}$ where $\mathbf{D} \in \mathbb{R}^{4n_t \times 2n_v}$ is defined as

$$\mathbf{D} = I_2 \otimes \mathbf{J}. \tag{5.41}$$

We use midpoint quadrature rule to compute the numerical integration of our objective functional. The first integral in (5.5) is approximated as

$$\int_{\Omega} s(p(x))\, \mathcal{S}(x, f, T, R) = \sum_{i=1}^{n_t} \int_{(\mathcal{T}_h)_i} s(p(x))\, \mathcal{S}(x, f, T, R) \tag{5.42}$$

$$\approx \sum_{i=1}^{n_t} \text{Area}((\mathcal{T}_h)_i)\, s(p(x_m))\, \mathcal{S}(x_m, f, T, R) \tag{5.43}$$

where x_m is the centroid of a triangle $\mathcal{T}_h$. Similarly, we approximate other integrals of (5.5).

Let $\mathbf{A} \in \mathbb{R}^{n_t \times n_v}$ be an averaging matrix on the centroid of a triangle, defined as,

$$\mathbf{A}_{i,j} = \begin{cases} 1/3 & \text{if } V_j \text{ is node of } (\mathcal{T}_h)_i \\ 0 & \text{otherwise.} \end{cases} \tag{5.44}$$

Another averaging matrix $\mathbf{B} \in \mathbb{R}^{2n_t \times 2n_v}$ is defined as

$$\mathbf{B} = I_2 \otimes \mathbf{A}, \tag{5.45}$$

and $\mathbf{v} \in \mathbb{R}^{n_t}$ stores area of triangles, and we define $\mathbf{V} = \text{diag}(\mathbf{v})$.

For illustration, if we assume that the similarity measure is a intensity preserving sum of squared differences, *i.e.*,

$$S(x, f, T, R) = \frac{1}{2}\Big(T(f(x)) - R(x)\Big)^2, \tag{5.46}$$

the first integral in (5.5), in its discrete form, utilizing (5.43), is represented as

$$\mathrm{S}[\mathbf{f}, \mathbf{p}] = \frac{1}{2}\text{res}(\mathbf{f})^T \text{diag}(s(\mathbf{Ap}) \odot \mathbf{v})\text{res}(\mathbf{f}) \tag{5.47}$$

where $\text{res}(\mathbf{f}) = T(\mathbf{Bf}) - R(\mathbf{x})$.

The discrete partial derivatives of the functional $\mathrm{S}[\mathbf{f}, \mathbf{p}]$ are

$$\partial_{\mathbf{f}}\mathrm{S} = \text{res}(\mathbf{f})^T \text{diag}(s(\mathbf{Ap}) \odot \mathbf{v})\nabla T(\mathbf{Bf})\mathbf{B}, \tag{5.48}$$

$$\partial_{\mathbf{p}}\mathrm{S} = \frac{1}{2}(\text{res}(\mathbf{f}) \odot \text{res}(\mathbf{f}) \odot \mathbf{v})^T\, \text{diag}(s'(\mathbf{Ap}))\mathbf{A}, \tag{5.49}$$

$$\partial_{\mathbf{f}}^2\mathrm{S} \approx \mathbf{B}^T(\nabla T(\mathbf{Bf}))^T \text{diag}(s(\mathbf{Ap}) \odot \mathbf{v})\nabla T(\mathbf{Bf})\mathbf{B}, \tag{5.50}$$

$$\partial_{\mathbf{p}}^2\mathrm{S} = \frac{1}{2}\mathbf{A}^T \text{diag}(\text{res}(\mathbf{f}) \odot \text{res}(\mathbf{f}) \odot \mathbf{v})\, \text{diag}(s''(\mathbf{Ap}))\mathbf{A}, \tag{5.51}$$

$$\partial_{\mathbf{pf}}\mathrm{S} = \mathbf{A}^T \text{diag}(\text{res}(\mathbf{f}) \odot s'(\mathbf{Ap}) \odot \mathbf{v})\nabla T(\mathbf{Bf})\mathbf{B}. \tag{5.52}$$

Similarly, if the choice of elastic energy is the hyperelastic regularization energy [Ruthotto15], *i.e.*,

$$\mathcal{E}(x, f, \nabla f(x)) = \frac{1}{2}\alpha_l \|\nabla(f - f_{\text{ref}})\|_2^2 + \alpha_v \psi(\det(\nabla f(x))) \tag{5.53}$$

where $\psi(v) = (v-1)^4/v^2$, the second integral in (5.5) is represented in its discrete form as

$$\begin{aligned}
\mathrm{E}[\mathbf{f}, \mathbf{p}] &= \alpha \mathrm{E}^l[\mathbf{f}, \mathbf{p}] + \alpha \mathrm{E}^v[\mathbf{f}, \mathbf{p}], \\
&= \frac{\alpha\alpha_l}{2}(\mathbf{f} - \mathbf{f}_{\text{ref}})^T \mathbf{D}^T[I_4 \otimes (e(\mathbf{Ap}) \odot \mathbf{v})]\mathbf{D}(\mathbf{f} - \mathbf{f}_{\text{ref}}) + \tag{5.54}
\end{aligned}$$

$$\alpha\alpha_v(e(\mathbf{Ap}) \odot \mathbf{v})^T \psi(\det \mathbf{Df}). \tag{5.55}$$

The discrete partial derivatives are

$$\partial_{\mathbf{f}}\mathrm{E}^l = \alpha_l(\mathbf{f} - \mathbf{f}_{\text{ref}})^T\mathbf{D}^T[I_4 \otimes (e(\mathbf{Ap}) \odot \mathbf{v})]\mathbf{D}, \tag{5.56}$$

$$\partial_{\mathbf{p}}\mathrm{E}^l = \frac{\alpha_l}{2}[\mathbf{D}(\mathbf{f} - \mathbf{f}_{\text{ref}}) \odot (I_4 \otimes \mathbf{v}) \odot \mathbf{D}(\mathbf{f} - \mathbf{f}_{\text{ref}})]^T(\mathbf{1}_4 \otimes e'(\mathbf{Ap}))\mathbf{A}, \tag{5.57}$$

$$\partial_{\mathbf{f}}^2\mathrm{E}^l = \alpha_l\mathbf{D}^T[I_4 \otimes (e(\mathbf{Ap}) \odot \mathbf{v})]\mathbf{D}, \tag{5.58}$$

$$\partial_{\mathbf{p}}^2\mathrm{E}^l = \frac{\alpha_l}{2}\mathbf{A}^T(\mathbf{1}_4 \otimes I_{n_t})^T\mathrm{diag}(\mathbf{D}(\mathbf{f} - \mathbf{f}_{\text{ref}}) \odot (I_4 \otimes \mathbf{v}) \odot \mathbf{D}(\mathbf{f} - \mathbf{f}_{\text{ref}}))$$
$$(\mathbf{1}_4 \otimes I_{n_t})\,\mathrm{diag}(e''(\mathbf{Ap}))\mathbf{A}, \tag{5.59}$$

$$\partial_{\mathbf{pf}}\mathrm{E}^l = \alpha_l\mathbf{A}^T\mathrm{diag}(e'(\mathbf{Ap}) \odot \mathbf{v})(\mathbf{1}_4 \otimes I_{n_t})\mathrm{diag}(\mathbf{D}(\mathbf{f} - \mathbf{f}_{\text{ref}}))\mathbf{D}, \tag{5.60}$$

and,

$$\partial_{\mathbf{f}}\mathrm{E}^v = \alpha_v(e(\mathbf{Ap}) \odot \mathbf{v})^T\psi'(\det \mathbf{Df})\,d\det \mathbf{Df}, \tag{5.61}$$

$$\partial_{\mathbf{p}}\mathrm{E}^v = \alpha_v(\psi(\det \mathbf{Df}) \odot \mathbf{v})^T\mathrm{diag}(e'(\mathbf{Ap}))\mathbf{A}, \tag{5.62}$$

$$\partial_{\mathbf{f}}^2\mathrm{E}^v \approx \alpha_v(d\det \mathbf{Df})^T\mathrm{diag}(e(\mathbf{Ap}) \odot \mathbf{v} \odot \psi''(\det \mathbf{Df}))\,d\det \mathbf{Df}, \tag{5.63}$$

$$\partial_{\mathbf{p}}^2\mathrm{E}^v = \alpha_v\mathbf{A}^T\mathrm{diag}(\psi(\det \mathbf{Df}) \odot \mathbf{v} \odot e''(\mathbf{Ap}))\mathbf{A}, \tag{5.64}$$

$$\partial_{\mathbf{pf}}\mathrm{E}^v = \alpha_l\mathbf{A}^T\mathrm{diag}(e'(\mathbf{Ap}) \odot \mathbf{v} \odot \psi'(\det \mathbf{Df}))\,d\det \mathbf{Df}. \tag{5.65}$$

If we consider dissipated energy, *i.e.*,

$$\mathcal{D}(p(x)) = w(x) + \frac{1}{2}l^2\|\nabla p\|_2^2, \tag{5.66}$$

the third integral in (5.5), in its discrete form, is expressed as

$$\mathrm{D}[\mathbf{p}] = \beta\left(\mathbf{v}^T w(\mathbf{Ap}) + \frac{1}{2}l^2\mathbf{p}^T\mathbf{J}^T\mathrm{diag}(\mathbf{1}_2 \otimes \mathbf{v})\mathbf{Jp}\right). \tag{5.67}$$

The discrete partial derivatives are

$$\partial_{\mathbf{p}} D = \beta \Big(\mathbf{v}^T \mathrm{diag}(w'(\mathbf{A}\mathbf{p}))\mathbf{A} + l^2 \mathbf{p}^T \mathbf{J}^T \mathrm{diag}(\mathbf{1}_2 \otimes \mathbf{v})\mathbf{J} \Big), \qquad (5.68)$$

$$\partial_{\mathbf{p}}^2 D = \beta \Big(\mathbf{A}^T \mathrm{diag}(\mathbf{v} \odot w''(\mathbf{A}\mathbf{p}))\mathbf{A} + l^2 \mathbf{J}^T \mathrm{diag}(\mathbf{1}_2 \otimes \mathbf{v})\mathbf{J} \Big). \qquad (5.69)$$

To summarize, the discretized objective functional of (5.5) is expressed as

$$J[\mathbf{f}, \mathbf{p}] = S[\mathbf{f}, \mathbf{p}] + E[\mathbf{f}, \mathbf{p}] + D[\mathbf{p}]. \qquad (5.70)$$

5.6.2 Multi-level Optimization and Initialization

In this work, we apply the Gauss-Newton (GN) optimization algorithm to locally minimize the energy function (5.70). Image registration functionals are highly non-convex in general. Therefore, an initial estimate plays an important role in an iterative method to converge to a desirable local optimal point. In a multilevel approach, an optimal point computed at a coarse discretization is the starting point of an iterative algorithm at a finer discretization of the domain. It is assumed that the optimal point at a coarse discretization is close to a global minimum or a desired local minimum. Therefore, the optimization problem at a finer discretization converges faster to a local optimal point. In practice, this strategy works efficiently to estimate a desirable solution.

The GN algorithm approximates a local curvature information to estimate an update step $\mathrm{du} = [\mathrm{df}; \mathrm{dp}]$ by solving a linear system, *i.e.*,

$$\mathrm{H}\,\mathrm{du} = -\mathrm{dJ} \qquad (5.71)$$

where H is an approximated positive definite Hessian matrix. We approximate the Hessian matrix as

$$\mathrm{H} = \begin{bmatrix} \partial_{\mathbf{f}}^2 S + \partial_{\mathbf{f}}^2 E & 0 \\ 0 & \partial_{\mathbf{p}}^2 S + \partial_{\mathbf{p}}^2 E + \partial_{\mathbf{p}}^2 D \end{bmatrix}, \qquad (5.72)$$

and ensure positive definitness of the matrix by choosing functions such that

$$s''(p) \geq 0, \quad e''(p) \geq 0, \quad \text{and} \quad w''(p) \geq 0, \quad \forall p. \qquad (5.73)$$

Given a starting point $\mathrm{u}^{(0)} = [\mathrm{f}^{(0)}; 0]$, where $\mathrm{f}^{(0)}$ is the initial configuration of the discretization grid; the algorithm estimates the next step

$$\mathrm{u}^{(k)} = \mathrm{u}^{(k-1)} + \lambda \mathrm{du}, \qquad (5.74)$$

where λ is the step size computed using the Armijo line search algorithm. We refer to [Modersitzki09] for a detailed description of the optimization procedure, stopping criteria, etc., in the context of image registration.

5.7 Experiments and Results

We demonstrate the potential of our proposed model using academic examples as shown in Fig. 5.7 and Fig. 5.13, for which the deformation fields can be expressed analytically. This allows us to compute error measures numerically and evaluate the accuracy of the registration. However, the analytical deformation field is not a unique solution for the chosen images, but this is one of the physically desirable solution.

We are using model (5.5) with $s(p) = (1-p)^2$, $e(p) = (1-p)^2 + \eta$, and $w(p) = p^2$. These function choices are based on our analysis of first order optimality condition of the energy functional with respect to p in section 5.3. The stiffness function might reduce to zero in the crack zone, which can completely distort the regularity of the deformation fields. Therefore, a small constant $\eta = 10^{-7}$ is added to regularize the deformation field in the crack region. We used Hyperelastic regularization energy with parameters $\alpha_l = 1$ and $\alpha_v = 1$.

Digital images are discrete data because intensities are known only on a set of grid points. On the other hand, image functions T and R in the registration model are assumed to be continuous and defined all over the spatial domain. Therefore, we define a continuous image model represented by a regularized spline basis functions. We use a built-in functionality of the FAIR toolbox to define a spline image model where bending energy is a choice of regularizer with a smoothing parameter $\theta = 4 \times 10^{-2}$. In this work, we are extensively using built-in functions of the FAIR toolbox [Modersitzki09], and its add-on FAIRFEM [Ruthotto15], unless stated otherwise.

We discretize the objective functional at five levels and optimize it sequentially at each level. The solution at a coarse level serves as an initial guess at a finer level. The estimated functions at a coarse grid are prolongated using linear polynomial basis functions. The image size is 128×128 pixels with a domain size of 2×2 units. However, we display results at the third discretization level, i.e., 32×32 pixels, due to a clear visualization of the deformation field.

We compare the correspondence map f_n, estimated from the proposed NCIR model (5.5), and f_c, estimated from the CIR model (5.1), with the analytical solution $\hat{f}$. We report the percent deformation field error,

$$e_{\hat{f}}(f) = 100 \times \frac{||f - \hat{f}||_2}{||\hat{f}||_2}, \tag{5.75}$$

to compare the accuracy of deformation fields. Instead of computing the error measure for the full domain, we calculate the deformation field error only for

the particles on the foreground object. The internal length l is zero in all experiments unless explicitly stated otherwise. We choose regularization parameters in all experiments based on the smallest percent error.

5.7.1   Intensity-preserving Registration
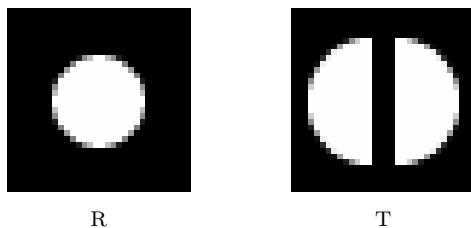
Figure 5.7: Intensity preserved images R and T for image registration. The display range for images is 0 to 1.

The appropriate similarity measure for the academic example, as shown in Fig. 5.7, is the intensity preserving SSD because the intensity of reference and template images are same. The intensity preserving SSD similarity measure is

$$\mathcal{S}(x, f, T, R) = \frac{1}{2}\Big(T(f(x)) - R(x)\Big)^2. \tag{5.76}$$

Fig. 5.8 shows the reference and the template image, deformed template images, a grid visualization of the deformation field overlaid on the template image, and a phase field map. In this example, the object expands and breaks into two parts. Therefore, the analytical forward map $\hat{f} : \Omega_R \subset \mathbb{R}^2 \mapsto \Omega_T \subset \mathbb{R}^2$ is given by

$$\hat{f}_1(x_1, x_2) = \begin{cases} cx_1 + d & x_1 > 0 \\ cx_1 - d & x_1 < 0 \\ 0 & x_1 = 0 \end{cases}, \quad \hat{f}_2(x_1, x_2) = cx_2, \tag{5.77}$$

where c is a scaling constant, $2d$ is the width of the crack in the image T, and the center of the coordinate system lies at the center of an image.

The deformed template images $T(f_c)$ and $T(f_n)$ are quite similar to the reference image with minor differences around the crack zone. However, we can notice substantial variations in the deformation fields around the crack zone with respect to the analytical solution. Therefore, an error measure only based on the similarity between a reference and a deformed template image may not

Reference (R) $T(f_c)$ T and $\hat{f}$ T and f_c

$e_{\hat{f}}(f_c) = 7.94\%$

Template (T) $T(f_n)$ p T and f_n

$e_{\hat{f}}(f_n) = 2.52\%$
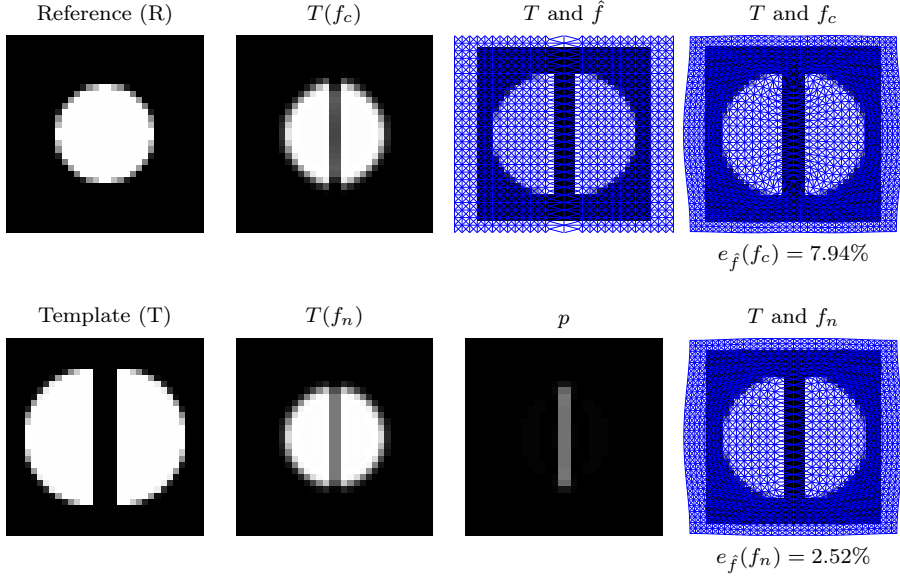
Figure 5.8: Forward maps and registered images based on an academic example. The regularization parameter $\alpha = 2 \times 10^3$ for CIR model, and $(\alpha, \beta) = (700, 2 \times 10^4)$ for NCIR model. The display range for images is [0,1].

be good enough to evaluate the performance of the image registration model. The accuracy of the deformation field is equally important. Unfortunately, the ground truth deformation field is not known for almost all real-world applications, hence error measure based on the deformation field can not be used.

The NCIR model estimates deformation field f_n with percent error 2.52% while CIR model estimate f_c with a percent error of 7.94%. The background intensity of the reference image is same as the intensity of the cracked zone in the template image. It is possible that particles on the background region in the reference image might map to particles lies in the cracked zone in the template image. This is what we observe in the grid representation of f_c at the top and bottom corner of the cracked zone. On the other hand, using the NCIR model, the phase field function identifies the crack region accurately in the reference image. Consequently, the phase field reduces the stiffness along the crack region, and allows large deformations. Moreover, the phase field masks the crack region such that the similarity measure mainly act in the non-crack region. Consequently, the particles lies in the non-crack region are not influenced much by the large deformations in the nearby crack region.

Above all, the deformation fields in the background region differs a lot from the analytical solution. The background does not contain enough textural information, and driving forces are almost inactive in that region. Therefore, surrounding regions around the foreground object are mainly driven by deformations in the foreground object.

We now emphasize the limitation of the CIR model by interchanging the role of template and reference image and estimating a backward deformation field. Now, physically, two objects are shrunk and glued together. The analytical expression for the backward map $\hat{g} : \Omega_T \mapsto \Omega_R$ is given by

$$\hat{g}_1(x_1, x_2) = \begin{cases} \frac{1}{c}x_1 - d & x_1 > d \\ \frac{1}{c}x_1 + d & x_1 < -d \\ 0 & -d \leq x_1 \leq d \end{cases}, \quad \hat{g}_2(x_1, x_2) = \frac{1}{c}x_2. \quad (5.78)$$

$$e_{\hat{f}}(g_c) = 36.96\%$$

$$e_{\hat{g}}(g_n) = 6.04\%$$

Figure 5.9: Backward maps and registered images based on an academic example. The regularization parameter $\alpha = 10^4$ for the CIR model, and $(\alpha, \beta) = (24, 24)$ for the NCIR model. The display range for images is [0,1].

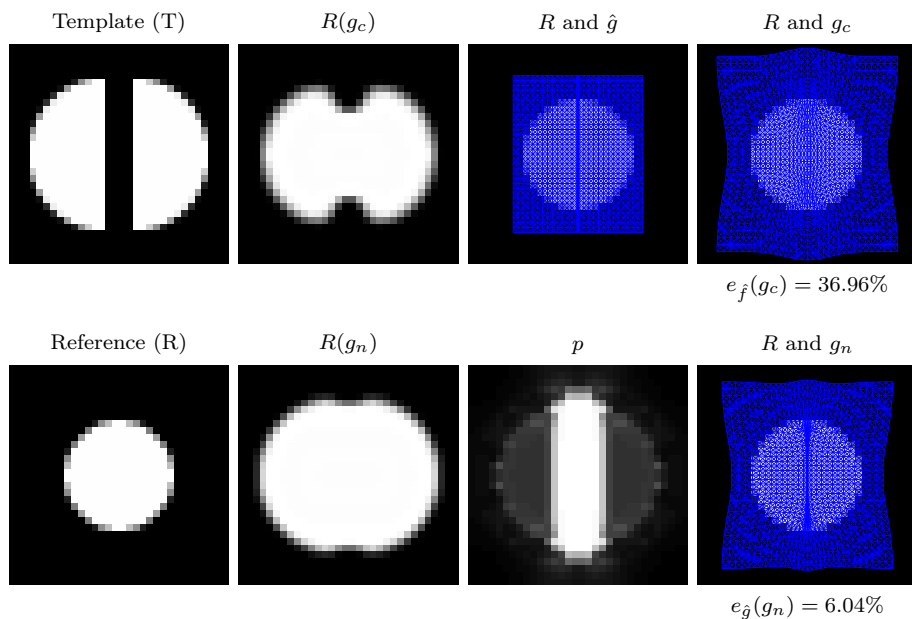One of the primary concerns is the mapping of particles lying on the crack zone in the image T, shown in Fig. 5.9. The CIR model, due to its basic assumption of correspondence everywhere, establishes a mapping with the background

particles on the image R. That is why the grid g_c bends towards the top and bottom of the image in the very center of the image. The backward map g_c has a percent error of 36.96%. On the other hand, the phase field masks the crack region in the image T and reduces its influence in the non-crack region. Moreover, lower stiffness allows a large volume shrinkage in the crack region. The g_n grid moves towards the center of the image following the path of nearby regions, and achieves a percent error of 6.04%.

The deformed image $R(g_c)$ is quite different from the image T. However, the deformed image $R(g_n)$ is dissimilar to image T majorly in the crack zone due to a continuous spline function used to interpolate the image R at g_n.

5.7.2   Study of Regularization Parameters
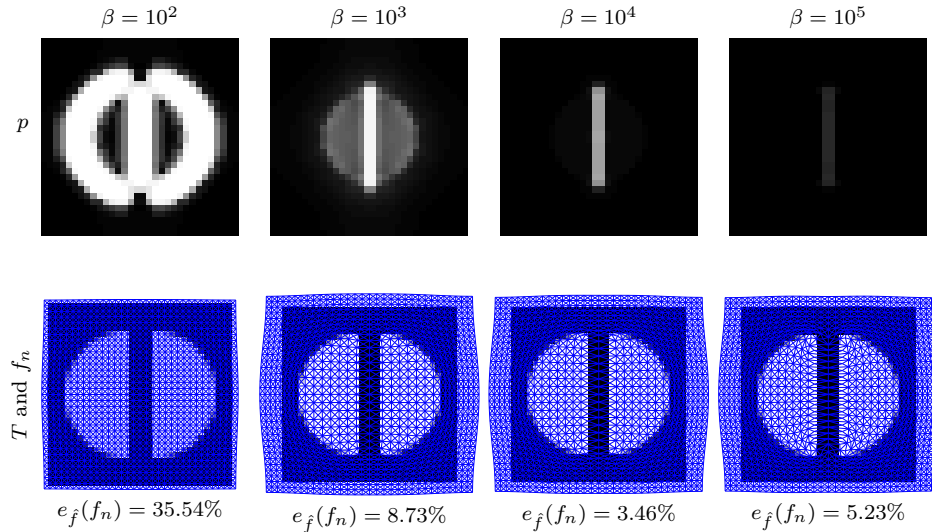
Figure 5.10: Phase field functions and deformation fields with a fixed stiffness and varying toughness parameters. The display range for phase field function p is 0 to 1.

The regularization parameters are crucial factors to decide the efficacy of variational models. In the NCIR model, we mainly tune two regularization parameters, *i.e.*, a stiffness constant α, and a toughness constant β. In this section, we perform experiments using the intensity-preserving images as shown in Fig. 5.7.

Fig. 5.10 displays variation in the phase field and the deformation field with a

fixed stiffness and varying toughness parameter. Following the equation (5.17), the optimal phase field $\hat{p}$ is inversely proportional to the toughness parameter, and approximately directly proportional to the sum of the similarity measure and the elastic energy. If the toughness parameter is low, the phase field attains a high value. Therefore, as a general observation in Fig. 5.10, the phase field is decreasing as the toughness parameter is increasing. Physically, toughness reflects breakability of a material. As toughness is increasing, the material becomes harder to break, and the possibility of a damage is lower. Therefore, the phase field, which reflects the damage in the material, also decreases with increasing toughness. At a very high toughness, the phase field approaches to zero, and the NCIR model behaves similarly to the CIR model.

During the initial iterates of the optimization problem associated with the NCIR model, the similarity measure is usually high due to the non-correspondences between the given images. If the similarity measure is quite high and the toughness parameter is low, the phase field would attain a high value. Consequently, the phase field masks the regions wherever the similarity measure is high. In turn, the driving forces become inactive in that region, and optimization process stops early. That's why, in Fig. 5.10, the phase field is high in the non-crack regions as well as in the crack region due to low toughness parameter. In other words, the NCIR model can consider the non-crack region as a crack region if the toughness parameter is too low.
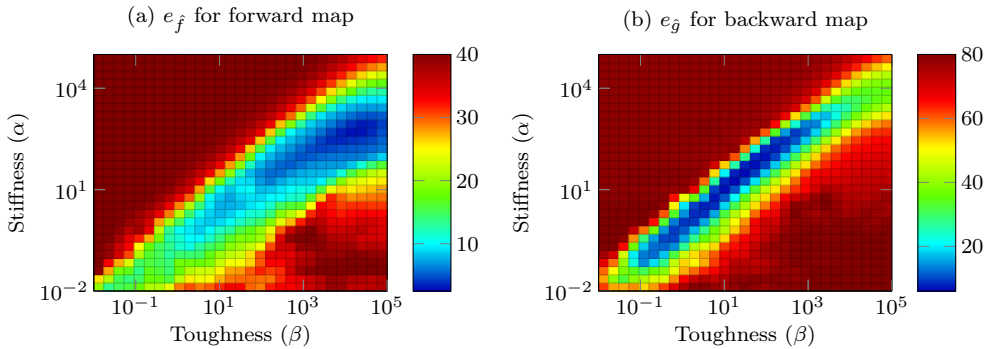
Figure 5.11: Error plot for forward and backward map.

The error plots, shown in Fig. 5.11, demonstrate the sensitivity of the NCIR model with respect to the regularization parameters. At a fixed stiffness, we observe a safe zone where the forward map percent error is small and varies approximately 5% for a range of toughness parameters, as can be seen from Fig. 5.11(a) and Fig. 5.10. Moreover, there is a sharp transition in the percent error at the boundary of the safe zone. The percent error is small mostly when $\beta \geq \alpha$, which can be used as a basic guideline to choose regularization

parameters for the NCIR model.

The safe zone for the backward map is quite narrow and it has steep transitions at a fixed stiffness parameter, as shown in Fig. 5.11(b). However, there are a number of (α, β) pairs where the percent error is small, but mostly concentrated around $\alpha = \beta$. Therefore, a starting parameter choice to estimate the backward map could be $\alpha = \beta$.

The parameter choice may also depend on the width of the crack and other features in the image. Moreover, the parameter choice may become difficult if the opening and closing of a fracture happen simultaneously in a reference image. In this case, as per our observations, $\alpha = \beta$ could be a starting parameter choice.

5.7.3 Internal Length Analysis
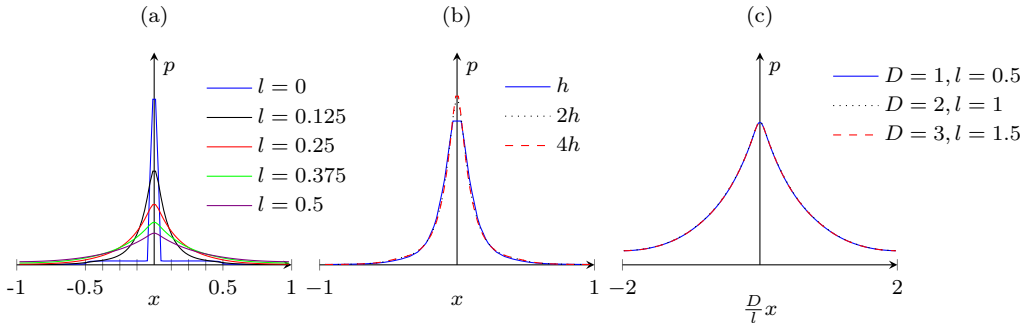
Figure 5.12: Internal length analysis. (a) Phase field variation with internal length. (b) Illustrate mesh size effect on the phase field at internal length l=0.125. (c) Interdependency of internal length and domain size (-D,D) where $x \in (-1, 1)$.

The internal length is a physical scalar, which has been introduced in the NCIR model to satisfy the dimensions of the energy functional. The internal length controls contributions from the non-local dissipation energy that penalizes jumps in the phase field function. A zero internal length nullifies the effect of non-local energy, and hence phase field function may consist of a set of jumps. In all of our numerical experiments (except this section), the internal length is zero and we observed satisfactory registration results. We do not know the exact use of the jump penalization term in the perspective of image registration yet.

Nevertheless, it is worthwhile to investigate the effect of the internal length on the image registration. The internal length is a physical quantity, and hence

this should not depend on the discretization, *i.e.*, the mesh size. However, the internal length depends on the domain size of the image with a constant factor. In this section, we illustrate our findings through numerical experiments.

We perform experiments on the images as shown in Fig. 5.7. We fix the regularization parameters $(\alpha, \beta) = (600, 2 \times 10^4)$. The domain size is 2×2 square unit. Fig. 5.12(a) displays a one-dimensional horizontal cross-section of the phase field function at multiple values of the internal length. The phase field is large at $x = 0$, the location of the crack interface. It appears that the phase field becomes smoother with increasing internal length, but the area under the curve is approximately the same for all line profiles, *i.e.*, around 0.1, except for zero internal length. The diffusivity of phase field affects the accuracy of deformation field estimate. Therefore, zero internal length seems to be the best candidate to approximate a precise phase field.

Fig. 5.12(b) displays the phase field line profiles at different mesh sizes for a fixed internal length, *i.e.*, $l = 0.125$. All line profiles are overlapping on each other which verifies that the internal length is independent of domain discretization resolution. Fig. 5.12(c) displays the phase field line profiles with varying domain size and internal length. The line profiles are similar if the internal length varies in a fixed proportion to the size of the domain.

5.7.4   Mass-preserving Registration

<p align="center">R   T</p>
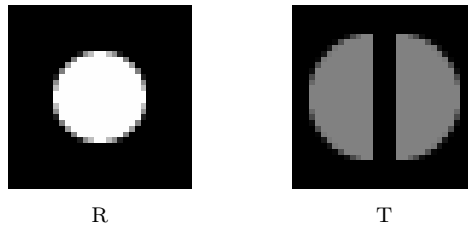
Figure 5.13: Mass preserved images R and T for image registration. The display range for images is 0 to 1.

Our next academic example, as shown in Fig. 5.13, represents a mass-preserving application where the total mass of an object remains preserved during the deformation. Like our previous examples, the object, represented in the image R, breaks into two parts during stretching, but the density of the object reduces proportional to its stretching factor to preserve the total mass of the object. That is why the intensity of the template image is low. The suitable similarity

measure for a mass-preserving application is

$$S(x, f, T, R) = \frac{1}{2}\Big(T(f(x))\det(\nabla f(x)) - R(x)\Big)^2, \tag{5.79}$$

where the determinant of the Jacobian, $\det(\nabla f(x))$, measures the local change in volume.

The analytical forward map $\hat{f}$ and backward map $\hat{g}$ for the mass-preserving example is identical to the intensity preserving example, as defined in (5.77) and (5.78) respectively. Fig. 5.14 and Fig. 5.15 display registered images, deformation fields, and a phase field. The intensity of the deformed template image is similar to the reference image which verifies the potential of the mass-preserving similarity measure. Surprisingly, the NCIR model behaviour for this mass-preserving example is similar to the behaviour for intensity-preserving example. We do not recognize any substantial influence of mass-preservation on the deformation field estimate.

Reference (R) $T(f_c)\det(\nabla f_c)$ T and $\hat{f}$ T and f_c

$e_{\hat{f}}(f_c) = 8.27\%$

Template (T) $T(f_n)\det(\nabla f_n)$ p T and f_n

$e_{\hat{f}}(f_n) = 1.84\%$
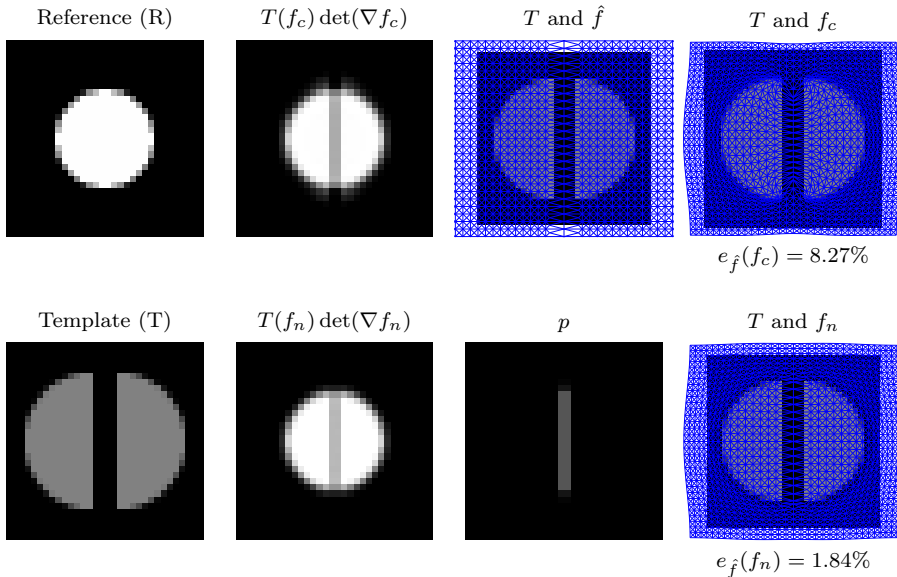
Figure 5.14: Forward maps and registered images based on the mass-preserving example. The regularization parameter $\alpha = 700$ for CIR model, and $(\alpha, \beta) = (40, 3500)$ for the NCIR model. The display range for images is [0,1].

| Template (T) | $R(g_c)\det(\nabla g_c)$ | R and $\hat{g}$ | R and g_c |

$$e_{\hat{g}}(g_c) = 30.38\%$$

| Reference (R) | $R(g_n)\det(\nabla g_n)$ | p | R and g_n |

$$e_{\hat{g}}(g_n) = 10.98\%$$
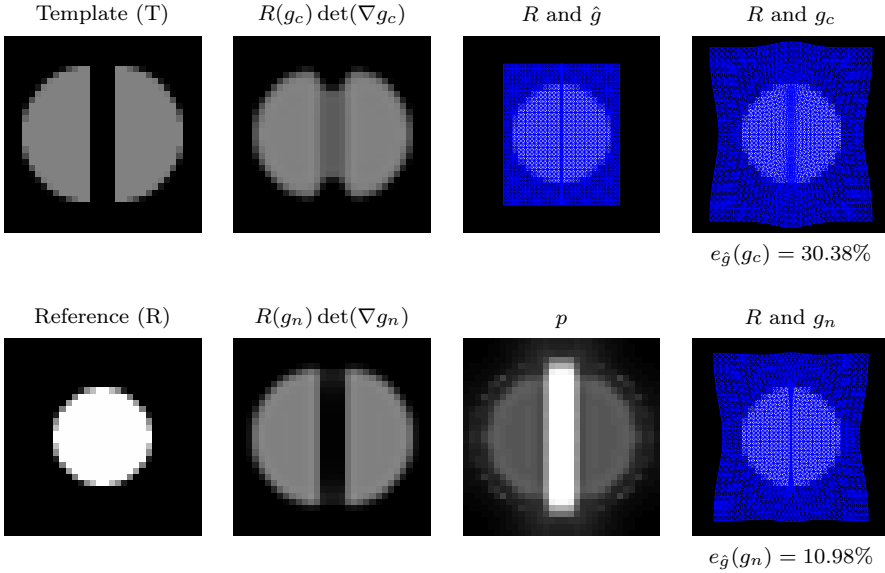
Figure 5.15: Backward maps and registered images based on the mass-preserving academic example. The regularization parameter $\alpha = 2 \times 10^3$ for CIR model, and $(\alpha, \beta) = (24, 14)$ for NCIR model. The display range for images is [0,1].

5.8   Conclusion

Image registration models are often based on the assumption that every feature in a reference image has a suitable match in the template image. But, the assumption, correspondence everywhere, may fail in real-world applications. In this work, we illustrated two non-corresponding scenarios with their underlying physical characteristics. The deformation field has jump discontinuities and non-smooth characteristics, depending on the forward and backward map associated with the problem concerned with a crack formation. However, deformation fields, associated with the images with missing structures, are smooth in non-corresponding regions. We have proposed an image registration model for images with cracks, borrowing ideas from damage mechanics where a crack is identified through the stiffness loss of a material. We further analysed the first order optimality condition of the proposed objective function to point out limitations of the model and to explain the role of the regularization parameters with their physical meaning.

Our experimental results indicate that our model effectively identifies a crack

zone and simultaneously estimates regularised large deformations in the crack region. Moreover, deformations in the non-crack region are minimally influenced from the large deformations in the crack region. We analysed the sensitivity of the regularization parameters, which could be helpful to select parameters for real-world applications. The successful registration for intensity-preserving and mass-preserving phantoms demonstrate the wide applicability of our proposed model.

Implicit Reference based Motion-Compensated Reconstruction from Metallic Angle Interlaced Projections

Recently, Mohan *et al.* [Mohan15] have shown that the distribution of projection views over time, particularly based on an interlaced sampling scheme, enhances the quality of images reconstructed with a temporal regularized reconstruction model for dynamic computerized tomography (CT). To the best of our knowledge, the importance of the sampling scheme has not been emphasized for reconstructions with a motion-compensated (MC) reconstruction model. Major interlacing schemes are not fixed angular gap sampling (FAS) schemes, hence not easy to implement in practice. Moreover, the existing interlaced FAS schemes are not suitable to scan fast-moving objects. In section 6.1, we propose an interlaced FAS scheme based on the family of metallic angles and conduct a preliminary study to demonstrate the effectiveness of the proposed scheme for reconstructions with a reference based MC reconstruction model. In chapter 3, we discuss the state-of-the-art sampling schemes and reconstruction models for dynamic CT.

The reference image based MC reconstruction models have been popular from the last decade for different dynamic imaging modalities, *e.g.*, CT, MRI, PET, SPECT, *etc.* [McClelland17; Suhr15; Liu15; Hinkle12; Eyndhoven12; Blume12; Blume10; Chun09]. The need for invertibility of a deformation map naturally arises in the MC reconstruction to project back information from a given time frame to the reference frame. Therefore, an admissible deformation map should be a continuously differentiable function whose Jacobian determinant is nonzero almost everywhere, and is thus locally invertible and has a one-to-one correspondence. Moreover, in order to avoid local folding, *i.e.*, for an orientation-preserving deformation map, the Jacobian determinant is assumed to be strictly positive almost everywhere. Although, the invertibility is important, this has been addressed in very few studies related to the MC reconstruction [Suhr15; Hinkle12; Chun09]. Otherwise, the invertibility is ensured by adjusting regularization parameters for the deformation map regularizer [Blume12; Blume10]. Moreover, these studies dealt with small deformations with respect to the reference image and deformations are assumed to be smooth locally. In this work, we use a recently proposed hyperelastic regularizer [Burger13] for the deformation map that guarantees a positive Jacobian determinant almost everywhere. Even though, a MC reconstruction model guarantees an invertible map, the most popular existing numerical schemes [Chen07; Christensen01b] to compute an inverse of an invertible function does not guarantees that the computed inverse function has a positive determinant almost everywhere, and it is a one-to-one map. In this work, our numerical scheme guarantees that the computed inverse of a function has a positive Jacobian determinant almost everywhere.

The reference image in the reconstruction model either represent the physical state of an object at a fixed time [McClelland17; Suhr15; Eyndhoven12; Chun09], *e.g.*, a breath-hold state of a patient, or it represents a virtual state [Liu15; Blume10]. The time-dependent state is also known as an explicit reference frame (ERF) and the time-independent state or the virtual state is known as an implicit reference frame (IRF) in the image registration community. The IRF modelling eliminates bias towards a fixed physical state of an object and gathers knowledge from the entire dataset; this has been studied in the groupwise image registration community [Geng09]. However, the benefit of an IRF modelling has not been analysed thoroughly for the MC reconstruction in dynamic CT. Although the underlying principle behind the IRF and ERF modelling are different, the IRF based MC reconstruction model can be utilized for the ERF modelling by setting deformation map at some fixed time to an identity map.

In section 6.2, we present our model assumptions for X-ray measurements and in section 6.3, we explain an IRF based motion model. Thereafter, in section 6.4, we develop an IRF based MC reconstruction model for dynamic CT, and discuss a numerical scheme following the discretize-then-optimize approach in

section 6.5, and explain optimization algorithm in section 6.6. In section 6.7, we conduct a preliminary study to demonstrate the effectiveness of the proposed scheme based on a simulated dataset and perform a singular value decomposition (SVD) analysis to recognize limitations of a reference based MC reconstruction model in view of large and highly non-linear deformations over time. Section 6.8 conclude our findings.

6.1 Metallic Angle based Interlaced Sampling Scheme

The golden angle based fixed angular sampling (FAS) scheme is quite popular in the applications of neutron microtomography [Münch11]. The sampling pattern is aperiodic in this scheme and the angle between two consecutive projections is always approximately 137°. This is quite a large angular range to cover in a limited time, depending on the rotational speed of a gantry. The centripetal force acting on the rotating frame of a CT scanner limits the maximum possible speed of a gantry. Therefore, a gantry may not cover the angular range within the desired temporal resolution for a dynamic CT application. Therefore, the golden angle based FAS scheme is suitable only for slowly moving objects where a gantry can rotate multiple times around the object to acquire a sufficient number of projections to achieve a high spatio-temporal resolution.

The FAS scheme is easy to implement in practice. Therefore, a FAS scheme with an aperiodic scanning pattern, as it is for a golden angle based scheme, but with a smaller angular gap could be useful to scan a fast-moving object. In this work, we propose a fixed angular gap interlaced sampling scheme with smaller angular gaps based on the family of metallic angles where the golden angle is also a part of this family. The metallic angles are based on metallic means; hence we first introduce the family of metallic means in the next section.

6.1.1 Metallic Means

The family of metallic means [Spinadel99] comprises quadratic irrational numbers that is the positive solution of the algebraic equation

$$\phi^2 - n\phi - 1 = 0 \tag{6.1}$$

where n is a natural number. The positive root of (6.1) is given by

$$\phi_n = \frac{n + \sqrt{n^2 + 4}}{2}. \tag{6.2}$$

The metallic mean ϕ_1 is known as the golden mean or golden ratio, ϕ_2 is known as the silver ratio, and ϕ_3 is known as the bronze ratio.

The golden ratio has a simple geometrical interpretation. If a and b are two quantities with $a > b > 0$, the golden ratio is the ratio of the larger quantity a to the smaller quantity b if this ratio is equal to the sum of these two quantities to the larger quantity, *i.e.*,

$$\phi_1 = \frac{a}{b} = \frac{a + b}{a}. \tag{6.3}$$

The last two expressions in (6.3) form the quadratic equation $x^2 - x - 1 = 0$ where $x = a/b$. The positive root of this quadratic equation is equal to ϕ_1.

This geometrical interpretation motivated us to represent a metallic mean in the following way

$$\phi_n = \frac{a}{b} = \frac{na + b}{a}. \tag{6.4}$$

where the last identity forms the quadratic equation (6.1). In the next section, we define metallic angles utilizing these geometrical interpretations on the circumferences of a circle.

6.1.2   Metallic Angles

If the circumference of a circle is divided into two segments a and b with $a > b > 0$ such that segments length satisfy (6.3), the golden angle is the angle subtended by the smaller arc of length b at the center of the circle. The golden angle ψ_1 utilizing (6.3) is computed as

$$\psi_1 = 2\pi \frac{b}{a + b} = 2\pi \frac{1}{1 + \phi_1} \approx 2.39996 \text{ rad.} \tag{6.5}$$

Similarly, if segments of a circumeference of a circle satisfies (6.4), the metallic angle is defined as the angle subtended by the smaller arc at the center, *i.e.*,

$$\psi_n = 2\pi \frac{b}{a + b} = 2\pi \frac{1}{1 + \phi_n}. \tag{6.6}$$

Table 6.1 lists the first few metallic ratios and the corresponding metallic angles.

Table 6.1: First eight metallic ratios and metallic angles.

n	ϕ	ψ (rad)	ψ (degree)	n	ϕ	ψ (rad)	ψ (degree)
0	1	3.1416	180°	4	4.2361	1.1999	68.7539°
1	1.6180	2.3999	137.5078°	5	5.1926	1.0146	58.1341°
2	2.4142	1.8403	105.4416°	6	6.1623	0.8773	50.2633°
3	3.3028	1.4603	83.6669°	7	7.1401	0.7719	44.2257°

6.1.3   Fixed Angular Gap Interlaced Sampling Scheme

Similar to the golden angle based FAS scheme, we define a kth view angle

$$\theta_n^k = k\psi_n \bmod 2\pi, \quad k \in \mathbb{N}, \tag{6.7}$$

where ψ_n is a metallic angle as defined in (6.6); this is an angular gap between two consecutive projections. In one full rotation, there will be total N_n projections with N_n given by

$$N_n = \left\lfloor \frac{2\pi}{\psi_n} \right\rfloor = \lfloor 1 + \phi_n \rfloor = n + 1. \tag{6.8}$$

Therefore, if N_p is the desired number of projections in a rotation, one should choose a metallic angle ψ_n with $n = N_p - 1$.

The sampling scheme based on (6.7) has following properties :

- **Fixed Angular gap**:

  The angular gap between two consecutive projections is always ψ_n, therefore the proposed sampling scheme is a FAS scheme. Hence, it is easy to implement in practice.

- **Aperiodic Pattern**:

  The sampling pattern is aperiodic, hence, ideally, each projection provides new information about the object of interest. We can easily prove our aperiodicity claim by the proof of contradiction, considering the fact that the metallic ratio ϕ_n is an irrational number except for $n = 0$. If the sampling pattern is periodic, the following identities must be true, *i.e.*,

$$m\psi_n = \psi_n + 2k\pi, \quad m, k \in \mathbb{N}$$
$$\frac{\psi_n}{2\pi} = \frac{k}{m-1},$$
$$\phi_n = \frac{m-1}{k} - 1.$$

According to this identity, ϕ_n should be a rational number but this is a contradiction.

- **Interlaced Sampling**:

  Fortunately, interlacing behavior comes out naturally from the metallic angle based sampling pattern as shown in Fig. 6.1. Suppose, we acquire in total 24 projections during an experiment. If we intend to reconstruct 3 image frames with 8 projections per frame covering one full rotation, the fixed angular gap between two consecutive projections should be ψ_7, using the expression (6.8), for the complete experiment. The Fig. 6.1(a) displays the sampling pattern with $\Delta\theta = \psi_7$ wrapped around 2π. The projection angles for two consecutive frames are different; moreover they are interleaved. The Fig. 6.1(b) displays a sampling pattern when we intend to reconstruct 4 frames in the same amount of time to increase the temporal resolution.
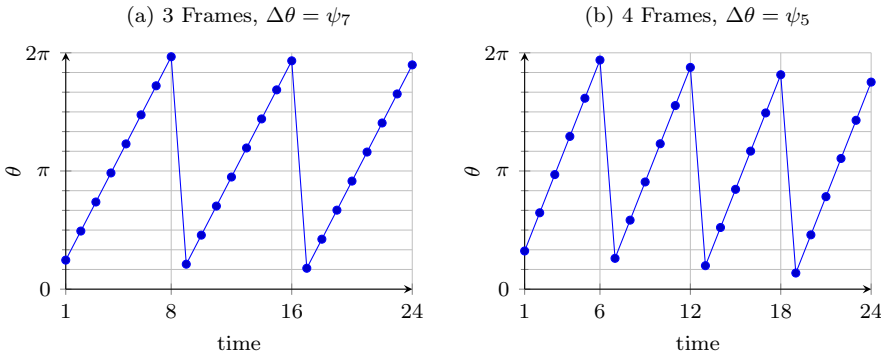
Figure 6.1: Distribution of 24 projection views over time based on the metallic angle based interlacing scheme. (a) displays distributions in 3 full cycles, and (b) displays distributions in 4 full cycles.

6.2   System and Measurement Model

An X-ray source illuminates a deforming object that is characterized by its spatio-temporal attenuation function $\mu(x,t) : \Omega \subset \mathbb{R}^2 \times \mathbb{R} \mapsto \mathbb{R}$, where the spatial coordinate $x = [x_1, x_2]$ is a physical point in the two-dimensional domain and t represents a temporal coordinate. A one-dimensional detector array with r elements acquires the attenuated X-rays from p projections. The data acquisition time for the complete experiment is T sec. The detector exposure time for one projection, *i.e.*, T_e sec., is less than the gantry rotation time between two

consecutive projections, *i.e.*, T/p sec. The average X-ray source photon flux is I_0 photons/sec. We assume that the measurement y_{ij}, obtained with detector i and projection j, is a sample of a Poisson random variable $\mathbf{Y}_{ij}$ whose mean is prescribed by the Lambert-Beer law, *i.e.*,

$$\mathbf{Y}_{ij} = y_{ij} \mid \mu(x,t) \sim \text{Poisson}\left(I_0 T_e \exp\left(-\int_{l_{ij}} \mu(x,t)dx\right)\right) \qquad (6.9)$$

where l_{ij} denotes the line segment between the ith detector element and the source for projection j.

6.3   Implicit Reference based Motion Modelling
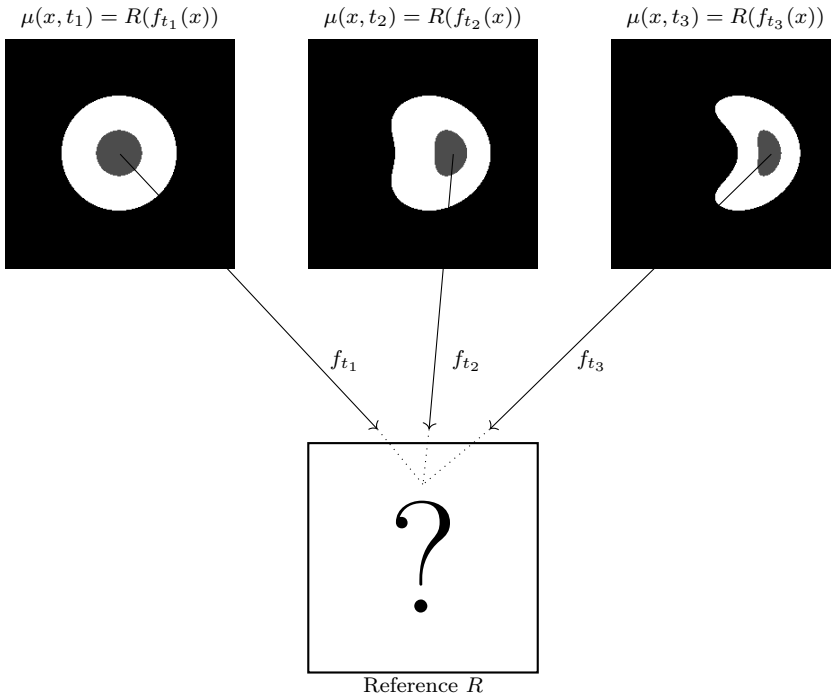
Figure 6.2: Illustration of the implicit reference based motion modelling.

We assumed that a physical state of an object at time t is a deformed configuration of an implicit reference frame $R : \Omega \subset \mathbb{R}^2 \mapsto \mathbb{R}$, *i.e.*,

$$\mu(x,t) = R(f_t(x)) \qquad (6.10)$$

where $f_t : \Omega \subset \mathbb{R}^2 \mapsto \mathbb{R}^2$ is a continuously differentiable deformation map and has a one-to-one correspondence, almost everywhere, at time t. Each physical point in the reference image R has a unique match in the image μ at all instants of time. The motion model (6.10), due to our underlying assumptions, is not suitable for deformations like crack formations, described by a jump discontinuity in the deformation map, or closing of a crack, described by a non-smooth continuous deformation map, as illustrated in chapter 5.

Fig. 6.2 illustrates the motion modelling graphically. Assuming a locally invertible deformation map, the reference image can also be represented in terms of each image in the image sequence that represents a deforming object, therefore the reference frame satisfies the following identity, *i.e.*,

$$R(x) = \frac{1}{K} \sum_{i=1}^{K} \mu(f_{t_i}^{-1}(x), t_i). \tag{6.11}$$

Generally, there is more than one f that satisfies (6.10), therefore regularization of a deformation map becomes utmost important to restrict the solution space. We do so with the recently proposed hyperelastic energy regularizer [Ruthotto15], *i.e.*,

$$E(f) = \int_{\Omega} \frac{1}{2} \alpha_l \|\nabla(f - f_{\text{ref}})\|_2^2 + \alpha_v \varphi(\det(\nabla f(x))) \tag{6.12}$$

where $\varphi(v) = (v-1)^4/v^2$, α_l, and α_v are regularization parameters and f_{ref} represents an initial configuration. They regularize deformation locally by controlling the change in displacement and the change in local volume simultaneously. The regularizer (6.12) guarantees a positive Jacobian determinant almost everywhere by attaining infinite energy for non-diffeomorphic deformations. The positive Jacobian determinant ensures an orientation-preserving and one-to-one map that is desirable to fulfill our model assumptions. Moreover, this is an appropriate regularizer for large and non-linear deformations.

After incorporating the motion model (6.10), the expression (6.9) yields

$$\mathbf{Y}_{ij} = y_{ij} \mid R, f_t \sim \text{Poisson}\left(I_0 T_e \exp\left(-\int_{l_{ij}} R(f_t(x)) \, dx\right)\right). \tag{6.13}$$

Note that, the measurement y_{ij} is conditioned on a deformation map f_t and a reference frame R.

For ease of notation, we define a linear operator A_{ij} which represents the line integral of a function along the line l_{ij}. The linear operator T_{f_t}, with respect to R, is defined as

$$T_{f_t} R(x) = R(f_t(x)).$$

Following these notations, we can express (6.13) as

$$\mathbf{Y}_{ij} = y_{ij} \mid R, f_t \sim \text{Poisson}\left(I_0 T_e \exp\left(-A_{ij} T_{f_t} R\right)\right). \tag{6.14}$$

6.4 Motion-Compensated Reconstruction Model

We consider that an image sequence of K reconstructed frames represent the evolution of an object with time. We assume that the object is deforming during an experiment and a gantry is rotating fast such that the object movement is assumed to be stationary while acquiring p consecutive projections over a full cycle. A detector array of r elements acquire total $N_p = K \times p$ projections during the complete experiment. We divide measurements in K groups where each group has $r \times p$ measurements. We add another subscript to represent a measured data, $i.e.$, y_{ijk}, for the kth group and represent them in total by a vector $y_k = (y_{11k}, \ldots, y_{rpk})$.

Measurement samples are independent, therefore we can define the joint probability of measurements for the kth group, using (6.14), as

$$\text{P}(y_k \mid R, f_k) = \prod_{i=1}^{r} \prod_{j=1}^{p} \frac{(I_0 T_e \exp(-A_{ijk} T_{f_k} R))^{y_{ijk}}}{y_{ijk}} \exp(-A_{ijk} T_{f_k} R). \tag{6.15}$$

Likewise, the joint probability of the complete set of measured data is given by

$$\text{P}(y_1, \ldots, y_K \mid R, f_1, \ldots, f_K) = \text{P}(y_1 \mid R, f_1) \times \cdots \times \text{P}(y_K \mid R, f_K). \tag{6.16}$$

According to Bayes' rule, the joint posterior distribution of unknown parameters is given by

$$\text{P}(R, f_1, \ldots, f_K \mid y_1, \ldots, y_K) \propto \text{P}(y_1, \ldots, y_K \mid R, f_1, \ldots, f_K)\, \text{P}(R)\, \text{P}(f_1, \ldots, f_K). \tag{6.17}$$

assuming the reference image R and deformation maps f_t are independent of each other.

We define prior distribution on deformation fields in the form

$$\text{P}(f_1, \ldots, f_K) = \prod_{k=1}^{K} \text{P}(f_k) \propto \prod_{k=1}^{K} \exp(-\alpha E(f_k)), \tag{6.18}$$

where α is a regularization parameter and E is defined in (6.12), and prior distribution on R in the form

$$\mathrm{P}(R) \propto \exp(-\gamma\phi(R)) \tag{6.19}$$

where ϕ is a convex function with respect to R and γ is a regularization parameter. The combination of nonnegativity constraint and total variation (TV) approximated regularization is expressed as

$$\phi(R) = I_+(R) + \mathrm{TV}_\epsilon(R) \tag{6.20}$$

where

$$\mathrm{TV}_\epsilon(R) = \int_\Omega \psi(||\nabla R)||_2) \; dx, \tag{6.21}$$

and $\psi(t)$ is a Huber loss function with smoothing parameter ϵ. $I_+(R)$ denotes the indicator function of the nonnegative orthant.

A maximum a posteriori (MAP) estimate of unknowns is given by

$$
\begin{aligned}
(\hat{R}, \hat{f}_1, \ldots, \hat{f}_K) &= \operatorname*{argmin}_{(R, f_1, \ldots, f_K)} \left\{ -\log \mathrm{P}(R, f_1, \ldots, f_K \mid y_1, \ldots, y_K) \right\}, \\
&= \operatorname*{argmin}_{(R, f_1, \ldots, f_K)} \left\{ \mathcal{D}(R, f_1, \ldots, f_K) + \mathcal{S}(R) + \mathcal{E}(f_1, \ldots, f_K) \right\}.
\end{aligned}
\tag{6.22}
$$

where

$$\mathcal{D}(R, f_1, \ldots, f_K) = \sum_{k=1}^{K} \sum_{i=1}^{r} \sum_{j=1}^{p} y_{ijk} A_{ijk} T_{f_k} R + I_0 T_e \exp(-A_{ijk} T_{f_k} R), \tag{6.23}$$

$$\mathcal{S}(R) = \gamma\phi(R), \tag{6.24}$$

and

$$\mathcal{E}(f_1, \ldots, f_K) = \alpha \sum_{k=1}^{K} E(f_k). \tag{6.25}$$

The (6.22) is a convex minimization problem in R given deformation fields f, but it is a non-convex problem in deformation fields f given R. Moreover, the problem (6.22) is separable in the deformation fields and can be minimized in an alternating fashion, *i.e.*,

$$R^m = \operatorname*{argmin}_{R} \mathcal{D}(R, f_1^{m-1}, \ldots, f_K^{m-1}) + \mathcal{S}(R) \tag{6.26}$$

$$f_k^m = \operatorname*{argmin}_{f_k} \mathcal{D}(R^m, f_k) + \mathcal{E}(f_k), \quad k = 1, \ldots, K. \tag{6.27}$$

6.5   Numerical Implementation
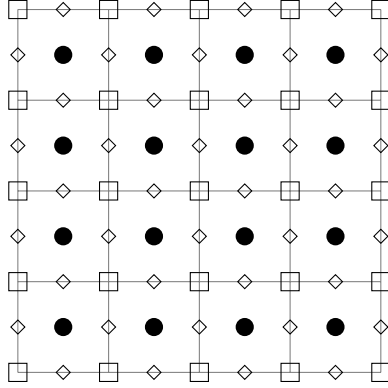
Figure 6.3: A two-dimensional grid: cell-centered xc (●), nodal xn (□), and staggered xs (◇)

.

We follow the discretize-then-optimize approach to solve the MAP estimation problem (6.22). We discretize a two-dimensional image domain $\Omega = (-sz, sz) \times (-sz, sz)$ into $n \times n$ cells of width h as shown in Fig. 6.3. Let xc denote a cell-centered grid and xn denote a nodal grid. We discretize reference function R on the cell-centered grid and represent it by $R^h \in \mathbb{R}^{n^2}$. Whereas, the deformation field $f = (f_1, f_2)$ is discretized on the nodal grid and represented by $f^h = ((f^h)_1, (f^h)_2) \in \mathbb{R}^{2(n+1)^2}$.

We approximate the continuous function R over the mth cell with its function value at the cell-centered grid xc_m; and the line-integral over a cell is approximated as,

$$\int_{l_m} R(f(x)) \; dx \approx w_m^h R(f(xc_m)) \tag{6.28}$$

where w_m^h is length of the intersection of the slab l with the mth cell. The weights w^h are stored component-wise in a row vector $A_{ij}^h \in \mathbb{R}^{1 \times n^2}$ corresponding to the line integral along l_{ij}.

The computation of $R(f(xc_m))$ on the cell-centered point of a mth cell consists of two steps. First, we interpolate the discretized deformation field f^h on the cell-centered point xc_m to compute $f^h[xc_m]$, and afterward we interpolate the discretized reference function R^h at $f^h[xc_m]$ to compute $R^h[f^h[xc_m]]$. Therefore,

the approximated line-integral, utilizing (6.28), is represented as,

$$
\begin{aligned}
\int_{l_{ij}} R(f(x)) \, dx = A_{ij} T_f R &= \sum_{m=1}^{n^2} \int_{(l_{ij})_m} R(f(x)) \, dx \\
&\approx \sum_{m=1}^{n^2} w_m^h R(f(xc_m)) \\
&\approx \sum_{m=1}^{n^2} w_m^h R^h[f^h[xc_m]] \\
&= A_{ij}^h T_{f^h} R^h
\end{aligned}
\tag{6.29}
$$

where $(T_{f^h} R^h)[xc_m] = R^h[f^h[xc_m]]$.

The discrete form of the data fidelity function (6.23), utilizing (6.29), is represented as

$$
\mathrm{D}[R^h, f_1^h, \dots, f_K^h] = \sum_{k=1}^{K} \sum_{i=1}^{r} \sum_{j=1}^{p} y_{ijk} A_{ijk}^h T_{f_k^h} R^h + I_0 T_e \exp(-A_{ijk}^h T_{f_k^h} R^h),
\tag{6.30}
$$

and the gradients of D are

$$
\nabla \mathrm{D}[R^h] = \sum_{k=1}^{K} \sum_{i=1}^{r} \sum_{j=1}^{p} T_{f_k^h}^{\ T} A_{ijk}^{h\ T} (y_{ijk} - \hat{y}_{ijk}),
\tag{6.31}
$$

$$
\nabla^2 \mathrm{D}[R^h] = \sum_{k=1}^{K} \sum_{i=1}^{r} \sum_{j=1}^{p} T_{f_k^h}^{\ T} A_{ijk}^{h\ T} \hat{y}_{ijk} A_{ijk}^h T_{f_k^h},
\tag{6.32}
$$

$$
\nabla \mathrm{D}[f_k^h] = \sum_{i=1}^{r} \sum_{j=1}^{p} \left(\frac{\partial T_{f_k^h} R^h}{\partial f_k^h} \right)^T A_{ijk}^{h\ T} (y_{ijk} - \hat{y}_{ijk}),
\tag{6.33}
$$

$$
\nabla^2 \mathrm{D}[f_k^h] \approx \sum_{i=1}^{r} \sum_{j=1}^{p} \left(\frac{\partial T_{f_k^h} R^h}{\partial f_k^h} \right)^T A_{ijk}^{h\ T} \hat{y}_{ijk} A_{ijk}^h \frac{\partial T_{f_k^h} R^h}{\partial f_k^h}
\tag{6.34}
$$

where $\hat{y}_{ijk} = I_0 T_e \exp(-A_{ijk}^h T_{f_k^h} R^h)$.

The first derivative of D with respect to R^h, as defined in (6.31), requires the adjoint of the transformation operator T_f. According to the definition of an adjoint operator, *i.e.*,

$$
\langle T_f \mu, g \rangle = \langle \mu, T_f^T g \rangle,
$$

$$
\Rightarrow \int_{\Omega} \mu(f(x)) g(x) \, dx = \int_{f(\Omega)} \mu(x) g(f^{-1}(x)) \frac{1}{\det(\nabla f)(f^{-1}(x))} \, dx
$$

the adjoint of a transformation operator T is given by,

$$T_f^T g(x) = \frac{g(f^{-1}(x))}{\det(\nabla f)(f^{-1}(x))} = g(f^{-1}(x))\det(\nabla f^{-1})(x) \qquad (6.35)$$

where the last identity arises from the inverse function theorem and Jacobian determinant of f is assumed to be positive.

Remark 1: A non-zero condition on the Jacobian determinant of $f : \Omega \mapsto \mathbb{R}^2$ guarantees that, for every point p in Ω, there exists a neighborhood around p over which f is invertible. But, this does not mean that f is invertible over its entire domain. We impose a Dirichlet boundary condition on f such that the displacement along the boundary is zero. As a result, the image of function f restricts to a domain $\Omega_f \subset \mathbb{R}^2$ if Jacobian determinant of f is positive almost everywhere in Ω. Hence, we can guarantee that $f : \Omega \mapsto \Omega_f$ is globally invertible over its entire domain, where $f^{-1} : \Omega_f \mapsto \Omega$ is the inverse function.

We use the midpoint quadrature rule to compute the integral in the expression (6.21), *i.e.*,

$$\begin{aligned}
\text{TV}_\epsilon(R) &= \int_\Omega \psi(||\nabla R)||_2) \; dx \\
&\approx h^2 \sum_{m=1}^{n^2} \psi(||\nabla R(xc_m)||_2) \\
&\approx h^2 \sum_{m=1}^{n^2} \psi(||D_m R^h||_2) \\
&= \text{TV}_\epsilon^h[R^h] \qquad (6.36)
\end{aligned}$$

where D_m is the 2D discrete derivative operator, defined as,

$$D_m = \begin{bmatrix} e_m^T(I_n \otimes \bar{D}_n) \\ e_m^T(\bar{D}_n \otimes I_n) \end{bmatrix}$$

where I_n is an identity matrix, and $\bar{D}_n$ is a 1D discrete derivative operator, defined as,

$$\bar{D}_n = \frac{1}{2h} \begin{bmatrix} -1 & 1 & & & & \\ -1 & 0 & 1 & & & \\ & & \ddots & \ddots & & \\ & & & -1 & 0 & 1 \\ & & & & -1 & 1 \end{bmatrix} \in \mathbb{R}^{n \times n}$$

assuming Dirichlet boundary conditions.

The discretize form of the regularizer $S(R)$ as defined in (6.24), utilizing (6.20) and (6.36) is represented as

$$\mathrm{S}[R^h] = I_+(R^h) + \gamma \mathrm{TV}_\epsilon^h[R^h]. \tag{6.37}$$

We also use the midpoint quadrature rule to compute the expression (6.12), *i.e.*,

$$
\begin{aligned}
E(f) &= \int_\Omega \frac{1}{2}\alpha_l \|\nabla(f(x) - f_{\mathrm{ref}}(x))\|_2^2 + \alpha_v \varphi(\det(\nabla f(x)))\ dx \\
&\approx h^2 \sum_{m=1}^{n^2} \frac{1}{2}\alpha_l \|\nabla(f(xc_m) - f_{\mathrm{ref}}(xc_m))\|_2^2 + \alpha_v \varphi(\det(\nabla f(xc_m))) \\
&\approx h^2 \left(\frac{\alpha_l}{2}(f^h - f_{\mathrm{ref}}^h)^T B^{h^T} B^h (f^h - f_{\mathrm{ref}}^h) + \alpha_v \varphi(\det(\nabla f^h)) \right) \\
&= E[f_k^h] \tag{6.38}
\end{aligned}
$$

where B^h is a discrete derivative operator, defined as,

$$
B^h = \begin{bmatrix} I_{(n+1)} \otimes \bar{B}_n \\ \bar{B}_n \otimes I_{(n+1)} \\ & & I_{(n+1)} \otimes \bar{B}_n \\ & & \bar{B}_n \otimes I_{(n+1)} \end{bmatrix} \in \mathbb{R}^{4n(n+1) \times 2(n+1)^2}
$$

where I_n is the identity matrix. $\bar{B}_n$ is a one-dimensional short central finite difference operator, defined as,

$$
\bar{B}_n = \frac{1}{h} \begin{bmatrix} -1 & 1 \\ & \ddots & \ddots \\ & & -1 & 1 \end{bmatrix} \in \mathbb{R}^{n \times (n+1)}.
$$

The components of the gradient of f_1 and f_2 are approximated at different locations on staggered grids because of the desired second order approximation of partial derivatives of $f = (f_1, f_2)$. The finite difference approximation is not appropriate to approximate Jacobian determinant

$$\det(\nabla f(x))(x) = \partial_1 f_1(x) \partial_2 f_2(x) - \partial_2 f_1(x) \partial_1 f_2(x)$$

because the determinant couples partial derivatives approximated at different locations. Therefore, Burger *et al.* suggested to approximate $\det(\nabla f(x))$ by measuring volume changes on a voxel based on a tetrahedral partition. We refer readers to the original work by Burger [Burger13] for a detailed description related to discretization and partial derivatives of the hyperelastic energy regularizer $E(f)$.

The discrete form of the regularizer $\mathcal{E}$ as defined in (6.25), utilizing (6.38), is represented as

$$\mathrm{E}[f_1^h, \cdots, f_K^h] = \alpha \sum_{k=1}^{K} E[f_k^h]. \tag{6.39}$$

To summarize, the discretized objectiove functional of (6.22) is expressed as,

$$\mathrm{J}[R^h, f_1^h, \ldots, f_K^h] = \mathrm{D}[R^h, f_1^h, \ldots, f_K^h] + \mathrm{S}[R^h] + \mathrm{E}[f_1^h, \ldots, f_K^h]. \tag{6.40}$$

6.6 Algorithms

We minimize the objective function (6.40) with respect to R^h and f^h in an alternating fashion, *i.e.*,

$$(R^h)^m = \underset{R^h}{\operatorname{argmin}} \mathrm{D}[R^h, (f_1^h)^{m-1}, \ldots, (f_K^h)^{m-1}] + \mathrm{S}[R^h] \tag{6.41}$$

$$(f_k^h)^m = \underset{f_k^h}{\operatorname{argmin}} \mathrm{D}[(R^h)^m, f_k^h] + \mathrm{E}[f_k^h], \quad k = 1, \ldots, K. \tag{6.42}$$

We use different optimization algorithms to estimate the reference image R^h and the deformation maps f^h which we will explain in this section in detail.

The gradient of D with respect to R^h involves the adjoint of the transformation operator T, defined in (6.35), that require an inverse of the deformation map f^h. We compute the inverse with an iterative scheme.

6.6.1 Inverse of a Deformation Map

Suppose, a deformation map $f : \Omega \mapsto \Omega_f$ and a function $g : \Omega_f \mapsto \Omega$ satisfy the identity

$$z = f(g(z)), \quad z \in \Omega_f, \tag{6.43}$$

then the function g is called an inverse function of f.

The estimation of the inverse function g is a root finding problem, which is expressed by rewriting (6.43) as

$$f(g) = z - f(g(z)) = 0. \tag{6.44}$$

We define an iterative sequence to solve the problem (6.44), motivated from [Chen07; Christensen01b], *i.e.*,

$$g_{k+1} = g_k + \alpha f(g_k), \tag{6.45}$$

where α is a step-size chosen such that

$$f(g_{k+1}) \leq f(g_k) \quad \text{and} \quad \det(\nabla g_k) > 0$$

to ensure an orientation preserving and a one-to-one function g.

In practice, (6.45) works satisfactorily with a good initial guess g_0. In order to compute g_0, we triangulate the domain Ω. Suppose, a triangle $T \subset \Omega$ deforms to a triangle $T_f \subset \Omega_f$, then we can compute barycentric coordinates (b_1, b_2, b_3) of a point $z \in T_f$ with respect to the triangle T_f such that

$$z = \sum_{i=1}^{3} b_i y_i^h,$$

where y_1^h, y_2^h, y_3^h are the vertices of the deformed triangle T_f. Utilizing these barycentric coordinates, we can approximate the inverse function g_0, corresponding to the point z by defining

$$g_0(z) = \sum_{i=1}^{3} b_i x_i^h$$

where x_1^h, x_2^h, x_3^h are the vertices of the triangle T in the domain Ω.

6.6.2 Reference Frame Estimation

The objective function (6.40) with respect to R^h is given by

$$J[R^h] = D[R^h] + S[R^h]. \tag{6.46}$$

The gradient of $D[R^h]$ is Lipschitz continuous because the norm of Hessian $\nabla^2 D[R^h]$ defined in (6.32) satisfies the following inequalities, *i.e.*,

$$\|\nabla^2 D[R^h]\|_2 = \sum_{k=1}^{K} \sum_{i=1}^{r} \sum_{j=1}^{p} T_{f_k^h}^T {A_{ijk}^h}^T \hat{y}_{ijk} A_{ijk}^h T_{f_k^h}$$

$$\leq \sum_{k=1}^{K} \sum_{i=1}^{r} \sum_{j=1}^{p} \|T_{f_k^h}\|_2^2 \|{A_{ijk}^h}^T \hat{y}_{ijk} A_{ijk}^h\|_2 \tag{6.47}$$

and the approximated Lipschitz constant L is given by

$$L = \sum_{k=1}^{K} \sum_{i=1}^{r} \sum_{j=1}^{p} \|T_{f_k^h}\|_2^2 \|A_{ijk}^h{}^T y_{ijk} A_{ijk}^h\|_2.$$

The function $\mathrm{TV}_\epsilon^h[R^h]$ also has a Lipschitz continuous gradient with constant $L_{tv}(\epsilon) = \|D\|_2^2/\epsilon$ where $D = [D_1^T \cdots D_{n^2}^T]^T$. Therefore, $\mathrm{J}[R^h]$ is differentiable with Lipschitz continuous gradients on the nonnegative orthant, and hence we can apply a proximal gradient method which is suitable for minimizing problems of the form

$$\underset{u}{\text{minimize}} \quad g(u) + h(u).$$

Here $g : \mathbb{R}^{n^2} \to \mathbb{R}$ is convex with a Lipschitz continuous gradient with Lipschitz constant L_g, $h : \mathbb{R}^{n^2} \to \mathbb{R}$ is convex, and the prox-operator

$$\mathrm{prox}_{th}(\bar{u}) = \underset{u}{\text{argmin}} \left\{ th(u) + \frac{1}{2}\|u - \bar{u}\|_2^2 \right\}$$

is assumed to be cheap to evaluate. We will define $g(u) = \mathrm{D}(u) + \gamma \mathrm{TV}_\epsilon(u)$ and $h(u) = I_+(u)$, and hence the Lipschitz constant is given by $L_\mathrm{J} = L + \gamma L_\mathrm{tv}(\epsilon)$. Given a starting point $u^{(0)}$ and a fixed number of iterations K, the algorithm can be summarized as

$$u^{(k)} = \mathrm{prox}_{th}(u^{(k-1)} - t\nabla g(u^{(k-1)})), \ k = 1, 2, \ldots, K$$

where $t \in (0, 2/L_\mathrm{J})$ is the step size and $\mathrm{prox}_{th}(\bar{u}) = \max(0, \bar{u})$ is the projection onto the nonnegative orthant. With this step size, the method is a descent method.

6.6.3 Motion Estimation

The objective function (6.40) with respect to f_k^h is given by

$$\mathrm{J}[f_k^h] = \mathrm{D}[f_k^h] + \mathrm{E}[f_k^h]$$

and it is a non-convex function. We use the Gauss-Newton optimization algorithm to compute a local minimizer with a multilevel strategy. First, we compute the minimizer on a coarse discretization, which serves as a starting guess for the optimization problem at a finer level. Given a starting point $(f_h^k)^0$, the iterative sequence is given by

$$(f_h^k)^m = (f_h^k)^{m-1} - s\Delta f_k^h$$

where we use Armijo backtracking line search method to compute the step size s and solve a linear system

$$\mathrm{H} \, \Delta f_k^h = \nabla \mathrm{J}[(f_h^k)^{m-1}] \tag{6.48}$$

for Δf_k^h where H is an approximated Hessian matrix at $(f_h^k)^{m-1}$. Following the remark 1 6.5, we incorporate the Dirichlet boundary conditions for f_h^k by modifying the rows and columns of the Hessian matrix H such that $\Delta f_h^k = 0$ at the boundary nodes.

6.7 Numerical Results

We conduct a series of experiments based on the simulated data to evaluate the performance of the proposed sampling scheme with the motion-compensated reconstruction model. In these experiments, we used a parallel beam geometry with a 2 cm wide photon counting detector array with 64 detector elements. The measurements with the object were generated according to (6.9) using a $2N \times 2N$ pixel discretization of a 2D phantom defined on a 4 cm^2 domain. To avoid inverse crimes, we computed our reconstructions on an $N \times N$ ($N = 64$) pixel grid. The value of the TV-smoothing parameter ϵ was 0.01 cm^{-1} in all experiments with the TV-prior. We determine the parameter γ for the TV-prior based on subjective visualization. We used the ASTRA Toolbox (version 1.7.1beta) to implicitly compute products with A and A^T on a GPU.

We use a linear interpolation method to interpolate the reference function R^h at f^h during minimization of the objective function (6.46) for the reference image. However, we need to use a smooth interpolation function for the motion estimation, where we use a regularized spline interpolation with a bending energy regularizer with a smoothing parameter $\theta = 4 \times 10^{-2}$. Our choices for the interpolation functions are based on numerical observations. If we do not use a smooth interpolant, the minimizing sequence may get stuck in an undesirable local minimum. We think that a regularized spline interpolation gives a smooth representation of the non-convex objective function and avoids small oscillations around a local minimum. We also follow a multilevel strategy to minimize the non-convex objective function. We represent the objective function at three levels and optimize them sequentially at each level. The solution at a coarse level serves as an initial guess at a finer level. In this work, we are extensively using built-in functions of the FAIR toolbox [Modersitzki09] unless stated otherwise.

We introduce a scaling factor in the objective function (6.40) and minimize the

following problem, *i.e.*,

$$\min_{R^h, f_1^h, \ldots, f_K^h} \frac{1}{I_0 T_e} \mathrm{D}(R^h, f_1^h, \ldots, f_K^h) + \mathrm{S}(R^h) + \mathrm{E}(f_1^h, \ldots, f_K^h), \qquad (6.49)$$

to avoid the dependence of regularization parameters on the magnitude of $I_0 T_e$ to a certain extent.

6.7.1 Performance of Sampling Schemes
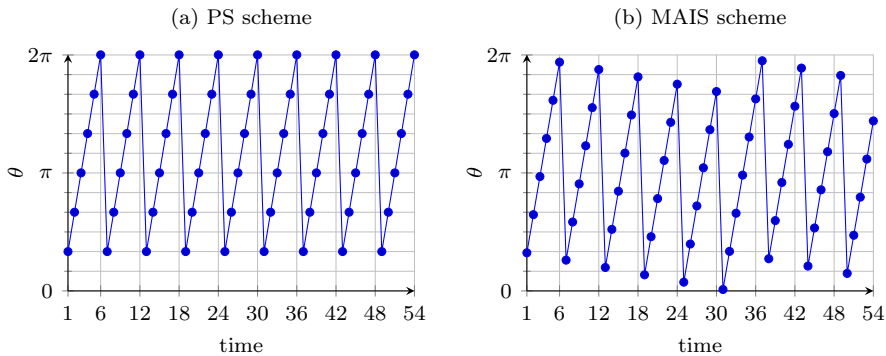
Figure 6.4: Distribution of projection views over time with the progressive sampling (PS) scheme and the proposed interlaced sampling scheme based on the family of metallic angles (MAIS).

In this experiment, we illustrate the effects of the sampling schemes on the reconstructions of a deforming object, as shown in Fig. 6.5(a), with the motion-compensated reconstruction model (6.49). The acquired projections either follow the progressive sampling scheme (PS) or the proposed interlaced sampling scheme based on the family of metallic angles (MAIS) as illustrated in Fig. 6.4 for our setup. We acquire in total 54 projections to reconstruct 9 frames assuming that the object is stationary while acquiring 6 consecutive projections for one frame. The angular gap between two consecutive projections is $2\pi/6$ for the PS scheme and it is ψ_5 for the MAIS scheme following (6.8). The projection directions are the same for each frame in the PS scheme, whereas all the projection directions are unique in the MAIS scheme. For our experiment, we can not use a bit-reversal based interlaced sampling scheme because it requires the total number of frames to be a power of 2, whereas we need a sampling scheme for 9 frames in total. We used the source intensity $I_0 = 10^7$ photons/sec and the detector exposure time $T_e = 1$ sec. The optimization algorithm stops when the relative change in the objective function value with respect to the previous iterate is less than 10^{-6}.
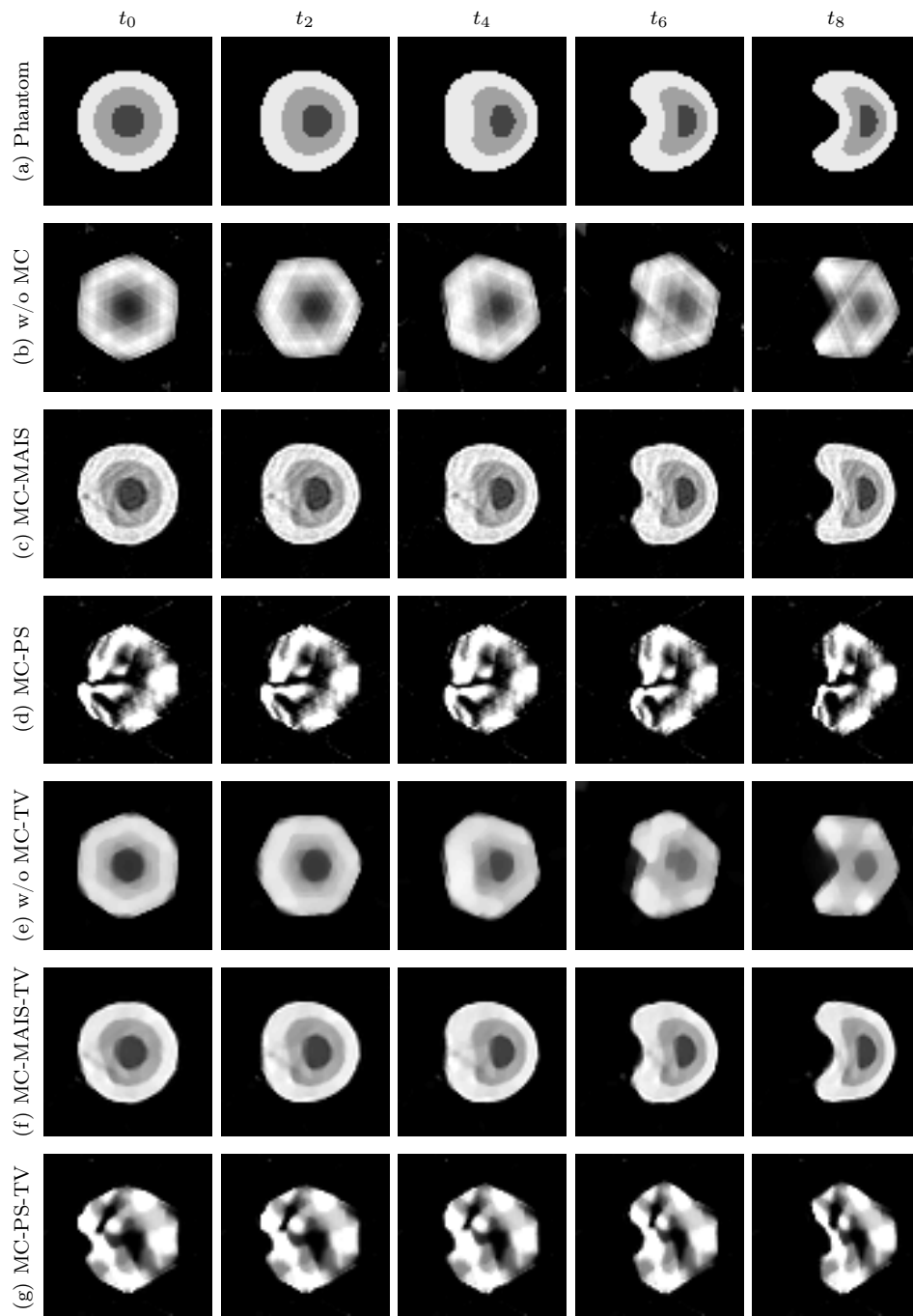
Figure 6.5: Phantom and reconstructions based on the simulated datasets with the PS and the MAIS schemes. The display range for images is 0 to 1.1 cm^{-1}. The reconstructions with the TV-prior were computed with $\gamma = 5 \times 10^{-4}$. The regularization parameter for the hyperelastic regularizer is $\alpha = 1$.

Fig.6.5(a) shows the deformation of the object only at 5 instants of time out of total 9 time points. The reconstructions without motion compensation (w/o MC) are shown in Fig. 6.5(b). Here, we reconstruct each frame independently with the AMAP reconstruction model derived in chapter 4. These reconstructions have limited angle artifacts due to reconstruction with a few number of projections, *i.e.*, only 6 projections which are acquired for a frame. On the other hand, the reconstructions with the motion-compensated reconstruction (MC) model (6.49), particularly with MAIS scheme, shows tremendous improvements as shown in Fig.6.5(c). However, the MC reconstructions with the PS scheme are distorted as shown in Fig.6.5(d). Intuitively, we can argue that the measured projections following the MAIS scheme have more information about the deformation of the object than the information collected with the PS scheme. To gain more insight into this subject, we perform the singular value decomposition (SVD) analysis of the MC reconstruction model in the next section.

Fig.6.5(e), (f), and (g) are reconstructions with a spatial TV regularization on the reference image. Even with the TV regularizer that smooths uniform intensity regions and preserve edges across regions, we do not see much improvement for reconstructions with the PS scheme. For all the motion-compensated reconstructions, we initialize the optimization algorithm with a reconstruction computed for the time point t_4 with the AMAP model, *i.e.*, without a motion-compensation approach. We also observe few line artifacts around the central regions of the MC reconstructions with the MAIS sampling scheme; the real reason behind these artifacts are not known to us.

6.7.2 SVD Analysis

In this study, we aim to analyze the impact of the sampling schemes on the reconstructions with the MC reconstruction model. Moreover, we intend to recognize the limitation of the MC reconstruction model due to large deformations with respect to the reference frame. We first derive a weighted least-squares MC reconstruction model and define a MC linear system for study. We later analyze the singular value decay of the system matrix associated with the defined MC linear system.

If y is positive, a quadratic approximation of (6.30) can be obtained by means of a second-order Taylor expansion, and this yields the following weighted least-squares objective function

$$\frac{1}{2} \sum_{k=1}^{K} \|A_k^h T_{f_k^h} R^h - b_k\|_{\Sigma_b^{-1}}^2 \tag{6.50}$$

where $A_k^h = [A_{11k}^h, \ldots, A_{rpk}^h] \in \mathbb{R}^{rp \times n^2}$, $b_k = [b_{11k}, \ldots, b_{rpk}] \in \mathbb{R}^{rp \times 1}$ where $b_{ijk} = (\log(I_0 T_e) - \log(y_{ijk}))$, and $\Sigma_b = \text{diag}(y_k)^{-1}$.

The least-squares form (6.50) motivated us to study the SVD of the following linear system, $i.e.$,

$$
\begin{bmatrix} A_1^h T_{f_1^h} \\ A_2^h T_{f_2^h} \\ \vdots \\ A_K^h T_{f_K^h} \end{bmatrix} R^h = \begin{bmatrix} b_1 \\ b_2 \\ \vdots \\ b_K \end{bmatrix}. \tag{6.51}
$$

To simplify our investigations, we assume that the deformation field f^h is known with respect to the reference configuration and we represent the transformation operator T_{f^h} in a matrix form, denoted by T. In order to analyze the impact of deformations on a MC reconstruction, we take four deformation configurations with zero, small, moderate, and large displacements with respect to the reference configuration as shown in Fig.6.6. Please note that $T = T_z$, $T = T_s$, $T = T_m$, and $T = T_l$ for zero, small, medium, and large displacements respectively. In our example, the deformation maps, as shown in Fig.6.6(b), can be expressed in a closed form, $i.e.$,

$$
\begin{aligned}
(f_t)_1 &= x_1 + \alpha_t \exp\left(-\frac{x_1^2}{\sigma_{x_1}}\right) \exp\left(-\frac{x_2^2}{\sigma_{x_2}}\right), \\
(f_t)_2 &= x_2
\end{aligned} \tag{6.52}
$$

where (x_1, x_2) are spatial points. The $(\alpha_t)_z = 0$ is for zero displacement with respect to the reference configuration, and the $(\alpha_t)_s = 0.16$, $(\alpha_t)_m = 0.48$, $(\alpha_t)_l = 0.64$ are for small, moderate, and large displacements respectively.

Fig.6.7(a) shows singular values of the transformation matrix T at different deformation configurations. The largest singular value of the matrix T, $i.e.$,

$$
\begin{aligned}
\sigma_{max}(T_z) &= 1, & \sigma_{max}(T_s) &= 1.15, \\
\sigma_{max}(T_m) &= 1.82, & \sigma_{max}(T_l) &= 2.96,
\end{aligned}
$$

is increasing with increase in the average displacement length of a deformation map. The matrix T_z, corresponding to zero displacement configuration, is an identity matrix due to zero displacement with respect to the reference configuration. Therefore all singular values of the matrix T_z is equal to 1. Notice that, the rank deficiency of the matrix T is increasing with increase in the average displacement length as shown in Fig. 6.7(a). The image features belong to the null space of T disappear after the interpolation and a null space is becoming larger with large deformations.
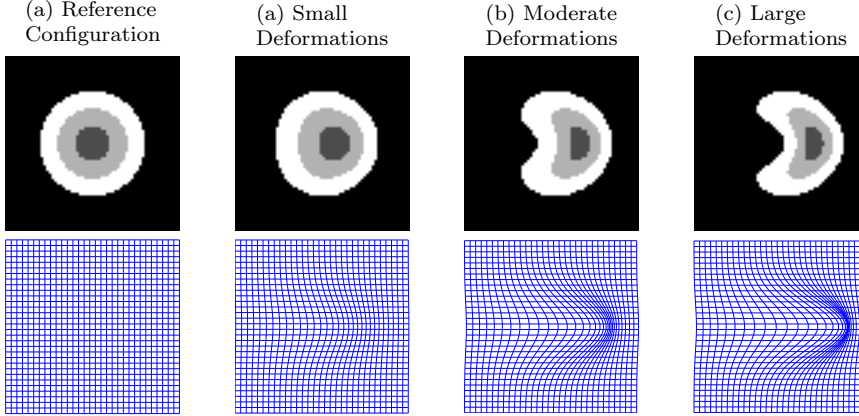
Figure 6.6: Dynamic Phantom and deformation maps with respect to the reference configuration. The deformation fields are defined in (6.52) where $\sigma_{x_1} = 0.3$, $\sigma_{x_2} = 0.15$.

In order to see the impact of rank deficiency on the MC reconstruction due to deformations, we analyze the MC linear system (6.51) where we consider that the data is available only for two frames corresponding to different deformation configurations. This reduces the linear system (6.51) to

$$A_T R = \begin{bmatrix} A_1 T_1 \\ A_2 T_2 \end{bmatrix} R = \begin{bmatrix} b_1 \\ b_2 \end{bmatrix} \tag{6.53}$$

where we have removed h from superscripts to simplify our notations and $A_T = [A_1 T_1, A_2 T_2]^T$.

Given the fact that the rank deficiency of the matrix T increases with large deformations, we would like to study how different deformation configurations affects the null space of the system matrix A_T. Suppose, T_1 represents a small deformation and T_2 represents a large deformation. The dimension of the null spaces then satisfy

$$\dim \mathcal{N}(T_1) \leq \dim \mathcal{N}(T_2). \tag{6.54}$$

In general, it is true that

$$\mathcal{N}(T_1) \subseteq \mathcal{N}(A_1 T_1), \qquad\qquad \mathcal{N}(T_2) \subseteq \mathcal{N}(A_2 T_2),$$
$$\dim \mathcal{N}(T_1) \leq \dim \mathcal{N}(A_1 T_1), \qquad \dim \mathcal{N}(T_2) \leq \dim \mathcal{N}(A_2 T_2). \tag{6.55}$$

This implies that the total null space either remains same or grows after multiplying T_1 and T_2 with the system matrix A_1 and A_2, respectively, as illustrated in Fig. 6.7(b).
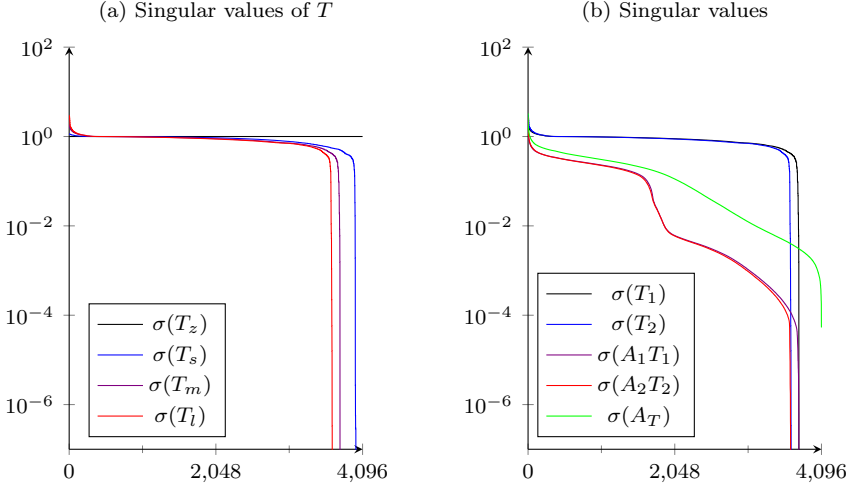
Figure 6.7: Singular values of T and $A_T = [A_1 T_1, A_2 T_2]^T \in \mathbb{R}^{2n \times n}$ where $n = 4096$, $T_1 = T_m$ and $T_2 = T_l$. $T = T_z$, $T = T_s$, $T = T_m$, and $T = T_l$ for zero, small, medium, and large displacements with respect to the reference configuration, respectively.

The null space of the matrix A_T satisfies

$$\mathcal{N}(A_T) = \mathcal{N}(A_1 T_1) \cap \mathcal{N}(A_2 T_2), \tag{6.56}$$
$$\mathcal{N}(A_T) \subseteq \mathcal{N}(A_1 T_1), \tag{6.57}$$
$$\mathcal{N}(A_T) \subseteq \mathcal{N}(A_2 T_2). \tag{6.58}$$

and

$$\dim \mathcal{N}(A_T) \leq \dim \mathcal{N}(A_1 T_1), \text{ and}$$
$$\dim \mathcal{N}(A_T) \leq \dim \mathcal{N}(A_2 T_2). \tag{6.59}$$

This signifies that the null space of A_T is the intersection of the null spaces of $A_1 T_1$ and $A_2 T_2$. For our test case, as shown in Fig.6.7(b), it seems that the intersection of the null space of $A_1 T_1$ and $A_2 T_2$ only has a zero vector, therefore the matrix A_T has a full column rank, however, $A_1 T_1$ and $A_2 T_2$ are rank deficient. These results are true for our test case; we still need to do investigations for a very general case.

Now, we study the impact of the sampling schemes on the MC reconstructions where $A_1 = A_2$ for the PS scheme and $A_1 \neq A_2$ for the MAIS scheme. The singular value decay for the matrix A_T is displayed in Fig.6.8 with different deformation configurations. The matrix A_T has a full column rank with the

Singular values of A_T with the PS and the MAIS scheme.
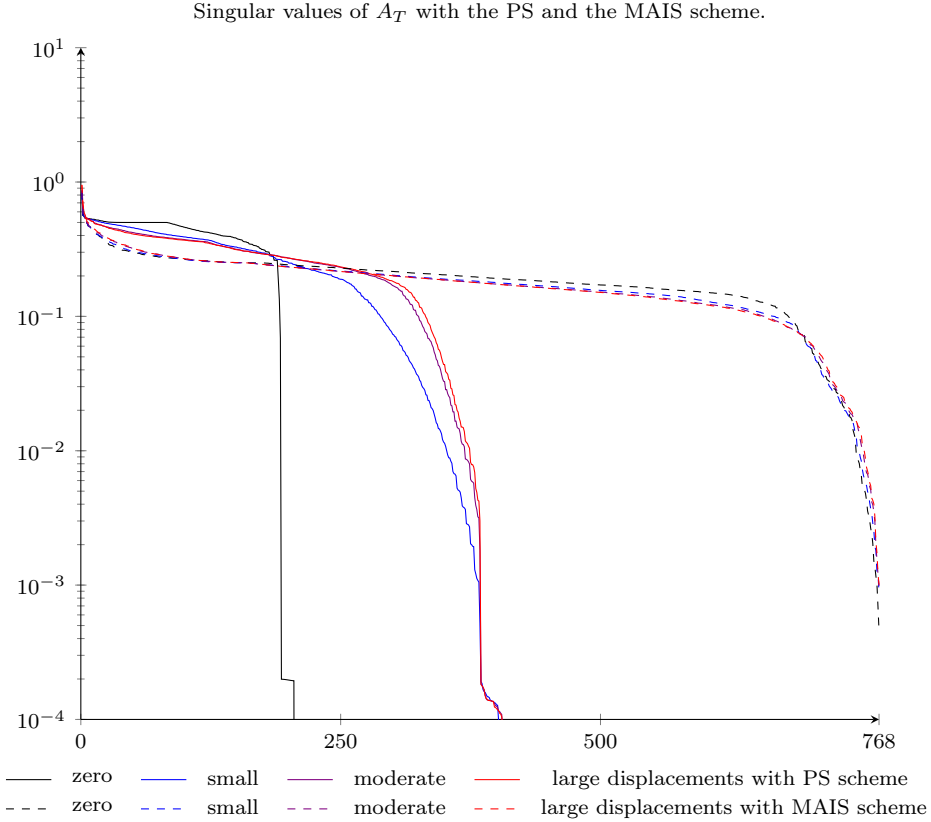
Figure 6.8: Singular values of $A_T \in \mathbb{R}^{m \times n}$ where $m = 768$, $n = 4096$, and $T_1 = T_z$ corresponding to the reference configuration, but T_2 varies with different deformation configurations with respect to the reference configuration. $T_2 = T_z$ for the zero displacements, $T_2 = T_s$ for the small displacements, $T_2 = T_m$ for the moderate displacements, and $T_2 = T_l$ for the large displacements. $A_1 = A_2$ for the PS scheme, but $A_1 \neq A_2$ for the MAIS scheme. The singular value decay does not change much with different deformation configurations, especially with the MAIS scheme, even though properties of the matrix T varies with the deformation configuration.

MAIS scheme and has a trivial null space, however the matrix A_T is a rank deficient matrix with the PS scheme. Therefore, the number of features of a given object do not appear on the sinogram with the PS scheme, and hence we can not reconstruct the number of features of the object with the PS scheme.

We stop our preliminary investigation at this point, but there are many questions which need to be answered in the context of the sampling schemes and the MC reconstruction model. We can study how the sampling schemes affect the motion estimation assuming that the reference frame is known, benefits of the implicit frame based motion modelling over the explicit frame-based motion modelling, the effect of a trade-off between the exposure time and the number of projections on the motion estimation and the image reconstructions, how the MC model performs if stationarity assumption is invalid within a frame, and many more.

6.8   Conclusion

It has been shown that the distribution of projection views over time, particularly based on an interlaced sampling scheme, enhances the quality of images reconstructed with a temporal regularized reconstruction model for dynamic CT. In this work, we emphasize the importance of the interlacing scheme with the MC reconstruction model. The MC reconstruction model exploit information from the acquired projection data to estimate time-dependent changes of a deforming object. We observed that the variability in the projection data greatly influences the quality of a MC reconstruction.

Major interlacing schemes are not a fixed angular sampling scheme, and hence not easy to implement in practice. Moreover, the existing interlaced FAS schemes are not suitable to scan fast-moving objects. In this work, we propose an interlaced FAS scheme based on the family of metallic angles. This scheme guarantees an aperiodic pattern and it is suitable to scan fast-moving objects due to small and adjustable angular gaps between consecutive projections. To evaluate the performance of the proposed sampling scheme, we developed an implicit reference based MC reconstruction model based on an assumption, *i.e.*, so-called one-to-one correspondence almost everywhere. Our numerical scheme guarantees that the deformation map and its inverse both have a one-to-one correspondence almost everywhere. Our experimental results indicate that the proposed interlacing scheme substantially enhances the quality of images reconstructed with the MC reconstruction model based on the simulated datasets.

To gain insight into the MC reconstruction model, we perform an SVD analysis of a related MC linear model where we assumed that the deformation map with respect to the reference configuration is known. This also allows us to analyse the impact of deformations on the MC reconstructions. We observed that the rank deficiency of an interpolation/transformation matrix associated with the deformations increases with increase in the average displacement length. This indicates that few features of an image may not appear after interpolation.

Our SVD analysis also indicates that the system matrix associated with the PS scheme is highly rank deficient, therefore a lot of image features do not appear on the sinogram. As a result, the MC reconstructions are generally of a poor quality with the PS scheme. Our investigations are mainly on a preliminary stage and need more attention. However, they point to some interesting questions to be answered for a more general case.

CHAPTER 7

Conclusion and Future Work

This thesis aims to understand and investigate different factors that can influence the quality of dynamic CT reconstructions. Mainly, we studied three fundamental issues associated with dynamic CT, *i.e.*, the uncertainties due to flat-field measurements, the distribution of projection views over time, and the non-corresponding motion models. In this chapter, we summarize our key findings in a broader context, point out limitations of our proposed models and methods, and comment on various topics that warrant further studies.

The first study points out that the flat-field uncertainties may cause severe and systematic artifacts, known as ring artifacts, in time-limited X-ray tomography such as dynamic CT. Our analysis shows an inverse relationship between severity of the ring artifacts and the flat-field intensity. The existing correction methods, roughly speaking, are based on the geometric nature of ring artifacts observed in either the sinogram or the reconstruction, however, our approach takes into account the statistical properties of the flat-fields. The proposed reconstruction model jointly estimates the flat-field intensity and the attenuation function of the object. The maximum likelihood estimate of the flat-field intensity through our model depends not only on the measurements without the object but also on the measurements with the object which also contain information about the flat-field intensity. As a result, the flat-field intensity estimate improves which leads to reduction in the ring artifacts. Our experimental results indicate that the model effectively mitigates ring artifacts even for low SNR data, not only

with simulated data, but also with real data sets.

We have also shown that the proposed JMAP model and its quadratic approximation model, *i.e.*, a stripe-weighted least-squares (SWLS) model, perform similar with regards to noise and reconstruction quality. The SWLS model paves the way to utilize iterative optimization algorithms such as block row-action methods which have fast initial convergence towards the desired reconstruction. We have also proposed a "ring ratio" error measure which quantifies the flat-field error in the image domain and assess the reduction of ring artifacts in the reconstructions. The error measure is motivated by the first-order analysis of a log-normalized sinogram as shown in section (4.1.3). Therefore, we point out that this measure is not specific to our test cases, rather it can be used in general to evaluate the performance of other ring artifact correction algorithm.

The proposed JMAP model assumes that the object is stationary during the data acquisition. We can derive a motion-compensated (MC) reconstruction model with uncertain flat-fields utilizing the proposed methodology. We think that the motion estimation may be very sensitive to the ring artifacts, in part, because of the failure of the underlying assumption upon which the motion model is based, *i.e.*, the so-called one-to-one correspondence almost everywhere. Therefore, we believe that a motion-compensated (MC) reconstruction model which takes into account the cause of these ring artifacts may enhance the quality of reconstructions for dynamic CT. We also mention that the proposed methodology can readily be extended to estimate a time-varying flat-field, *e.g.*, in applications where the flat-field does not remain stable while acquiring the tomographic measurements.

The second study demonstrates that the non-corresponding motion model based on the underlying physics of crack formation regularizes non-smooth and large deformations along cracks with minimal influence on the nearby regions. We derive the motion model based on two fundamental principles of crack formation. First, a material lose its stiffness entirely at the location of a crack, and second, the material dissipates energy proportional to the crack surface. We formulate the dissipation energy in terms of a soft crack indicator function and derive a registration model based on the minimum total potential energy principle. The resulting registration model jointly estimates the crack indicator function and the deformation map. The crack indicator function allows to modulate the stiffness of a material, and as a result, regularize the non-smooth and the large deformations along the crack region. Moreover, it masks the crack region such that the registration in the non-crack regions executes independently. Therefore, crack regions have a minimum influence on the deformations in the non-crack region.

We should note that the proposed image registration framework does not depend

on a specific data-fidelity measure or a regularization energy for the deformation map. We have also shown the effectiveness of this framework with two data-fidelity measures suitable for intensity- and mass-preserving applications. Therefore, it is worth to investigate the efficacy of this framework with other data-fidelity measures and regularization energies, especially with Normalized Gradient Fields (NGF) - the image gradient based data-fidelity measure. NGF could be a suitable measure to track the motion of a deforming object based on the edge information of an object. Although our investigations were motivated to develop motion models for dynamic CT, we realized that the proposed model has applicability in the medical image registration applications as well, *e.g.*, registration of histological images where cracks may develop during staining of tissues.

The numerical scheme for our proposed non-convex registration model is based on a multi-level strategy, where the optimal point at a coarse discretization serves as an initial guess at a finer discretization. We expect that the optimal point at a coarse discretization is close to a desired local minimum. This scheme fails for high-resolution images where a crack that is a few-pixel wide completely disappears at a coarse discretization. Thus, the optimal point at a coarse discretization may not be close to a desired local minimum. Therefore, more work needs to be done to develop a proper numerical scheme for our model. In the future, we intend to do the well-posedness analysis for the proposed model to gain the theoretical insight. After thorough numerical and theoretical studies, another important step could be to incorporate the motion model into a motion-compensation framework. It is also worth investigating the effect of regularization energies that favor discontinuous and non-smooth deformation fields, *e.g.*, a total-variation-based regularization energy, combined with our proposed framework.

The third study concludes that an interlaced distribution of projection views over time enhances the spatio-temporal resolution of motion-compensated reconstructions. Major interlacing schemes are not fixed angular gap sampling (FAS) schemes, and hence they are not easy to implement in practice. Moreover, the existing interlaced FAS schemes are not suitable to scan fast-moving objects. The proposed interlaced FAS scheme based on the family of metallic angles guarantees an aperiodic projection pattern. It is also suitable to scan fast-moving objects due to small, adjustable angular gaps between consecutive projections. We observed that the variability in the projection data, due to the interlaced projections, greatly influences the quality of a MC reconstruction.

A numerical scheme for the MC reconstruction model should ensure global invertibility of a deformation map to satisfy the underlying model assumption, *i.e.*, a so-called one-to-one correspondence almost everywhere. However, very few studies have given attention to the crucial requirement of the global in-

vertibility in the context of MC reconstructions. Therefore, we re-emphasize the need for a proper numerical scheme. Our numerical scheme guarantees the global invertibility by incorporating a Dirichlet boundary condition for the deformation as well as ensures a positive Jacobian determinant of the deformation map almost everywhere. We incorporate the Dirichlet boundary condition by modifying a large sparse Hessian matrix, but it is not an efficient numerical approach. Moreover, the Hessian matrix construction is a computationally intensive task. Therefore, we think that the use of an accelerated first-order iterative method for the non-convex problem with a linear constraint to incorporate Dirichlet boundary condition could be an approach to reduce memory footprint and overall computation time.

In our preliminary investigations, with the help of an SVD analysis, we observed that for our test cases, the rank deficiency of the interpolation/transformation matrix increases with increasing average displacement length in respect to the reference configuration. This means, some features of the image may disappear after interpolation. Presently, we do not know whether this finding is valid or not for a more general case; moreover, we need to analyze the effects of rank deficiency on the MC reconstructions. The SVD analysis also indicates that the system matrix associated with the progressive sampling scheme is highly rank deficient. Therefore, a lot of image features do not appear on the sinogram, and as a result, we obtain poor quality MC reconstructions. We also observed a few artifacts in our MC reconstructions; however, we do not know the real reasons behind these artifacts. We believe that a thorough investigation of the cause of these artifacts may bring forth new models to mitigate these reconstruction artifacts.

Bibliography

[Aarle15]   W. van Aarle, W. J. Palenstijn, J. D. Beenhouwer, T. Altantzis, S. Bals, K. J. Batenburg, and J. Sijbers. "The {AS-TRA} Toolbox: A platform for advanced algorithm development in electron tomography". In: *Ultramicroscopy* 157 (Oct. 2015), pages 35–47.

[Abascal16]   J. F. P. J. Abascal, M. Abella, E. Marinetto, J. Pascau, and M. Desco. "A Novel Prior- and Motion-Based Compressed Sensing Method for Small-Animal Respiratory Gated CT". In: *PLoS One* 11.3 (Mar. 2016). Edited by Q. Zhang, pages 1–20.

[Ambrosio90]   L. Ambrosio and V. M. Tortorelli. "Approximation of Functional Depending on Jumps by Elliptic Functional via t-Convergence". In: *Communications on Pure and Applied Mathematics* 43.8 (Dec. 1990), pages 999–1036.

[Bateman54]   H. Bateman. *Table of Integral Transforms, Vol. 2*. McGraw-Hill, 1954.

[Berendsen14]   F. F. Berendsen, A. N. T. J. Kotte, A. A. C. de Leeuw, I. M. Jürgenliemk-Schulz, M. A. Viergever, and J. P. W. Pluim. "Registration of Structurally Dissimilar Images in MRI-based Brachytherapy". In: *Physics in Medicine and Biology* 59.15 (Aug. 2014), pages 4033–4045.

[Berger85]   J. Berger. *Statistical Decision Theory and {B}ayesian Analysis*. Springer New York, 1985, page 558.

[Bertero98]   M. Bertero and P. Boccacci. *Introduction to Inverse Problems in Imaging*. CRC Press, 1998, page 352.

[Blume10]   M. Blume, A. Martinez-Moller, A. Keil, N. Navab, and
               M. Rafecas. "Joint Reconstruction of Image and Motion in
               Gated Positron Emission Tomography". In: *IEEE Transac-
               tions on Medical Imaging* 29.11 (Nov. 2010), pages 1892–
               1906.

[Blume12]   M. Blume, N. Navab, and M. Rafecas. "Joint Image and
               Motion Reconstruction for PET using a B-Spline Motion
               Model". In: *Physics in Medicine and Biology* 57.24 (Dec.
               2012), pages 8249–8270.

[Bonnet03]   S. Bonnet, A. Koenig, S. Roux, P. Hugonnard, R. Guille-
               maud, and P. Grangeat. "Dynamic X-ray computed to-
               mography". In: *Proceedings of the IEEE* 91.10 (Oct. 2003),
               pages 1574–1587.

[Bourdin00]   B. Bourdin, G. Francfort, and J.-J. Marigo. "Numerical ex-
               periments in revisited brittle fracture". In: *Journal of the
               Mechanics and Physics of Solids* 48.4 (Apr. 2000), pages 797–
               826.

[Brett01]   M. Brett, A. P. Leff, C. Rorden, and J. Ashburner. "Spa-
               tial Normalization of Brain Images with Focal Lesions Us-
               ing Cost Function Masking". In: *NeuroImage* 14.2 (2001),
               pages 486–500.

[Brown92]   L. G. Brown. "A Survey of Image Registration Techniques".
               In: *ACM Computing Surveys* 24.4 (Dec. 1992), pages 325–
               376.

[Burger13]   M. Burger, J. Modersitzki, and L. Ruthotto. "A Hypere-
               lastic Regularization Energy for Image Registration". In:
               SIAM Journal on Scientific Computing 35.1 (Jan. 2013),
               B132–B148.

[Burger17]   M. Burger, H. Dirks, L. Frerking, A. Hauptmann, T. He-
               lin, and S. Siltanen. "A Variational Reconstruction Method
               for Undersampled Dynamic X-ray Tomography based on
               Physical Motion Models". In: *Inverse Problems* 33.12 (Dec.
               2017), page 124008.

[Buzug08]   T. M. Buzug. *Computed Tomography - From Photon Statis-
               tics to Modern Cone-beam CT*. 1st edition. Springer-Verlag
               Berlin Heidelberg, 2008.

[Chaim81]   B. Chaim. "Optimal Registration of Deformed Images".
               PhD thesis. 1981.

[Chen07]   M. Chen, W. Lu, Q. Chen, K. J. Ruchala, and G. H. Olivera. "A Simple Fixed-point Approach to Invert a Deformation Fields)". In: *Medical Physics* 35.1 (Dec. 2007), pages 81–88.

[Chen08]   G.-H. Chen, J. Tang, and S. Leng. "Prior Image Constrained Compressed Sensing (PICCS): A Method to Accurately Reconstruct Dynamic CT Images from Highly Undersampled Projection Data Sets". In: *Medical Physics* 35.2 (Jan. 2008), pages 660–663.

[Chen15]   K. Chen, A. Derksen, S. Heldmann, M. Hallmann, and B. Berkels. "Deformable Image Registration with Automatic Non-Correspondence Detection". In: *Scale Space and Variational Methods in Computer Vision*. Springer International Publishing, 2015, pages 360–371.

[Chitphakdithai10]   N. Chitphakdithai and J. S. Duncan. "Non-rigid Registration with Missing Correspondences in Preoperative and Postresection Brain Images". In: *Medical Image Computing and Computer-Assisted Intervention – MICCAI 2010*. Springer, Berlin, Heidelberg, 2010, pages 367–374.

[Christensen01a]   G. Christensen and H. Johnson. "Consistent Image Registration". In: *IEEE Transactions on Medical Imaging* 20.7 (July 2001), pages 568–582.

[Christensen01b]   G. Christensen and H. Johnson. "Consistent Image Registration". In: *IEEE Transactions on Medical Imaging* 20.7 (July 2001), pages 568–582.

[Christensen96]   G. Christensen, R. Rabbitt, and M. Miller. "Deformable Templates using Large Deformation Kinematics". In: *IEEE Transactions on Image Processing* 5.10 (1996), pages 1435–1447.

[Chumchob13]   N. Chumchob. "Vectorial Total Variation-Based Regularization for Variational Image Registration". In: *IEEE Transactions on Image Processing* 22.11 (Nov. 2013), pages 4551–4559.

[Chun09]   S. Y. Chun and J. A. Fessler. "Joint Image Reconstruction and Nonrigid Motion Estimation with a Simple Penalty that Encourages Local Invertibility". In: *Proc. of SPIE. Medical Imaging: Image Processing*. 2009, pages 1–9.

[Chun12]   S. Y. Chun and J. A. Fessler. "Spatial Resolution Properties of Motion-Compensated Tomographic Image Reconstruction Methods". In: *IEEE Transactions on Medical Imaging* 31.7 (July 2012), pages 1413–1425.

[Chun13]   S. Y. Chun and J. A. Fessler. "Noise Properties of Motion-Compensated Tomographic Image Reconstruction Methods". In: *IEEE Transactions on Medical Imaging* 32.2 (Feb. 2013), pages 141–152.

[Cnudde13]   V. Cnudde and M. Boone. "High-Resolution X-ray Computed Tomography in Geosciences: A Review of the Current Technology and Applications". In: *Earth-Science Reviews* 123 (Aug. 2013), pages 1–17.

[Dahlman12]   P. Dahlman, A. J. Van Der Molen, M. Magnusson, and A. Magnusson. "How Much Dose can be Saved in Three-phase CT Urography? A Combination of Normal-dose Corticomedullary Phase with Low-dose Unenhanced and Excretory Phases." In: *AJR. American journal of roentgenology* 199.4 (Oct. 2012), pages 852–60.

[Darkner11]   S. Darkner, M. S. Hansen, R. Larsen, and M. F. Hansen. "Efficient Hyperelastic Regularization for Registration". In: *Image Analysis*. Edited by A. Heyden and F. Kahl. Berlin, Heidelberg: Springer Berlin Heidelberg, 2011, pages 295–305.

[De Giorgi89]   E. De Giorgi, M. Carriero, and A. Leaci. "Existence Theorem for a Minimum Problem with Free Discontinuity Set". In: *Archive for Rational Mechanics and Analysis* 108.4 (Nov. 1989), pages 195–218.

[Dean12]   C. J. Dean, J. R. Sykes, R. A. Cooper, P. Hatfield, B. Carey, S. Swift, S. E. Bacon, D. Thwaites, D. Sebag-Montefiore, and A. M. Morgan. "An evaluation of four CT-MRI coregistration techniques for radiotherapy treatment planning of prone rectal cancer patients." In: *The British Journal of Radiology* 85.1009 (Jan. 2012), pages 61–68.

[Doran01]   S. J. Doran, K. K. Koerkamp, M. A. Bero, P. Jenneson, E. J. Morton, and W. B. Gilboy. "A CCD-based Optical CT Scanner for High-resolution 3D Imaging of Radiation Dose Distributions: Equipment Specifications, Optical Simulations and Preliminary Results". In: *Physics in Medicine and Biology* 46.12 (Dec. 2001), pages 3191–3213.

[Drobny15]   D. Drobny, H. Carolus, S. Kabus, and J. Modersitzki. "Handling Non-Corresponding Regions in Image Registration". In: *Bildverarbeitung f{\ "u}r die Medizin 2015*. Springer Berlin Heidelberg, 2015, pages 107–112.

[Droske04]   M. Droske and M. Rumpf. "A Variational Approach to Nonrigid Morphological Image Registration". In: *SIAM Journal on Applied Mathematics* 64.2 (Jan. 2004), pages 668–687.

[Eyndhoven12]   G. V. Eyndhoven, J. Sijbers, and J. Batenburg. "Combined Motion Estimation and Reconstruction in Tomography". In: *Computer Vision – ECCV 2012. Workshops and Demonstrations.* Edited by A. Fusiello, V. Murino, and R. Cucchiara. Berlin, Heidelberg: Springer Berlin Heidelberg, 2012, pages 12–21.

[Fahrig06]   R. Fahrig, R. Dixon, T. Payne, R. L. Morin, A. Ganguly, and N. Strobel. "Dose and Image Quality for a Cone-Beam C-arm CT System". In: *Medical Physics* 33.12 (Dec. 2006), page 4541.

[Fessler96]   J. Fessler and W. Rogers. "Spatial Resolution Properties of Penalized-likelihood Image Reconstruction: Space-invariant Tomographs". In: *IEEE Transactions on Image Processing* 5.9 (1996), pages 1346–1358.

[Fischer02]   B. Fischer and J. Modersitzki. "Fast Diffusion Registration". In: *Contemporary Mathematics* 313 (Jan. 2002). Edited by M. Z. Nashed and O. Scherzer, pages 117–129.

[Fischer04]   B. Fischer and J. Modersitzki. "A Unified Approach to Fast Image Registration and a New Curvature based Registration Technique". In: *Linear Algebra and its Applications* 380 (Mar. 2004), pages 107–124.

[Flohr15]   T. G. Flohr, C. N. De Cecco, B. Schmidt, R. Wang, U. J. Schoepf, and F. G. Meinel. "Computed Tomographic Assessment of Coronary Artery Disease". In: *Radiologic Clinics of North America* 53.2 (Mar. 2015), pages 271–285.

[Flohr16]   T. G. Flohr and B. Schmidt. "CT Technology for Imaging the Thorax: State of the Art". In: *Multidetector-Row {CT} of the Thorax.* Springer International Publishing, July 2016, pages 3–28.

[Francfort98]   G. A. Francfort and J.-J. Marigo. "Revisiting Brittle Fracture as an Energy Minimization Problem". In: *Journal of the Mechanics and Physics of Solids* 46.8 (Aug. 1998), pages 1319–1342.

[FrohnSchauf08] C. Frohn-Schauf, S. Henn, and K. Witsch. "Multigrid based Total Variation Image Registration". In: *Computing and Visualization in Science* 11.2 (Mar. 2008), pages 101–113.

[Geng09]   X. Geng, G. E. Christensen, H. Gu, T. J. Ross, and Y. Yang. "Implicit Reference-based Group-wise Image Registration and its application to Structural and Functional MRI." In: *NeuroImage* 47.4 (Oct. 2009), pages 1341–1351.

[Gigengack12]   F. Gigengack, L. Ruthotto, M. Burger, C. H. Wolters, Xiaoyi Jiang, and K. P. Schafers. "Motion Correction in Dual Gated Cardiac PET Using Mass-Preserving Image Registration". In: *IEEE Transactions on Medical Imaging* 31.3 (Mar. 2012), pages 698–712.

[Griffith21]   A. A. Griffith. "The Phenomena of Rupture and Flow in Solids". In: *Philosophical Transactions of the Royal Society A: Mathematical, Physical and Engineering Sciences* 221.582-593 (Jan. 1921), pages 163–198.

[Haber06]   E. Haber and J. Modersitzki. "Intensity Gradient Based Registration and Fusion of Multi-modal Images". In: *Medical Image Computing and Computer-Assisted Intervention – MICCAI 2006*. Edited by R. Larsen, M. Nielsen, and J. Sporring. Berlin, Heidelberg: Springer Berlin Heidelberg, Oct. 2006, pages 726–733.

[Hahn14]   B. N. Hahn. "Efficient Algorithms for Linear Dynamic Inverse Problems with Known Motion". In: *Inverse Problems* 30.3 (Mar. 2014), page 035008.

[Hahn17]   B. N. Hahn. "Motion Estimation and Compensation Strategies in Dynamic Computerized Tomography". In: *Sensing and Imaging* 18.1 (Dec. 2017), page 10.

[Halliburton12] S. Halliburton, A. Arbab-Zadeh, D. Dey, A. J. Einstein, R. Gentry, R. T. George, T. Gerber, M. Mahesh, and W. G. Weigold. "State-of-the-art in CT Hardware and Scan Modes for Cardiovascular CT". In: *Journal of Cardiovascular Computed Tomography* 6.3 (May 2012), pages 154–163.

[Hansen10]   P. C. Hansen. *Discrete Inverse Problems*. Society for Industrial and Applied Mathematics, Jan. 2010, pages xii + 206.

[Hansen12]   P. C. Hansen and M. Saxild-Hansen. "AIR Tools — A MATLAB Package of Algebraic Iterative Reconstruction Methods". In: *Journal of Computational and Applied Mathematics* 236.8 (Feb. 2012), pages 2167–2178.

[Heindel11]   T. J. Heindel. "A Review of X-Ray Flow Visualization With Applications to Multiphase Flows". In: *Journal of Fluids Engineering* 133.7 (July 2011), page 074001.

[Henao10]   D. Henao and C. Mora-Corral. "Invertibility and Weak
                 Continuity of the Determinant for the Modelling of Cav-
                 itation and Fracture in Nonlinear Elasticity". In: *Archive
                 for Rational Mechanics and Analysis* 197.2 (Aug. 2010),
                 pages 619–655.

[Henao15]   D. Henao, C. Mora-Corral, and X. Xu. "Γ-convergence Ap-
                 proximation of Fracture and Cavitation in Nonlinear Elas-
                 ticity". In: *Archive for Rational Mechanics and Analysis*
                 216.3 (June 2015), pages 813–879.

[Henao16]   D. Henao, C. Mora-Corral, and X. Xu. "A Numerical Study
                 of Void Coalescence and Fracture in Nonlinear Elasticity".
                 In: *Computer Methods in Applied Mechanics and Engineer-
                 ing* 303 (May 2016), pages 163–184.

[Hinkle12]   J. Hinkle, M. Szegedi, B. Wang, B. Salter, and S. Joshi.
                 "4D CT Image Reconstruction with Diffeomorphic Mo-
                 tion Model". In: *Medical Image Analysis* 16.6 (Aug. 2012),
                 pages 1307–1316.

[Holmes09]   M. H. Holmes. *Introduction to the Foundations of Applied
                 Mathematics*. Springer, 2009, page 467.

[Kak01]   A. C. Kak and M. Slaney. *Principles of Computerized To-
                 mographic Imaging*. Society for Industrial and Applied Math-
                 ematics, Jan. 2001, pages xii + 323.

[Katsevich10]   A. Katsevich. "An Accurate Approximate Algorithm for
                 Motion Compensation in Two-Dimensional Tomography".
                 In: *Inverse Problems* 26.6 (June 2010), page 065007.

[Kazantsev15a]   D. Kazantsev, G. Van Eyndhoven, W. R. B. Lionheart,
                 P. J. Withers, K. J. Dobson, S. A. McDonald, R. Atwood,
                 and P. D. Lee. "Employing Temporal Self-similarity across
                 the Entire Time Domain in Computed Tomography Re-
                 construction". In: *Philosophical Transactions of the Royal
                 Society of London A: Mathematical, Physical and Engi-
                 neering Sciences* 373.2043 (June 2015).

[Kazantsev15b]   D. Kazantsev, W. M. Thompson, W. R. B. Lionheart,
                 G. V. Eyndhoven, A. P. Kaestner, K. J. Dobson, P. J.
                 Withers, and P. D. Lee. "4D-CT Reconstruction with Uni-
                 fied Spatial-Temporal Patch-based Regularization". In: *In-
                 verse Problems and Imaging* 9.2 (Mar. 2015), pages 447–
                 467.

[Kim04]   J. Kim and J. Fessler. "Intensity-Based Image Registration Using Robust Correlation Coefficients". In: *IEEE Transactions on Medical Imaging* 23.11 (Nov. 2004), pages 1430–1444.

[Kim14]   Y. Kim, J. Baek, and D. Hwang. "Ring Artifact Correction using Detector Line-ratios in Computed Tomography." In: *Optics express* 22.11 (June 2014), pages 13380–13392.

[Kowalski77]   G. Kowalski. "The Influence of Fixed Errors of a Detector Array on the Reconstruction of Objects from Their Projections". In: *IEEE Transactions on Nuclear Science* 24.5 (June 1977), pages 2006–2016.

[Kowalski78]   G. Kowalski. "Suppression of Ring Artefacts in CT Fan-Beam Scanners". In: *IEEE Transactions on Nuclear Science* 25.5 (Oct. 1978), pages 1111–1116.

[Kwon14]   D. Kwon, M. Niethammer, H. Akbari, M. Bilello, C. Davatzikos, and K. M. Pohl. "PORTR: Pre-Operative and Post-Recurrence Brain Tumor Registration". In: *IEEE Transactions on Medical Imaging* 33.3 (Mar. 2014), pages 651–667.

[Laurent12]   D. Laurent, C. Mennessier, and R. Clackdoyle. "Dynamic Tomography, Mass Preservation and ROI Reconstruction". In: *Second International Conference on Image Formation in X-Ray Computed Tomography*. 2012, page 318.

[Lester99]   H. Lester and S. R. Arridge. "A Survey of Hierarchical Non-linear Medical Image Registration". In: *Pattern Recognition* 32.1 (Jan. 1999), pages 129–149.

[Liu15]   J. Liu, X. Zhang, X. Zhang, H. Zhao, Y. Gao, D. Thomas, D. A. Low, and H. Gao. "5D Respiratory Motion Model based Image Reconstruction Algorithm for 4D Cone-beam Computed Tomography". In: *Inverse Problems* 31.11 (Nov. 2015), page 115007.

[Maintz98]   J. Maintz and M. A. Viergever. "A Survey of Medical Image Registration". In: *Medical Image Analysis* 2.1 (Mar. 1998), pages 1–36.

[Mair06]   B. A. Mair, D. R. Gilland, and J. Sun. "Estimation of Images and Nonrigid Deformations in Gated Emission CT." In: *IEEE transactions on medical imaging* 25.9 (Sept. 2006), pages 1130–44.

[Manavalan16]   G. D. Manavalan and K. Rajgopal. "Estimation of Small Motion for Dynamic X-ray Computed Tomography using a General Motion Model and Moments of Projections". In: *2016 International Conference on Signal Processing and Communications (SPCOM)*. IEEE, June 2016, pages 1–5.

[Marigo16]   J.-J. Marigo, C. Maurini, and K. Pham. "An Overview of the Modelling of Fracture by Gradient Damage Models". In: *Meccanica* 51.12 (Dec. 2016), pages 3107–3128.

[McClelland13]   J. McClelland, D. Hawkes, T. Schaeffter, and A. King. "Respiratory Motion Models: A Review". In: *Medical Image Analysis* 17.1 (Jan. 2013), pages 19–42.

[McClelland17]   J. R. McClelland, M. Modat, S. Arridge, H. Grimes, D. D'Souza, D. Thomas, D. O. Connell, D. A. Low, E. Kaza, D. J. Collins, M. O. Leach, and D. J. Hawkes. "A Generalized Framework Unifying Image Registration and Respiratory Motion Models and Incorporating Image Reconstruction, for Partial Image Data or Full Images". In: *Physics in Medicine and Biology* 62.11 (June 2017), pages 4273–4292.

[Messnarz04]   B. Messnarz, B. Tilg, R. Modre, G. Fischer, and F. Hanser. "A New Spatiotemporal Regularization Approach for Reconstruction of Cardiac Transmembrane Potential Patterns". In: *IEEE Transactions on Biomedical Engineering* 51.2 (Feb. 2004), pages 273–281.

[Modersitzki04]   J. Modersitzki. *Numerical Methods for Image Registration*. Oxford Univesity Press, 2004.

[Modersitzki09]   J. Modersitzki. *FAIR : Flexible Algorithms for Image Registration*. Society for Industrial and Applied Mathematics, 2009, page 189.

[Mohan15]   K. A. Mohan, S. V. Venkatakrishnan, J. W. Gibbs, E. B. Gulsoy, X. Xiao, M. De Graef, P. W. Voorhees, and C. A. Bouman. "TIMBIR: A Method for Time-space Reconstruction from Interlaced Views". In: *IEEE Transactions on Computational Imaging* 1.2 (June 2015), pages 96–111.

[Mokso15]   R. Mokso, D. A. Schwyn, S. M. Walker, M. Doube, M. Wicklein, T. Müller, M. Stampanoni, G. K. Taylor, and H. G. Krapp. "Four-dimensional in Vivo X-ray Microscopy with Projection-guided Gating". In: *Scientific Reports* 5.8727 (Mar. 2015).

[Morton98]   E. Morton, R. Luggar, R. Key, A. Kundu, L. Tavora, and W. Gilboy. "Development of a High Speed X-ray Tomography System for Multiphase Flow Imaging". In: *1998 IEEE Nuclear Science Symposium Conference Record. 1998 IEEE Nuclear Science Symposium and Medical Imaging Conference (Cat. No.98CH36255)*. Volume 2. IEEE, Nov. 1998, pages 995–999.

[Mory16]   C. Mory, G. Janssens, and S. Rit. "Motion-aware Temporal Regularization for Improved 4D Cone-beam Computed Tomography". In: *Physics in Medicine and Biology* 61.18 (Sept. 2016), pages 6856–6877.

[Mumford89]   D. Mumford and J. Shah. "Optimal Approximations by Piecewise Smooth Functions and Associated Variational Problems". In: *Communications on Pure and Applied Mathematics* 42.5 (July 1989), pages 577–685.

[Münch09]   B. Münch, P. Trtik, F. Marone, and M. Stampanoni. "Stripe and Ring Artifact Removal with Combined Wavelet—Fourier Filtering". EN. In: *Optics Express* 17.10 (May 2009), page 8567.

[Münch11]   B. Münch, P. Trtik, and L. Butler. "Spatiotemporal Computed Tomography of Dynamic Processes". In: *Optical Engineering* 50.12 (Dec. 2011), page 123201.

[Nieuwenhove17] V. V. Nieuwenhove, J. De Beenhouwer, J. Vlassenbroeck, M. Brennan, and J. Sijbers. "MoVIT: A Tomographic Reconstruction Framework for 4D-CT". In: *Optics Express* 25.16 (Aug. 2017), page 19236.

[Nithiananthan12] S. Nithiananthan, S. Schafer, D. J. Mirota, J. W. Stayman, W. Zbijewski, D. D. Reh, G. L. Gallia, and J. H. Siewerdsen. "Extra-dimensional Demons: a Method for Incorporating Missing Tissue in Deformable Image Registration." In: *Medical physics* 39.9 (Sept. 2012), pages 5718–31.

[Nuyts13]   J. Nuyts, B. De Man, J. A. Fessler, W. Zbijewski, and F. J. Beekman. "Modelling the Physics in the Iterative Reconstruction for Transmission Computed Tomography". In: *Physics in medicine and biology* 58.12 (June 2013), R63–96.

[Ou11]   Y. Ou, A. Sotiras, N. Paragios, and C. Davatzikos. "DRAMMS: Deformable Registration via Attribute Matching and Mutual-Saliency Weighting." In: *Medical image analysis* 15.4 (Aug. 2011), pages 622–39.

[Paleo15]   P. Paleo and A. Mirone. "Ring Artifacts Correction in Compressed Sensing Tomographic Reconstruction". In: *Journal of synchrotron radiation* 22.5 (Sept. 2015), pages 1268–1278.

[Papoulis02]   A. Papoulis and S. U. Pillai. *Probability, Random Variables and Stochastic Processes.* 4th edition. McGraw-Hill Europe, 2002, page 852.

[Pelc14]   N. J. Pelc. "Recent and Future Directions in CT Imaging." In: *Annals of biomedical engineering* 42.2 (Feb. 2014), pages 260–268.

[Pennec05]   X. Pennec, R. Stefanescu, V. Arsigny, P. Fillard, and N. Ayache. "Riemannian Elasticity: A Statistical Regularization Framework for Non-linear Registration". In: *Medical Image Computing and Computer-Assisted Intervention – MICCAI 2005: 8th International Conference, Palm Springs, CA, USA, October 26-29, 2005, Proceedings, Part II.* Edited by J. S. Duncan and G. Gerig. Berlin, Heidelberg: Springer Berlin Heidelberg, 2005, pages 943–950.

[Periaswamy06] S. Periaswamy and H. Farid. "Medical Image Registration with Partial Data". In: *Medical Image Analysis* 10.3 (June 2006), pages 452–464.

[Pinzer12]   B. R. Pinzer, A. Medebach, H. J. Limbach, C. Dubois, M. Stampanoni, and M. Schneebeli. "3D-characterization of Three-phase Systems using X-ray Tomography: Tracking the Microstructural Evolution in Ice Cream". In: *Soft Matter* 8.17 (Apr. 2012), page 4584.

[Prell09]   D. Prell, Y. Kyriakou, and W. A. Kalender. "Comparison of Ring Artifact Correction Methods for Flat-detector CT". In: *Physics in medicine and biology* 54.12 (June 2009), pages 3881–95.

[Prince15]   J. L. Prince and J. M. Links. *Medical Imaging Signals and Systems.* Pearson, 2015, page 519.

[Rabbitt95]   R. D. Rabbitt, J. A. Weiss, G. E. Christensen, and M. I. Miller. "Mapping of Hyperelastic Deformable Templates using the Finite Element Method". In: *Proceedings of the SPIE.* Edited by R. A. Melter, A. Y. Wu, F. L. Bookstein, and W. D. K. Green. Volume 2573. Aug. 1995, pages 252–265.

[Rashid12]   S. Rashid, S. Lee, and M. Hasan. "An Improved Method for the Removal of Ring Artifacts in High Resolution CT Imaging". In: *EURASIP Journal on Advances in Signal Processing* 2012.1 (2012), page 93.

[Rattey81]   P. Rattey and A. Lindgren. "Sampling the 2-D Radon Transform". In: *IEEE Transactions on Acoustics, Speech, and Signal Processing* 29.5 (Oct. 1981), pages 994–1002.

[Raven98]   C. Raven. "Numerical Removal of Ring Artifacts in Microtomography". In: *Review of Scientific Instruments* 69.8 (Aug. 1998), page 2978.

[Richard04]   F. Richard. "A New Approach for the Registration of Images with Inconsistent Differences". In: *Proceedings of the 17th International Conference on Pattern Recognition, 2004.* IEEE, 2004, pages 649–652.

[Rit09]   S. Rit, D. Sarrut, and L. Desbat. "Comparison of Analytic and Algebraic Methods for Motion-Compensated Cone-Beam CT Reconstruction of the Thorax". In: *IEEE Transactions on Medical Imaging* 28.10 (Oct. 2009), pages 1513–1525.

[Rose15]   S. Rose, M. S. Andersen, E. Y. Sidky, and X. Pan. "Noise Properties of CT Images Reconstructed by use of Constrained Total-variation, Data-discrepancy Minimization". In: *Medical physics* 42.5 (May 2015), pages 2690–2698.

[Rudin92]   L. I. Rudin, S. Osher, and E. Fatemi. "Nonlinear Total Variation based Noise Removal Algorithms". In: *Physica D: Nonlinear Phenomena* 60.1-4 (Nov. 1992), pages 259–268.

[Ruthotto15]   L. Ruthotto and J. Modersitzki. "Non-linear Image Registration". In: *Handbook of Mathematical Methods in Imaging.* New York, NY: Springer New York, 2015, pages 2005–2051.

[Sauer93]   K. Sauer and C. Bouman. "A Local Update Strategy for Iterative Reconstruction from Projections". In: *IEEE Transactions on Signal Processing* 41.2 (Feb. 1993), pages 534–548.

[Schmitt02]   U. Schmitt and A. K. Louis. "Efficient Algorithms for the Regularization of Dynamic Inverse Problems: I. Theory". In: *Inverse Problems* 18.3 (June 2002), page 308.

[Sicsic13]   P. Sicsic and J.-J. Marigo. "From Gradient Damage Laws to Griffith's Theory of Crack Propagation". In: *Journal of Elasticity* 113.1 (Sept. 2013), pages 55–74.

[Sijbers04]   J. Sijbers and A. Postnov. "Reduction of Ring Artefacts in High Resolution Micro-CT Reconstructions". In: *Physics in medicine and biology* 49.14 (July 2004), N247–N253.

[Sotiras13]   A. Sotiras, C. Davatzikos, and N. Paragios. "Deformable Medical Image Registration: A Survey". In: *IEEE Transactions on Medical Imaging* 32.7 (July 2013), pages 1153–1190.

[Spinadel99]   V. W. de Spinadel. "The Metallic Means Family and Multifractal Spectra". In: *Nonlinear Analysis: Theory, Methods & Applications* 36.6 (June 1999), pages 721–745.

[Suhr15]   S. Suhr. "Variational Methods for Combined Image and Motion Estimation". PhD thesis. University of Munster, 2015.

[Thomas10]   C. Thomas, M. Heuschmid, D. Schilling, D. Ketelsen, I. Tsiflikas, A. Stenzl, C. D. Claussen, and H.-P. Schlemmer. "Urinary Calculi Composed of Uric Acid, Cystine, and Mineral Salts: Differentiation with Dual-energy CT at a Radiation Dose Comparable to that of Intravenous Pyelography." In: *Radiology* 257.2 (Nov. 2010), pages 402–9.

[Thompson15]   W. M. Thompson, W. R. B. Lionheart, E. J. Morton, M. Cunningham, and R. D. Luggar. "High Speed Imaging of Dynamic Processes with a Switched Source X-ray CT System". In: *Measurement Science and Technology* 26.5 (May 2015), page 055401.

[Tian11]   Z. Tian, X. Jia, B. Dong, Y. Lou, and S. B. Jiang. "Low-dose 4DCT Reconstruction via Temporal Nonlocal Means". In: *Medical Physics* 38.3 (Feb. 2011), pages 1359–1365.

[Wang04]   Z. Wang, A. C. Bovik, H. R. Sheikh, and E. P. Simoncelli. "Image Quality Assessment: From Error Visibility to Structural Similarity". In: *IEEE Transactions on Image Processing* 13.4 (Apr. 2004), pages 600–612.

[Whiting06]   B. R. Whiting, P. Massoumzadeh, O. A. Earl, J. A. O'Sullivan, D. L. Snyder, and J. F. Williamson. "Properties of Preprocessed Sinogram Data in X-ray Computed Tomography". In: *Medical physics* 33.9 (Sept. 2006), pages 3290–3303.

[Willis95]   P. Willis and Y. Bresler. "Optimal Scan for Time-varying Tomography. I. Theoretical Analysis and Fundamental Limitations". In: *IEEE Transactions on Image Processing* 4.5 (May 1995), pages 642–653.

[Yan16]   L. Yan, T. Wu, S. Zhong, and Q. Zhang. "A Variation-based Ring Artifact Correction Method with Sparse Constraint for Flat-detector CT". In: *Physics in medicine and biology* 61.3 (Feb. 2016), pages 1278–92.

[Zitová03] B. Zitová and J. Flusser. "Image Registration Methods: A Survey". In: *Image and Vision Computing* 21.11 (Oct. 2003), pages 977–1000.